Liquid Deposition Photolithography for Efficient Three Dimensional Structuring

by

Adam C. Urness

B.S., B.A., University of St. Thomas, St. Paul, MN (2007)

A thesis submitted to the

Faculty of the Graduate School of the

University of Colorado in partial fulfillment

of the requirements for the degree of

Doctor of Philosophy

Department of Electrical, Computer and Energy Engineering

2013

This thesis entitled:
Liquid Deposition Photolithography for Efficient Three Dimensional Structuring
written by Adam C. Urness
has been approved for the Department of Electrical, Computer and Energy Engineering

_____

Prof. Robert R. McLeod

_____

Prof. Juliet Gopinath

Date _____

The final copy of this thesis has been examined by the signatories, and we find that both
the content and the form meet acceptable presentation standards of scholarly work in the
above mentioned discipline.

Urness, Adam C. (Ph.D., Electrical Engineering)

Liquid Deposition Photolithography for Efficient Three Dimensional Structuring

Thesis directed by Prof. Robert R. McLeod

Photonic devices increasingly require three dimensional (3D) control of refractive index, but existing fabrication methods such as femtosecond micromachining, multi-layer planar lithography and bulk diffusion can only address a select scale range, are often limited in complexity or thickness and have low throughput. This Thesis presents a new fabrication process, liquid deposition photolithography (LDP), that can efficiently create mm^3 optical devices with programmable, gradient index of refraction with arbitrary feature size. Index contrast of 0.1 is demonstrated, which is 100 times larger than femtosecond micromachining and 20 times larger than commercial holographic photopolymers, allowing greater flexibility in photonic device fabrication.

The 3D volume is created through repetitive layering of liquid photopolymer, where each layer is structured and solidified by projection lithography. In addition to full 3D control of index, processing time in LDP is reduced compared to multi-layer planar lithography because the material is self-developing, enabling the entire process to be completed on a single instrument. The self-developing process has the unusual property that total fabrication time for a fixed thickness decreases as the number of layers is increased, enabling fabrication 10^5 faster than femtosecond micromachining. The high throughput and index contrast is demonstrated by sequentially writing 100 layers to fabricate a mm thick waveguide array that has a fabrication rate of 1.2 mm^3/hour and index contrast of 0.1.

Acknowledgements

First, I would like to acknowledge and thank my advisor, Bob McLeod. He has been an incredible source of knowledge, insight, advice, and especially enthusiasm. When I joined his Research Group I had limited research experience and was scared to death to give public presentations. His support and encouragement gave me the confidence to pursue my own research ideas and to deliver presentations clearly and with confidence to large audiences.

I would like to thank all other members, both past and present, of the McLeod Research Group, Amy Sullivan, Matt Grabowski, Eric Moore, Mark Ayers, Chungfang Ye, Keith Kamysiak, Ben Kowalski, Anna Linnenberger, Michael Cole, Marty Baylor, Darren Forman, Patrick Wagner, Martha Bodine, David Glugla, Callie Fiedler and Jacob Friedlein for all their help and support. I have also had the pleasure of working with and having insightful conversations with Sean Quirin, Ginni Sharma, Ben Braker and Don Conkey throughout my graduate career. I would also like to thank the undergraduate students that I have had the pleasuring of working with and mentoring through the years. In particular, Seth Miers made a major contribution to this thesis for his work with the DMD software and his continued contributions will undoubtedly further research on LDP.

I would like to thank my committee members: Prof. Juliet Gopinath, Prof. Christopher Bowman, Prof. Rafael Piestun and Prof. Carol Cogswell. I would like to give additional thanks to Prof. Gopinath for her contribution to improve this thesis and Prof. Piestun who oversaw the fellowship program that made this research possible. Further thanks are also due to Prof. Bowman, who has been an incredible source of polymer chemistry knowledge

and directed me to Patrick Doyle's paper on particle synthesis that inspired the key innovation of my research. I would also like to thank Carol Cogswell for the use of the differential interference contrast microscope in her lab.

The knowledge that I have gleaned regarding the chemistry and practical laboratory production of volume photopolymer materials is principally due to Michael Cole. I would like to thank him for aiding my understanding despite my lack of background in chemistry. I would also like to thank Neil Cramer, Devatha Nair and Richard Sheridan from the Bowman research labs for furthering my chemistry education and making the collaboration with their lab a productive one.

I would also like to acknowledge the financial support I have received through my years in the program. I have been the fortunate recipient of two fellowships an NSF IGERT fellowship under the Computational Optical Sensing and Imaging (COSI) program and a GAANN fellowship under the functional materials program. This work has also been supported under NSF STTR (grant no. IIP-0822695) and an an AF MURI (grant no. FA9550-09-1-0677).

Finally, I would like to thank my family and friends who have supported me these last 5 years. My wife, Kimberly, has been with me every step of the way and has given me love and encouragement throughout the journey.

Contents

Chapter

Tables

Table

Figures

Figure

Chapter 1

Introduction

1.1   Motivation for three dimensional structuring

Additive lithography is transforming the fields of advanced photonic devices, micro-electromechanical systems (MEMS), high resolution prototyping parts and synthetic cellular environments due to its ability to rapidly and inexpensively create arbitrary 3D structure. Existing methods generally create physical structure from one or a small number of uniform materials. This thesis introduces a new 3D structuring method that controls material density and thus refractive index. This has applications in the fabrication of new forms of photonic devices including 3D guided wave and gradient-index optics.

1.1.1   Motivation for physical structuring

One of the most-developed applications of physical 3D structuring is rapid prototyping of user defined models, both for the purpose of designing new products and limited production manufacturing. Traditional prototyping methods involve labor-intensive mould making and casting steps [1], and have high upfront costs and long lead-times, making them unattractive for small production runs or prototyping. Rapid prototyping technologies, on the other hand, have the ability to create objects directly from a computer design, significantly speeding up the development of products as well as reducing cost in limited production runs. Currently, rapid prototyping is common practice in the automotive industry, jewelry manufacturing and designing end-user devices and appliances [2]. It is becoming more widely

used in many other industries and some rapid prototyping technologies are being marketed to consumers for personal use in their homes [3, 4].

In addition to limited-production manufacturing, rapid prototyping technologies have been extended for use in biomedical device fabrication. Rapid prototyping technologies have been used for the creation of patient-specific physical models used for temporary implantation such as mould-assisted implant fabrication [5], aids for complex surgery [6], bone fracture fixation devices and artificial hips or knees. Biodegradable materials have been developed for use with 3D structuring methods to fabricate temporary tissue scaffold structures. They are used in combination with seeded cells and/or biologically active compounds to induce the generation or regeneration of tissues in vitro or in vivo [7, 8]. Water soluble monomers have also been developed, allowing cells to be encapsulated within the material and because the hydrogel is able to swell with large amounts of water, the material can be made to resemble the physical characteristics of soft tissue. By encapsulating cells in fabricated hydrogel structures, higher cell densities and more control over cellular distribution can be achieved than by seeding into prebuilt porous scaffolds [9, 10]. Additionally, hydrogels can be designed to degrade within a given time frame or at the presence of a chemical compound [11], enhancing tissue formation and health.

Tissue scaffold and prototype production require fabrication of a static 3D structures, however, 3D physical structuring methods can also fabricate physical structures intended to be dynamic, known as microelectromechanical systems (MEMS). MEMS are miniaturized mechanical and electro-mechanical devices and structures, and can be extremely complex electromechanical systems with multiple moving elements under the control of a microprocessor. There are many large sub-fields of MEMS including: optical MEMS(e.g., deformable mirror device [12]), RF MEMS [13](e.g., switches, resonators), and biological MEMS (e.g., microfluidics, medical devices). In all of these sub-domains of MEMS fabrication, the use of polymer materials has become more prevalent.

Polymer materials have increasingly been used in MEMS fabrication because they can

provide greater mechanical yield strain in comparison to silicon [14], lower cost, substrates in non-wafer form factors, more complex structuring techniques, and unique chemical, structural and biological functionalities [15] not available in other material systems. The most frequently used polymers in MEMS applications are polyimide, acrylics, photopatternable epoxy (SU8), and polydimethylsiloxane (PDMS). In addition to these materials, other polymer materials including biodegradable polymers [16], functional hydrogels [17], fluorocarbon thin films, and conductive polymers [18] can be used for the purposes of conductors, sensors, actuators and drug delivery systems in MEMS. A list of highly used polymer materials and the MEMS applications associated with their use is shown in Table 1.1.1.

Table 1.1: Polymer MEMS materials and applications [19]

Material	Application
Acrylates	Microfluidics
Polyimide	Sensor substrates, microfluidics
PDMS	Microfluidic channels, pumps, and valves
SU-8 epoxy	Artificial haircell sensors
Polyurethane	Structures
Nanocomposite elastomers	Conductors, sensors, actuators
Biodegradable polymers	Drug delivery systems

In addition to materials design and development, three dimensional structuring technology for polymer MEMS processing is an active area of research with many unresolved problems. Three dimensional structuring methods must be able to provide large area processing, polymer-semiconductor integration, and packaging solutions for many polymer MEMS applications to be realized. Therefore, new structuring techniques will increase the range of devices that can be fabricated.

1.1.2   Motivation for index structuring

In addition to being able to control a polymer material's physical 3D distribution, greater control of the 3D distribution of refractive index in polymer materials is also being investigated. A spatially-changing refractive index distribution within a material can change the light propagation characteristics through the material, and can be exploited for a variety of applications. The most common example is a lens, a curved piece of glass that bends light through a single change of refractive index at an air/glass interface. However, a single change in refractive index limits how much control one has in the light propagation characteristics. To increase control, lenses are designed with multiple glass elements with different refractive indicies which improves the imaging performance of the lens. Arbitrary 3D control of the refractive index distribution is important in a large range of optical device technologies, such as transformation optics, optical data storage, and photonic device fabrication.

Structured artificial material that has spatially changing optical properties enables novel control of light. For example, a material can be structured in such a way that light is steered around an object within the structured material to make it appear invisible [20, 21]. The mathematical technique that enables the design of such artificial materials is called either transformation or conformally mapped optics [20, 21]. Transformation optics has become a tool for designing a wide variety of new optical effects and devices. The theoretical and mathematical basis of transformation optics has been known for over fifty years [22], however, the transformed dielectric permittivity and magnetic permeability tensors can take on almost any local value, including negative values, and therefore not subject to physical constraints of natural materials. The gap between mathematical theory and what could be fabricated was bridged with the advent of metamaterials [23, 24], which not only broadened the realm of possible values for both the dielectric constant and magnetic permeability to the negative territory, but also extended their combined effect in generating negative refractive materials [25–29]. Demonstration of negative index of refraction materials have thus far been

limited to structuring metals in such a way that the bandwidth of the light is within the resonance of the metallic structure. However, this results in nearly complete attenuation of the propagating light within tens of microns. To avoid strong attenuation, metamaterials designed entirely from dielectric materials have been demonstrated [30, 31]. However, current fabrication techniques are either limited in throughput or resolution restricting the number of devices that could potentially be fabricated. Therefore, a 3D structuring technique with high throughput and resolution will be able to create additional devices not yet demonstrated.

Three dimensional index structuring can also be used for the fabrication of photonic devices. Photonic devices have a wide range of applications in fiber optic communication, imaging systems, manufacturing and medical devices. Devices such as gradient index (GRIN) lenses, microlens arrays, photonic crystal, waveguides, active devices, filters and resonators have been fabricated with current three dimensional structuring techniques. A new fabrication method could potentially improve the performance, scale and/or cost of these devices.

Three dimensional index structuring methods have also been investigated for optical data storage. By encoding data through a localized refractive index change, data can be written and read out in a thick three dimensional volume [32]. Three dimensional methods storage have many advantages over current two dimensional storage implementations. Two dimensional approaches of conventional storage technologies have limited storage densities and data transfer rates because of limited recording area and serial data recording and recovering. Three dimensional approaches increase the potential storage capacity by orders of magnitude [33] and parallel data recording and recovering can be implemented [34].

1.2   Current fabrication methods

1.2.1   Physical patterning methods

Three dimensional physical structuring is currently accomplished by additive lithography, multi-layer planar lithography or LIGA (German acronym for Lithographie, Gal-

vanoformung and Abformung). Multi-layer planar lithography is capable of sub-micron 3D resolution with a continuous throughput of over 10^{12} features per second. However, each high-throughput 2D lithographic exposure is followed by hours of processing in a series of tools, limiting the number of layers and aspect ratio. LIGA is capable of sub-micron resolution, high aspect ratio structures but at an increased cost compared to multi-layer planar lithography. Additive lithography techniques are currently not capable of sub-micron resolution, but can reach higher aspect ratios, have higher throughput and lower cost than either planar lithography or LIGA.

Additive lithography refers to a group of methods that fabricate 3D objects made of a variety of materials from a computer aided design (CAD) model. Rapid prototyping techniques are additive processes [35], where successive layers of either liquid, powder or solid material are deposited and fused together in the shape of the 3D CAD model. Stereolithography (SLA) was the first rapid prototyping technique developed [36] and continues to be the most widely used rapid prototyping method. In SLA, the fabrication of the 3D objects is done by spatially controlled solidification of a liquid resin by polymerization. A laser is angularly scanned and subsequently focused onto the material surface, solidifying a defined depth of the resin causing it to adhere to a support platform. After polymerization of the first layer, the platform is moved away from the surface and the built layer is re-coated with the liquid material. The exposure process is repeated, and the second layer is adhered to the first layer as it cures. Good adherence of the second layer to the first layer is ensured by setting the depth of curing slightly larger than the platform step height. These steps are repeated for the remaining layers, solidifying the resin in the form of the defined 3D object. Objects which have overhangs must be supported during the fabrication process by support structures, which are manually or automatically designed with a CAD program used for SLA. The transverse and depth resolution of a 3D object built with SLA is approximately 20-100 μms, depending on the process and material used [37, 38]. Micro-stereolithography (μSL) [39–41] improves resolution compared to SLA by using higher numerical aperture (NA) op-

tical components to produce a μm radius focus. To enable the use of a μm radius focus in laser scanning systems, a closed-loop focus servo implementation is required to compensate for the reduced depth of focus [39]. To improve throughput over a single scanning point, a deformable mirror device [42] or liquid crystal display [43] can write up to 2 million features simultaneously. Transverse and depth resolution under 5 μms has been demonstrated for both implementations. Upon completion of the fabrication process in both SLA and μSL, the solidified 3D object is removed from the vat and the supports are removed from the object. The 3D object is then washed of excess resin and post-cured with ultraviolet light, polymerizing the remaining reactive groups within the object, improving the mechanical properties of the structure.

To fabricate structures with sub-micron resolution in all three dimensions, two photon absorption can be used [44]. Two photon absorption is utilized to restrict out-of-focus response and confine the polymerization to the focal volume. To create the micro-structure, a focused beam from a high NA objective is raster scanned through a material with a low one-photon absorption and a high two-photon initiation cross section. The non linear response to intensity and the high NA objective enables 100 nm features to be written for micro-structures [45] and MEMS devices [46]. Unfortunately, two photon absorption requires a large photon flux for sufficient excitation, so a femtosecond laser must be focused to a single point to achieve the required power density. However, the single focus requires rastering through a large number of voxels, making the fabrication rate for the polymer structures orders of magnitude smaller than conventional SLA, limiting structures to small voxel count.

Many applications require 3D objects made of materials other than polymers, such as metals and ceramics, but the rapid prototyping technologies presented thus far have been optimized for the creation of polymer 3D objects. Ceramic and metal 3D objects have been demonstrated using the SLA process [47, 48], however the 3D objects have poor fidelity. The SLA process fabricates ceramic and metallic 3D objects by dispersing ceramic [47] or metallic [48] particles into the liquid resin. To complete the 3D object the polymerized resin

is removed by sintering, leaving only the ceramic or metallic material in the intended 3D shape. However, it has been demonstrated that the sintering process deforms the ceramic or metallic 3D object because the particle density must be kept low to keep the liquid resin's viscosity within operational specifications of SLA. Selective Laser Sintering [49, 50] (SLS), can fabricate 3D ceramic and metal objects directly from metal and ceramic powder without the use of any intermediate binders or other materials. In the SLS process, a thin layer of powder is deposited by a roller onto a fabrication platform and preheated to a temperature slightly below the material's melting point. A CO_2 laser beam traces a cross-section of the part on the powder surface to heat the powder up to the sintering temperature, bonding the scanned areas together. When a layer of the cross-section is completed, the roller levels another layer of powder over the sintered one and the process is repeated until every cross section has been sintered and the 3D metal or ceramic structure has been formed.

Another technology that uses powder as the base additive material is three dimensional printing (3DP) [51, 52]. In 3DP, layers of powder are applied to a substrate, similar to SLS, and then is selectively joined together, in the 2D pattern of the cross section, using a binder sprayed through a nozzle. The resolution is dependent on the size of the binder droplets and the powder grains, the placement accuracy of the nozzle and how efficiently binder diffuses through the powder. When a layer of the cross-section is completed, another layer of powder is applied to the previous layer and the process is repeated until all the layers have been fabricated. The part is then heated to set the binder and the excess powder is removed by immersion in a water bath. To complete the 3D part the binder is removed by sintering.

Processing the material as liquid or powder limits what materials can be used. By processing a solid instead of a liquid or a powder, materials such as paper, fabrics, synthetic materials, and composites can be used in addition to polymers and metals. One such process is laminated object manufacturing, where stacks of sheets are cut to a desired 2D cross sectional shape and glued to each other to fabricate the 3D object [53, 54]. Each sheet is first glued to the stack, before the part's cross section is cut out by a laser beam. The

velocity and the focus of the laser beam is adjusted so that the cutting depth matches the thickness of the layer being cut, so the underlying layer is not damaged. Table 1.2.1 lists the various rapid prototyping technologies, comparing the advantages and disadvantages of each technology in terms of resolution, throughput and scalability.

Table 1.2: Comparison of Rapid Prototyping technologies

	SLA	μSL	TPDW	SLS	3DP	LOM
Material form	Liquid	Liquid	Liquid	Powder	Powder	Solid
Materials used	acrylates, epoxies	acrylates, epoxies	acrylates, epoxies	Nylons, Metals, polycarbonates, waxes	Cermaics, Metals	Papers, Plastics, Metals
supports req.	yes	yes	yes	no	no	no
Transverse Resolution	100μ m	2-5 μm	100nm	500 μm	100 μm	50μm
Depth Resolution	100 μm	3-40 μ m (object dep.)	100nm	200 μm(plastic), 20 μm(metal)	100 μm	150 μm(plastic), 100 μm(paper)
Throughput	100 mm^3/hr	1.2 mm^3/hr	.1 mm^3/yr	.25 mm^3/hr	5000 mm^3/hr	1000 mm^3/hr
Maximum object size	500x500x 580 mm	100x160x 100 mm	100x100x 100 μm	280x330x 380 mm	508x381x 229 mm	810x550x 500 mm

Rapid prototyping's main application is the fabrication of static devices and proto-types, such as small mechanical components, fluidic components [55], and complex geometric shapes. However, there has been great interest in combining rapid prototyping technologies and conventional silicon-based micro-machining because greater functionality could be obtained by hybridization. To this end, μSL has been combined to piezoelectric elements [56] and shape memory alloy wires [57] to create actuators. μSL has also been used for prototyping MEMS components and optimizing their geometry, before investing in equipment necessary for using conventional lithography in mass production [58]. Thus far, rapid prototyping technologies have not made a large contribution to the fabrication of MEMS systems because the technology is either not scalable(e.g.two photon stereolithography) or lacks sufficient resolution for most applications (e.g. microstereolithography). Therefore, the majority of MEMS fabrication is done by conventional lithographic technology.

For standard conventional lithography, aspect ratios are limited [59], but high aspect ratios in very thick resists is often a required for many fabricating micromechanical structures for MEMS or packaging applications. The LIGA process [60] is able to produce high aspect ratio, very small microstructures through deep X-ray lithography using synchrotron radiation, to pattern very thick polymethylmethacrylate (PMMA). The lithographic step is followed by electroplating metals on the structured PMMA. The LIGA process has fabricated microwave MEMS devices (e.g. transmission lines, filters, couplers, and antennas [61–63]), micromechanical MEMS devices(e.g. micromotors, microactuators, and geared micropumps [64–66]) and microfluidic devices [67]. However, large scale application of the LIGA fabrication process is restricted by the expensive X-ray source and the demanding mask technology required for the process.

1.2.2   Index structuring methods

Three dimensional index structuring is currently accomplished by multi-photon direct write lithography at a scanning point, multi-layer projection lithography of sequential 2D

planes or volume holography of entire 3D volumes. While sub-micron resolution is possible in all cases, throughput dramatically increases with dimensionality of the exposure but at the cost of flexibility in the type of structure that can be fabricated. In the case of direct-write lithography at a scanning point, multi-photon absorption is utilized to restrict out-of-focus response and confine induced changes to the focal volume. Unfortunately, multi-photon absorption requires femtosecond pulse length for efficient excitation. Glass is the most used base material and has high environmental stability, but requires irradiances of 10^{17} W/m^2 or larger [68] and device thickness is restricted to the working distance of an oil-immersion objective.

Most applications are sparse waveguide devices [69–72] due to throughput limitations, though dense 3D index patterns such as volume computer generated holograms (VCGH) [73] have been generated, however they only contain 64^3 index features. To increase throughput and eliminate depth restrictions, liquid polymers [74] containing photo-initiators with large two-photon cross-sections and polymerization chain-reactions to increase sensitivity are used. Sparse waveguide [75, 76] devices have been fabricated and scanning point exposures have created dense 3D structures including invisibility cloaks [77] and templates for a gold polarizer [78]. However, even with the increased throughput of polymers, the fabrication rate for the polymer structure of the invisibility cloak is 13 years/mm^3, because the necessary power density still requires rastering through a large number of very small voxels, limiting devices to sparse, typically binary structures with small voxel count.

To increase throughput over a scanning single point, a single two-dimensional exposure writes a multitude of index features simultaneously. Two photon absorption cant be used because response greatly reduces over a large transverse area, therefore one photon absorption must be used. However, one-photon absorption does not restrict out-of-focus response, so 2D exposures are typically done into a thin layer. Ultraviolet (UV) optical projection lithography is the most common and is currently capable of 22 nm resolution with a continuous throughput of over 10^{12} features per second. Repetitive projection lithography and

planarization enables both large area and arbitrary 3D structuring, demonstrated by the fabrication of a 3D optical metamaterial [30]. However, each high-throughput 2D layer is followed by hours of processing in a series of tools, currently limiting demonstrations to 3 to 30 layers.

The depth limit of sequential two-dimensional processing can be avoided by 3D holographic exposure. One photon diffusive photopolymers [79] enable self-developing 3D patterning of up to cm thick solid volumes. These materials contain two monomers [80], in which the first monomer thermally gels providing a physical scaffold for index structures. Incident light polymerizes the second monomer, locally depleting monomer in the exposed region. This causes diffusional mass transport of unreacted monomer into the exposed region, resulting in an increased material density and index of refraction, without solvents or thermal processing. A post-exposure optical flood cure is then done to bleach remaining initiator and cross-link all remaining monomer, desensitizing the material. The low required dose (100 mJ/cm^2) and wavelength sensitivity (UV to near IR) of these materials have led to applications in holographic data storage (HDS) [32]. Current holographic data storage (HDS) systems use the change in refractive index to encode the data by employing a page based architecture, where the Fourier transform of a data page is interfered in the photopolymer media with a plane wave reference beam. Data capacities up to 1.6 TB and 960 Mbit/s data rates are achieved through angle and polytopic multiplexing of the holograms written[81]. Although HDS systems have shown large capacity and fast data transfer rates, the drive architecture is complex and difficult to manufacture at a large scale. This motivates a simpler solution such as writing micro holograms in multiple layers of the same type of photopolymer as HDS [82]. However, SNR scaling and phase aberration limits [83] make scaling to many layers difficult.

These one photon diffusive photopolymers have also been used for the fabrication of photonic devices, such as waveguides [84], holographic filters [85], and GRIN lenses [86]. Using one photon absorption materials for photonic device fabrication has potential ad-

vantages over multi photon absorption systems, such as greater writing flexibility, larger throughput and the potential to integrate other optical circuitry within the photopolymer material. However, one photon absorption in solid, thick materials does not yield complete control of the 3D index distribution due to diffraction.Additionally, the required diffusion time for development increases quadratically with scale, limiting practical feature size to 100s of microns [86].

1.3   Thesis overview

This thesis presents a new fabrication process, liquid deposition photolithography (LDP), for the fabrication of sub-micron resolution 3D index and physical structures. Chapter 2 is an introduction to the LDP fabrication process. The process steps of the method and a reaction/diffusion model are presented. The individual parts of the process are detailed and results of single and multiple superimposed layers written into a volume of photopolymer are presented. To demonstrate LDP's ability to manufacture photonic devices, a waveguide array containing over 3,000 waveguides is fabricated. Chapter 3 describes the photopolymer used in the LDP fabrication process. The photopolymer is a two-component mixture, where both components are liquid photopolymers. The formulation of the diffusive photopolymer and how the photopolymer achieves high index contrast is presented. The amount of control over index structure formation is investigated by quantifying the fidelity of refractive index recordings. Chapter 4 describes the fabrication of GRIN structures with nearly arbitrary index profiles. To fabricate nearly arbitrary GRIN profiles, the optical system is redesigned to include a deformable mirror device (DMD). Exposure parameters that result in high fidelity, high contrast GRIN recordings are presented. Chapter 5 presents a thorough study of the chamber window and the dynamics of oxygen diffusion in the LDP process. A model of the photo-chemical processes in LDP is presented and experimentally validated using a test setup called the pull tester. The model and experimental results show that the chamber window has a finite lifetime if used in a rapid fabrication, but can be extended if delay

is introduced between exposures. Finally, Chapter 6 summarizes the current state of the work presented in this thesis. It provides suggestions for future work that could continue to advance the capabilities of LDP and optimize the current implementation.

Chapter 2

Liquid Deposition Photolithography

2.1 Introduction

In this chapter, I present a new fabrication process, liquid deposition photolithography (LDP), for efficiently fabricating sub-micron resolution 3D index structures within diffusive photopolymers. The fabricated 3D index structures have an index contrast up to 0.1, 100 times larger than femtosecond micromachining and 20 times larger than commercial holographic photopolymers, allowing greater flexibility in photonic device fabrication. It can efficiently create mm^3 optical devices with programmable, gradient index of refraction at simultaneous scales from 100's of nm to mm.

The 3D volume is created through repetitive layering of the liquid photopolymer, where each layer is structured by projection lithography. Every processing step is performed on a single instrument, vastly reducing fabrication time compared to multi-layered semiconductor lithography. The process has the unusual property that total fabrication time for a fixed thickness decreases as the number of layers is increased, enabling fabrication 10^5 faster than femtosecond micromachining. The high throughput and index contrast is demonstrated by sequentially writing 100 layers to fabricate a mm thick waveguide array that has a fabrication rate of 1.2 mm^3 per hour.

2.2   Process steps

The process steps for LDP are shown in Figure 2.1. The LDP process requires a lithographic chamber that can inject liquid photopolymer into the exposure chamber, a moving platform connected to a high precision stage and a chamber window. Layers are created by drawing liquid monomer through a microfluidic gap between the chamber window and platform created as the platform is lowered. The layer thickness is controlled by the distance the platform is lowered, enabling sub-micron precision [87] of layer thickness. Two dimensional (2D) projection lithography through the chamber window structures the index of each layer and the process repeats. The chamber window provides optical access and prevents stiction by maintaining a thin liquid layer at the top of the polymer, allowing many layers to be written.
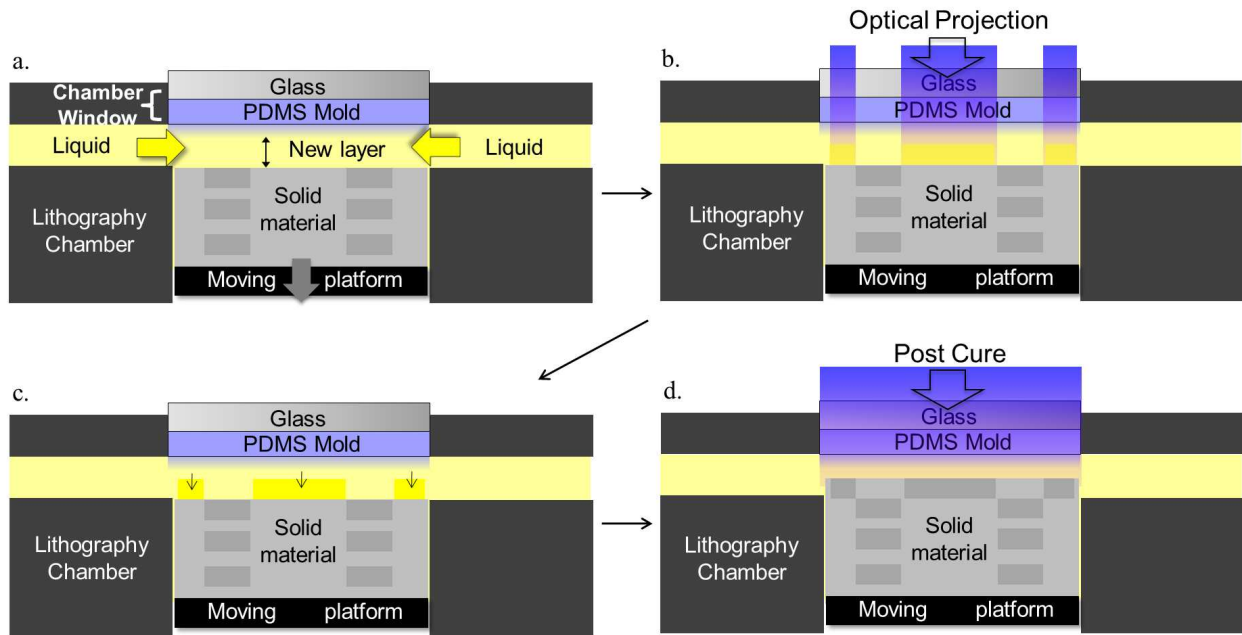
Figure 2.1: Steps of Liquid Deposition Photolithography (LDP) process. (a) UV sensitive liquid monomer is drawn through a microfluidic channel created as the platform is lowered, producing a new layer. (b) The new liquid layer is patterned by 2D projection lithography, using 365 nm light, polymerizing the liquid monomer into the 2D pattern. (c) Unreacted monomer diffuses from this adjacent layer of liquid monomer into the solid to replace that consumed by polymerization, increasing the material density and index of refraction in the exposed region. (d) The entire layer is optically flood cured, using 365 nm light, to a solid, cross-linked, photo-insensitive polymer. Steps (a-d) are then repeated until the entire volume is fabricated.

Processing time in LDP is reduced compared to conventional lithography because the entire process is completed on a single instrument. Therefore, the separate instruments for each step of the process are not required, including the mask-to-substrate alignment, layer planarization, and chemical and thermal processing. Thermal and wet processing steps can be eliminated because the material used is a self-developing diffusive photopolymer that does not require the additional processing to develop, which is not the case for the resists used in conventional lithography. Similar to conventional lithography, transverse resolution is a function of the projection optics, material response and layer thickness, while axial resolution is determined by layer thickness. In LDP, the layer is not spin coated but, instead, fluid is deposited by the motion of a stage with nanometer resolution and planarized by the chamber window, enabling thin layers to be fabricated.

2.3   Features of LDP

2.3.1   Large throughput

LDP has large throughput and can create large scale transverse structures because the liquid layer enables longitudinal diffusion and creates a short diffusion path for unreacted monomer. The time to fabricate a single layer consists of the mask translation and settle time, exposure duration, and monomer diffusion time. By Fick's law, the diffusion time scales as the layer thickness squared while the exposure time is not dependent on layer thickness. Therefore, for a fixed part thickness, total diffusion time for all layers decreases linearly with layer thickness, as shown below in Figure 2.2. The relationship between axial resolution and fabrication time is therefore unusual, in that higher resolution results in faster write times. This relation breaks down for sufficiently thin layers where exposure duration and mask translation and settle time dominate. This enables the process to simultaneously have both high throughput and sub-micron resolution through the depth of the fabricated volume.
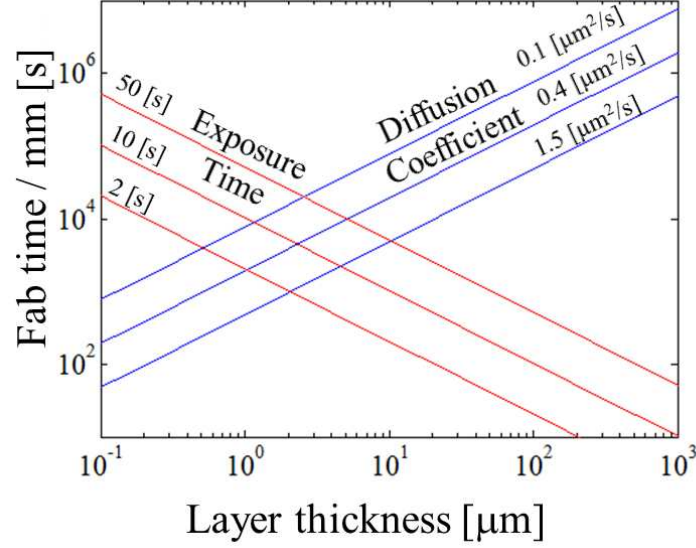
Figure 2.2: Throughput simulation of LDP. The total time required to complete exposure and diffusion of a one mm thick part as a function of the individual layer thickness for various per layer exposure times and diffusion coefficients for materials similar to the material used, described in Chapter 3. There is an optimal layer thickness, depending on both the exposure time and monomer diffusion constant. For materials with reasonable exposure times, 1-30 seconds, and diffusion coefficients, 0.1-1 μm^2/s, optimal layer thickness ranges from 1-10 μm with a total fabrication time ranging from 10^4 - 10^5 s/mm. The results shown here were created by a one-dimensional model of monomer diffusion.

To create Figure 2.2, a one-dimensional model of monomer diffusion was created. In the model only monomer diffusion was considered and a constant diffusion coefficient of monomer was assumed throughout space. Only longitudinal diffusion was considered, so fabrications with small transverse will have a different relationship between layer thickness and total diffusion time than what is shown here. With those assumptions the diffusion of monomer is described by the following equation

$$\frac{\delta[m]}{\delta t} = D_m \frac{\delta^2[m]}{\delta x^2} \tag{2.1}$$

Both the concentrations and time are normalized using

$$[M] = \frac{[m]}{[m_0]}, \quad t' = \frac{tD_m}{L^2}, \quad x' = \frac{x}{L},$$

where m_0 is the initial concentration of monomer, L is the thickness of the layer and D_m is the monomer diffusion coefficient. Time is normalized to the diffusion time of monomer across the layer. Space is normalized to the thickness of the layer. The nondimensional equation is

$$\frac{\delta[M]}{\delta t'} = \frac{\delta^2[M]}{\delta x'^2} \tag{2.2}$$

The boundary and initial condition are shown in Figure 2.3. The boundary condition of the left edge is set to one because diffusion of monomer in the liquid monomer layer is assumed to be much faster than in the gelled regions. A 1D PDE solver in MATLAB was used to find the normalized time it took to reach 85 percent monomer replacement via diffusion on the right boundary of the simulation. The diffusion time for each layer thickness was determined by the simulation.
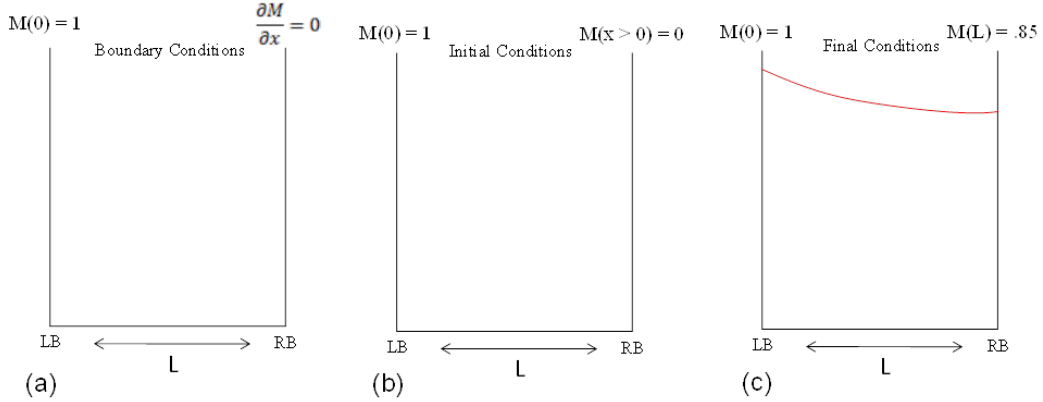
Figure 2.3: Boundary and initial conditions of the simulation. (a) The boundary conditions for the simulation. The flux of monomer on the right boundary (RB) is set to zero and the concentration of monomer, M, on the left boundary (LB) is set to a normalized concentration of one. (b) The initial concentration of monomer. The left boundary of the simulation is set to one and all other x coordinates are set to zero. (c) The 1D PDE solver in Matlab was time advanced until the concentration of the right boundary reached 85 percent monomer replacement via diffusion.

2.3.2   Decoupling lateral resolution from layer thickness

Repetitive layering allows multiple layers thinner than the depth of field of the optical system to be sequentially deposited and structured. This enables independent control of lateral and transverse resolution of refractive index structures written in one photon absorption photopolymers. Therefore, the aspect ratio of the fabricated refractive index structures, defined as the ratio of the structure's width to its height, are not limited by diffraction and could potentially be much higher than other photopolymer structuring methods.

To determine the layer thickness required to effectively decouple lateral and transverse resolution, transverse resolution as a function of layer thickness must be determined. In order to avoid exposure variations throughout the layer, the thickness can be no greater than the depth of field of the projected pattern. Transverse resolution and the depth of field for an optical system focusing a Gaussian beam [88] are respectively

$$\omega_0 = \frac{\lambda}{\pi NA} \tag{2.3}$$

$$2z_0 = t = \frac{2\pi \omega_0^2}{\lambda n} = \frac{2\lambda}{\pi NA^2} \tag{2.4}$$

where ω_0 is the transverse resolution, $2z_0$ is the depth of field, n is the refractive index of the material, NA is the numerical aperture of the optical system, t is the layer thickness and λ is the wavelength of light in vacuum. The lateral resolution as a function of layer thickness is

$$\omega_0 = \frac{\lambda}{\pi\sqrt{\frac{2\lambda}{\pi t}}} \tag{2.5}$$

The transverse resolution as a function of layer thickness is shown in Figure 2.4.

The transverse resolution reaches a minimum of 90 nm, as show in figure 2.4(b), because the numerical aperture (NA) of the projection system was limited to 1.3. The depth of field using a NA of 1.3 is approximately 100 nanometers which is larger than the boundary between the inhibited and exposed region as demonstrated in a subsequent section. Implying that LDP could use optics with a NA over 1 resulting in 100 nm voxel size in all dimensions. The
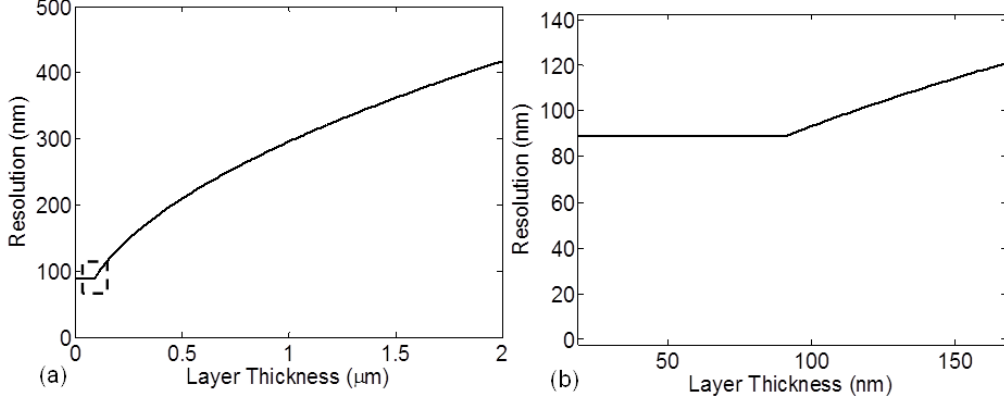
Figure 2.4: Plot of transverse resolution as a function of layer thickness. (a) Transverse resolution as a function of layer thickness. (b) Magnified image of minimum resolution.

100 nm achievable voxel resolution in LDP is comparable to achievable voxel resolution of femtosecond micromachining.

2.4   Implementation of LDP

2.4.1   The chamber window

The chamber window is critical to the LDP process because it prevents polymer adhesion to the window allowing thin layers to be written and it enables each thin layer to be structured by aberration-free projection lithography. The chamber window was originally developed to allow optical pattern access and prevent polymer adhesion to the window for efficient fabrication of micron-sized acrylate particles [89, 90]. We have extended the use to passively planarize new layers as a mold and maintain a monomer-rich liquid layer next to the exposed part. The chamber window performs these functions by providing a constant flux of oxygen at the liquid monomer boundary via diffusion from the PDMS layer. Oxygen is a strong radical inhibitor [91], so polymerization is prevented in the thin liquid monomer layer directly adjacent to the chamber window. Oxygen is used as the inhibitor because it is naturally present via atmospheric diffusion, is a well-characterized inhibitor of

radical polymerization and diffuses rapidly due to its small size. A reaction/diffusion model of the chamber windows is presented in Chapter 5, providing further details on the chamber window's operation.

Chamber windows are fabricated by adhering a flat, 125 μm layer of PDMS (Sylgard 184, Dow Corning) onto microscope cover slips (Ted Pella, 22 x 50 mm). To create a flat PDMS surface, uncured liquid PDMS is poured on optically flat BK7 float glass. To set the thickness of the PDMS layer, 125 μm spacers were placed at the edges of the BK7 float glass. Treated cover slips were then placed on top of the liquid PDMS and casted against the float glass. To promote PDMS adhesion to the cover glass and prevent PDMS adhesion to the BK7 float glass, they were treated with Dow Corning P5200 adhesion promoter and (Tridecafluro-1,1,2,2 tetrahydroctyl) Trimethoxysilane respectively. The samples were put in an oven at 100 degrees Celsius for 2 hours to thermally cure the PDMS. After removal from the oven, the cover slips with PDMS adhered to them were peeled off the float glass and the exterior of the cover slip was cleaned with methanol.

The second function of the chamber window is to enable aberration-free projection lithography and thus the phase flatness of the chamber window must be verified. To demonstrate the optical quality of the chamber window, a wavefront sensor was used to measure the phase of the chamber windows by using the setup shown in Figure 2.5. Surface variations on the PDMS side do not impact optical imaging quality since PDMS is very well index matched to the liquid monomer. To remove the surface variation from the optical path length measurement, a piece of BK7 float glass was attached to the PDMS side of the chamber window.

As shown in Figure 2.5b the root mean squared (RMS) optical path difference(OPD) was measured to be .026 waves, demonstrating there are no significant lateral optical inhomogeneities in the PDMS of the chamber windows. The measured RMS OPD of the chamber window will be slightly different at 365nm compared to our test wavelength of 532 nm. However, since the PDMS exhibits no absorption at 365 nm [92], dispersion or non-

a

532 nm Compass Laser | Spatial filter | Chamber Window | Wavefront Sensor

b

Size in mm (object space)   P-V OPD (Waves): .1654

OPD (wv)
Avg: -.024
RMS: .026
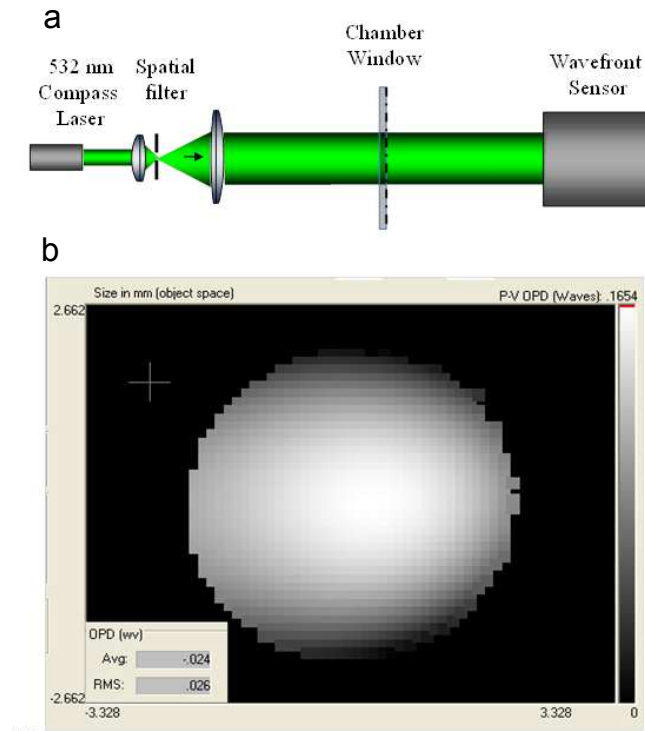
Figure 2.5: Optical quality of the chamber windows. (a) The optical setup to test quality of chamber windows using a Wavefront Sciences Shack Hartmann wavefront sensor. (b) Image of wavefront error calculated by the Wavefront Sciences Shack Hartman wavefront sensor.

linear effects will be minimal and the RMS wavefront will scale with the wavelength, still providing diffraction limited performance.

2.4.2   Optical system

The optical projection system, shown in Figure 2.6, creates the illumination for the processing steps of LDP by imaging 2D patterned light and unstructured post-cure light onto the LDP sample plane.

Chrome-on-glass photomasks were used for the initial demonstrations of the process, but programmable masks (DMDs, liquid crystals, and galavometers) have been shown and are used in subsequent work within this thesis. The photomasks used were designed in
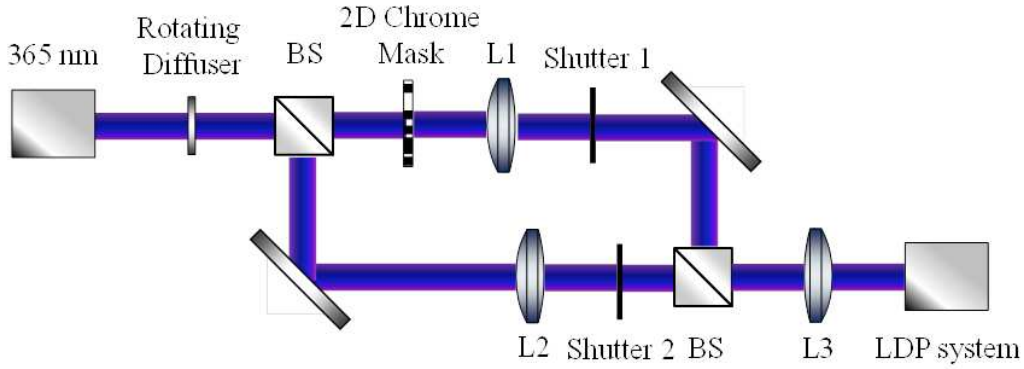
Figure 2.6: Optical setup of mask and post cure projection system. When shutter 1 is opened, 2D patterned light, created by the 2D chrome mask, is imaged onto the LDP sample plane, creating the 2D structure. When shutter 2 is opened, unpatterened post cure light is imaged onto the LDP sample plane, bleaching the remaining initiator and cross-linking all remaining monomer. The rotating diffuser was used to break the spatial coherence of the UV light source and eliminate interference effects. The focal lengths of lenses L1, L2 and L3 are 120 mm, 80 mm, and 80 mm respectively.

CleWin and printed on a chrome mask using a Heidelberg DWL 66FS at the Colorado Nanofabrication Lab (Boulder, Colorado). The mask was then inserted into the optical setup. An Innova 300C argon laser served as the source of UV light. An engineered 20 degree circle pattern diffuser from Thorlabs was mounted on rotation stage and driven by a DC motor to create the rotating diffuser. Two VS35 shutters (Uniblitz) driven by a computer-controlled VMM-D1 shutter driver provided specified pulses of UV light. The lenses in the projection system (L1, L2, and L3) were Edmund Optics doublets and measured 2 in diameter.

2.4.2.1 Effect of coherence of source on fidelity of structures

The optical system was originally designed to use a Innova 300C argon laser as the light source. However, the index structures fabricated using the laser contained interference fringes from the edge of the mask. An example of an index structure exposed with a coherent light source is shown in Figure 2.7(a), demonstrating the interference fringes.

In addition to using an ND filter to reduce reflections from the platform, an engineered

a. b.
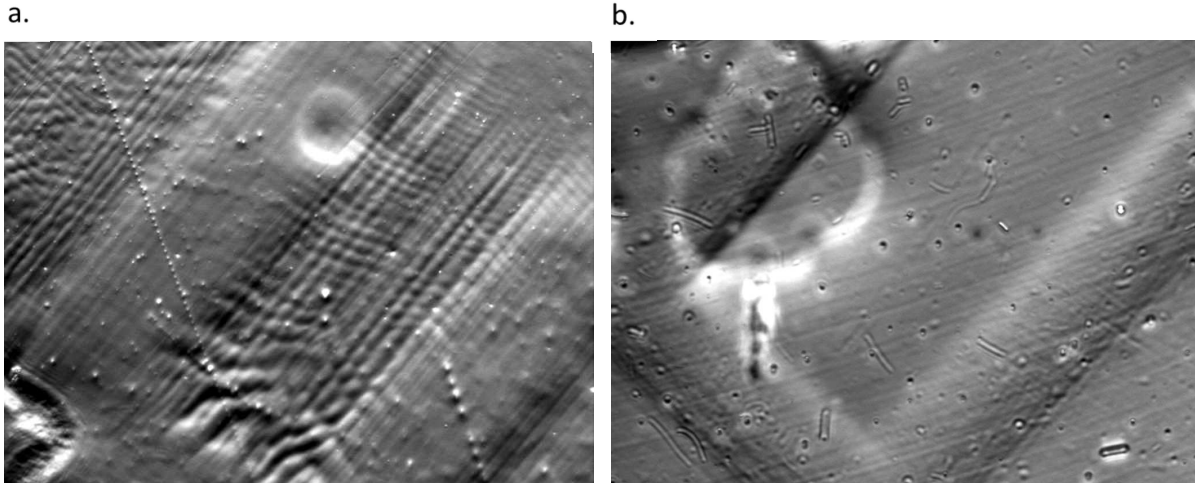
Figure 2.7: DIC images of the same index structure exposed with and without using a diffuser. (a) Index structure fabricated with a coherent source. (b) Index structure fabricated with a diffuser to reduce spatial coherence of the illumination.

20 degree rotating diffuser was incorporated into the setup to reduce the spatial coherence and the interference distortions associated with a coherent source. To demonstrate the improved fidelity using incoherent light, a second index structure was exposed under the same conditions as Figure 2.7(a) but with the addition of the rotating diffuser, shown in Figure 2.7(b). The index structure no longer has the interference fringes adjacent to the exposed structure, improving fidelity. Without the fidelity improvement from using an incoherent source, LDP's ability to fabricate useful 3D structured volumes would be severely diminished.

2.4.3   Fabricating multiple layers of binary index structures

There are multiple ways to create the dynamic two dimensional pattern to structure each layer within LDP. In the following sections different implementations will be outlined and potential strengths and limitations of each implementation discussed. Each of these projection methods have been implemented in other photopolymer structuring systems, particularly in stereolithography apparatus, so many of the advantages and issues with each method are well known. Many of these techniques can be extended for gray scale imaging

and fabrication of GRIN structures, as will be discussed in Chapter 4, but the focus of this section will be on the fabrication of multiple layers of binary index structures.

2.4.3.1   Multiple chrome on glass masks

A potential way to create a 2D pattern generator is to use a large chrome on glass mask containing multiple patterns, which is dynamically translated transversely by computer-controlled stages. This enables multiple patterns to be projected onto the image plane without realignment of the sample. A single chrome mask written by a Heidelberg 66fs, a common mask writer, is capable of 0.6 μm resolution over an area as large as 200 by 200 mm^2 [93], enabling over 110 Gbits of data to be transferred to the fabricated volume within the duration of the exposure. An example of this configuration is shown in Figure 2.8.

To create multiple binary light patterns, the chrome-on-glass mask must be translated to the next pattern after each exposure. If the number of pixels for each binary pattern is equivalent to the 2D area of the largest DMD (1092x1080), patterns are separated by a approximately one millimeter. Transverse stages can travel at 300 mm/s and have a settling time of 250 milliseconds [94]. Therefore, the settling time dominates the mask translation time, so binary patterns can be changed at a rate of 4 Hz. This is much slower than a DMD, which can be modulated at 30 KHz, but this is still approximately two orders of magnitude less than the exposure time so mask translation time is not significant relative to exposure. A 200 by 200 mm^2 chrome-on-glass mask has approximately 110 Gigapixels which is over five order of magnitude larger than DMDs, which have approximately 2 Megapixels. Therefore, a single chrome-on-glass mask can create 55,000 binary patterns with the same information content as a single DMD image. There are different costs associated with each implementation. The chrome-on-glass implementation requires two translation stages, a motion controller and the chrome-on-glass mask. The cost of the translation stage and motion controller can range anywhere from $8,000-30,000 depending on the accuracy and precision of the transverse stages. The cost of each mask can range from $200-5,000 depending on the
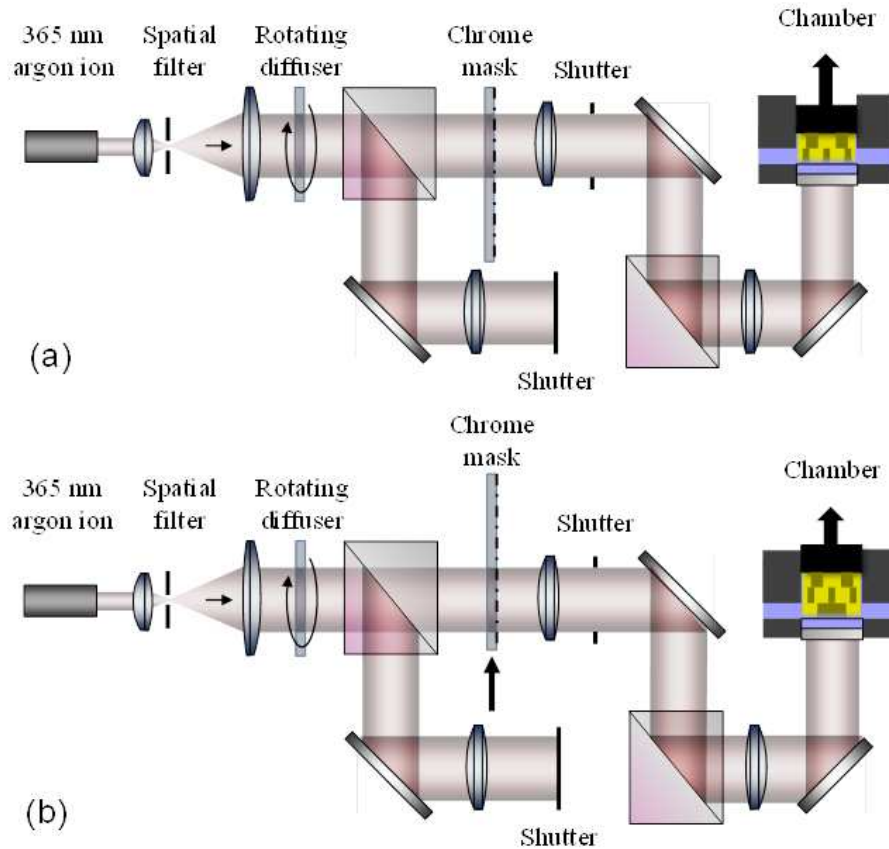
Figure 2.8: System diagram of creating multiple 2D transverse patterns within LDP. a, Writing layer n by aligning chrome mask plane and sample planes to be conjugate and projecting pattern n onto the sample plane. b, Writing layer (n+1) by translating the large chrome mask to a new position within the mask plane and then then projecting pattern (n+1) onto the sample plane.

availability of a mask writer. Additionally, when binary patterns beyond what is already on the chrome-on-glass mask are required, a new mask must be fabricated which has an additional cost and lead time. The cost of a DMD can range from $8,000-25,000, but after purchased a DMD does not require additional materials.

2.4.3.2   Laser scanning system

Laser scanning was the first 2D pattern generator developed for stereo-lithography systems. In this method, a focused laser is scanned over the surface of a film to generate

the 2D pattern. There are two ways to implement a laser scanning system, either using scanning mirrors or multiple translation stages. In the scanning mirror implementation, the 2D pattern is created by deflecting a focused laser beam to an array of x-y positions. In the multiple translation stages implementation, the 2D pattern is created by translation of the material through a focused laser beam. An example of both types of laser scanning systems are shown Figure 2.9. High resolution and throughput is achieved by using a microscope objective to obtain a sub-micron focal volume with light irradiances of 10^4 W/m^2 or larger. The binary pattern can be modulated up to 1 Hz [95], an order of magnitude smaller than the exposure time. A pair of linear stages with 20 nm precision and 200 mm of travel can be used to create 10^{14} pixels in a single image.
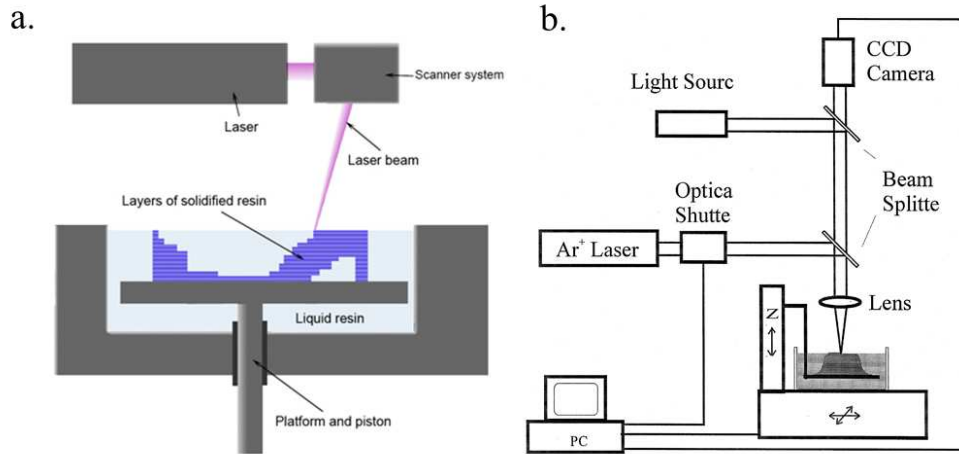
Figure 2.9: Illustrations of two implementations of laser scanning systems. (a) An example of using a galvanometer as a dynamic 2D mask [96]. (b) An example of using translation stages to move the vat of material through a focused laser beam to dynamically create a 2D mask [39].

2.4.3.3 Liquid crystal display

A straightforward way to create two dimensional patterns that do not need transverse alignment is to image a liquid crystal display (LCD) onto a fixed sample. LCD are made

of pixels separated by thread of electrical connections that are used for their control. Each pixel of an LCD typically consists of a layer of liquid crystal molecules aligned between two electrodes, and two polarizing filters, the axes of transmission of which are perpendicular to each other. An applied electric field across the transparent electrode, usually made of ITO, induces a change in the orientation of the liquid crystal molecules causing a rotation of the polarization of the incident light. Common LCDs have a pixel size of 20-30 μm and a 100:1 contrast ratio [42]. The binary pattern can be modulated up to 500 Hz [97], two orders of magnitude faster than a chrome-on-glass mask.

There has been multiple implementations of an LCD as a dynamic 2D mask, with the application closest to LDP being stereo-lithography. Since most LCD's are not compatible with UV light because it damages the liquid crystals, stereo-lithography setups had to incorporate a visible light source and an initiator sensitive to visible wavelengths [98] in order to use them. LCD transparent to wavelengths around 350nm can be fabricated in order to use UV initiators [43], however they are expensive and have short lifetimes. An example a LCD being used as a dynamic 2D mask is shown Figure 2.10.

2.4.3.4   Deformable mirror device

Another common way to create multiple two dimensional planar patterns on a sample without constant realignment is to image a DMD onto the sample. DMDs are made of highly reflective, digitally switchable mirrors organized in a two-dimensional rectangular array. Each aluminum micromirror is approximately 10.8 microns in size, and is switchable between two discrete angular positions: $12°$ and $+12°$. The pattern on the DMD is controlled by dynamically modulating the pixels at over 30 kfps through computer control. DMD's have a pixel size of 10.6 μm and a contrast ratio of 350:1 [42]. Additionally, the aluminum micromirrors coated for UV illumination enable higher modulation efficiency and longer lifetimes compared to LCD displays. The largest DMDs have an data transfer capacity of 2 MB for a single exposure. If layers require pixel counts of 2 MB or more, layers can be written using a
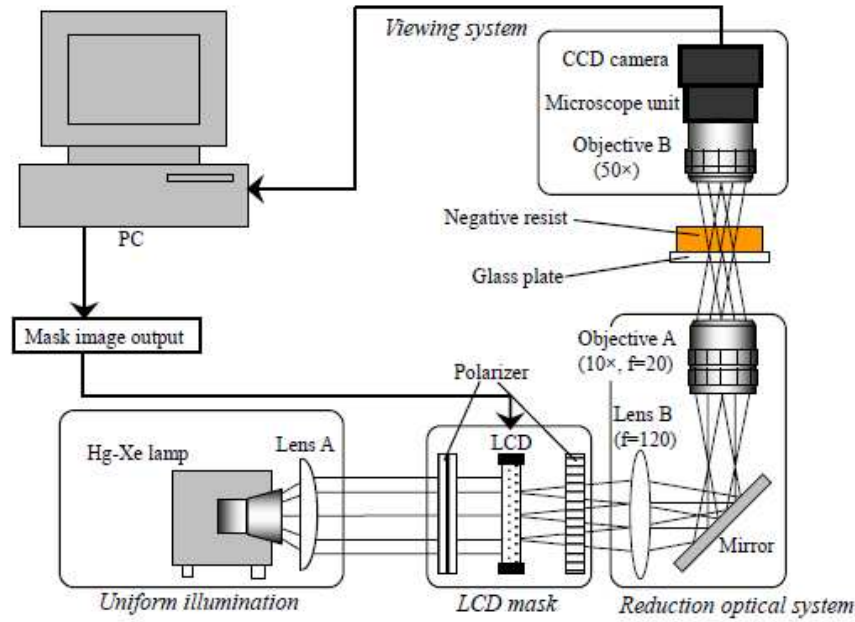
Figure 2.10: An illustration of using LCD as a dynamic mask in an optical system [99].

step and repeat process [100]. This process requires additional translation stages, increasing the implementation cost.

2.4.3.5   Comparing the methods

Table 2.4.3.5 lists the structuring technologies, comparing the advantages and disadvantages of each technology in terms of resolution, throughput and cost.

2.4.4   Mechanical design of lithographic chamber and platform

LDP differs from SLA and other additive lithography methods through a closed exposure chamber. This closed exposure chamber creates the chamber window/liquid polymer boundary, produce new photopatterable liquid layers, and hold additional liquid photopolymer for subsequent layers. Two designs for the lithographic chamber and platform were implemented with both a bottom and top window geometry.

The first platform developed was a metallic cantilever connected to a Newport GTS-

Table 2.1: Comparison of binary pattern generators

	Chrome mask	Scanning system	LCD	DMD
Resolution	0.6μm	0.2μm	30μm	10.6μm
Contrast	>1000:1	-	100:1	350:1
Modulation rate	4 Hz	.5-1 Hz	500 Hz	30 kHz
Number of pixels	110 x 10^9	10^{14}	1 x 10^6	2 x 10^6
Wavelength range	300-1200 nm	300-1200 nm	450-1200 nm	325-1000 nm
Capital cost	$10,000 - 35,000	$20,000 - 80,000	$10,000 - 25,000	$8,000 - 20,000
Additional cost	$200 - 4,000	-	-	-

30V, a high precision vertical linear stage, that was vertically actuated to create a new layer of liquid photopolymer. A neutral density filter was epoxied to the metallic end of the cantilever, which suppressed reflections within the chamber and increased the optical clarity of the polymerized material. This is similar to bottom anti-reflective coatings (BARC) used in planar photolithography to reduce reflections off the surface of the substrate [101].

The lithographic chamber was designed to hold the chamber window in place and create a vat for liquid photopolymer material needed for the entire exposure. In order to be able to load the chamber window into the lithographic chamber, the chamber was fabricated into two separate metallic pieces that could be attached and detached using screws. The bottom metallic piece had a four millimeter diameter hole cut through the middle of the part, setting the photo-patternable transverse area, and a slot with the dimensions of the chamber window cut into it to register the chamber window to the exposure area. The depth of the cut was 10 μm smaller than the thickness of the chamber window in order to seal the chamber using the compliance of the PDMS. An image of the lithographic chamber and platform, as illustrated in Solidworks, is shown in Figure 2.11.

The original lithographic chamber and platform design produced the results shown
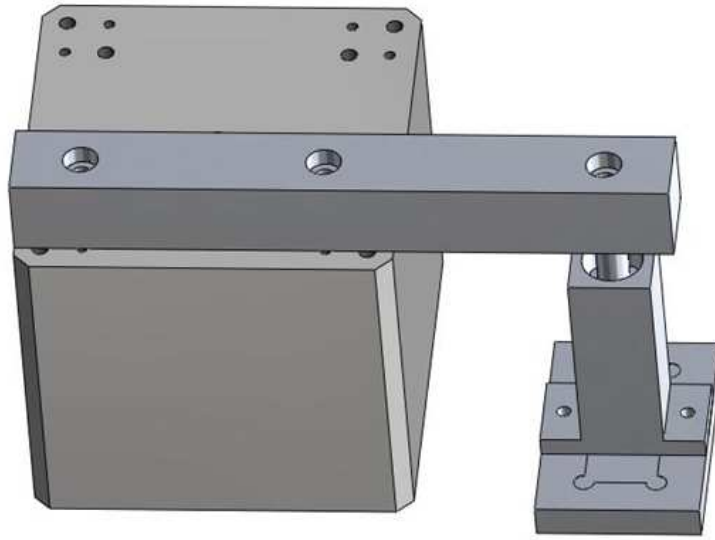
Figure 2.11: The original lithographic chamber and platform design

in this chapter, however, the transverse field and fidelity of the volumes fabricated were limited by the chamber and platform design. The flatness of the ND filter attached to the platform could only be controlled to +/-0.5 degrees from center. This limited the minimum layer thickness of the first layer and produced a wedge at one end of the fabricated volume. Additionally, the finished part had to be peeled off the ND filter in order to remove the part from the platform. This caused mechanical strain within the volume, creating birefringence and exposing the fabricated volume to additional contamination. Those issues motivated a new chamber design that had better control of layer thickness, didn't require using a razor blade to remove the fabricated volume from the platform and increased the photo-patternable transverse area. An image of the newly designed lithographic chamber and platform, as illustrated in Solidworks, is shown in Figure 2.12.

The new design, as shown in Figure 2.12, consists of three separate pieces: the platform(referred to as the piston), the chamber and the Newport GTS-30V stage which actuates
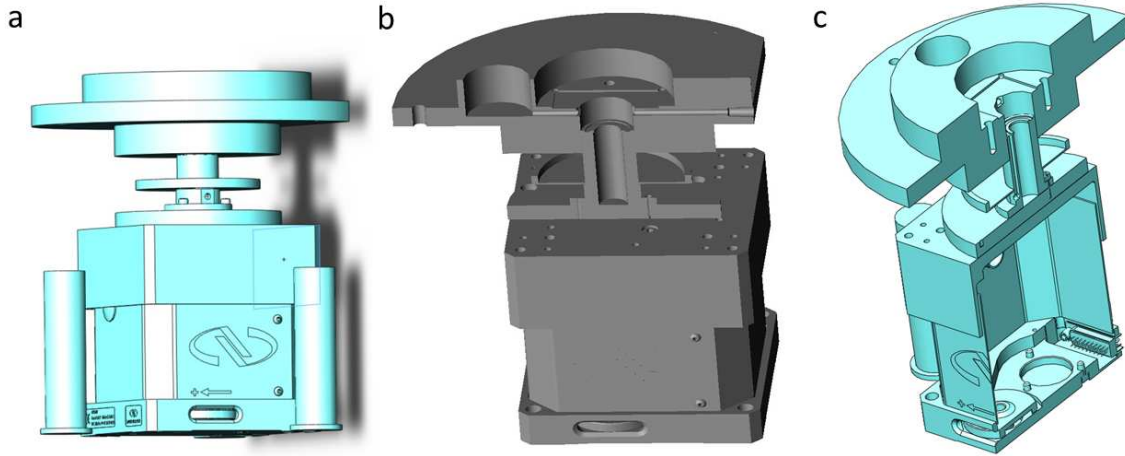
Figure 2.12: The new lithographic chamber design. The new chamber increases the transverse patternable area, enables greater fluidic control of liquid materials, has a flatter transverse field and greater control over the 3D index distribution. (a) zoomed out view of piston, chamber, and Newport stage connected together. (b) side view of cross section of the piston and chamber. (c) angled view of cross section of the piston and chamber.

the piston to inject liquid layers. The patternable transverse area increased from 4 to 12.7 millimeters, set by the diameter of the ND filter at the center of the piston. The new lithographic chamber required a change in form factor of the chamber windows, from 50 by 22 millimeters to 50 by 35 millimeters, however, the change in form factor does not require a fabrication process change. To avoid peeling the fabricated volume from the ND filter, a 25 mm diameter, 3 millimeter thick BK7 window is attached to the piston and index matched to the ND filter of the piston. To retrieve the fabricated volume the piston was removed from the stage and placed in the oven for 45 minutes, allowing the BK7 window to be removed from the piston. To create optically flat surfaces on both sides of the fabricated volume, a small amount of the liquid photopolymer is coated on the side opposite of the BK7 window and 25 millimeter diameter piece of cover glass is polymerized to it.

Selecting the materials that the piston and chamber are made of is essential for the platform and chamber to operate as designed. The piston was machined with stainless steel

and the chamber was bored out and anodized to increase its physical modulus and aide lubrication. Dissimilar metals were used to help prevent the binding of the materials. The piston and chamber were originally made of aluminum but were damaged beyond repair within 5 uses of the system.

2.5   Simulation of LDP

To gain a greater understanding of the inhibition and polymerization dynamics of the implementation of LDP that has been presented, a reaction/diffusion simulation similar to reference [102] was created. The simplified chemical model [91, 103] only considers the photolysis, chain initiation, chain propagation, chain termination, and oxygen inhibition processes.

Here I introduce a model of the photo-chemical processes and describe them with a set of reaction/diffusion equations suitable for numerical simulation of LDP. To initiate the photo-chemical processes, UV light incident on the sample photolyzes the initiator molecules (pi) to produce primary radical species (r') through a photo-cleavage process. The rate of radical production in a thin layer of material is proportional to the rate at which incident photons are absorbed in that layer. In a layer of thickness dz at a depth z, the rate of radical production, r' is given by

$$r' = 2\phi\epsilon[pi]\frac{\delta I(z)}{\delta z} \tag{2.6}$$

where $[pi]$, ϵ and ϕ are the concentration, molar absorptivity, and quantum yield of the photoinitiator respectively, and $I(z)$ is the light intensity. The light intensity varies through the depth of the material in accordance with Beer's law and is given by

$$\frac{\delta I(z)}{\delta z} = -\epsilon[pi]I(z) \tag{2.7}$$

The concentration of the photoinitiator is high in comparison to the number of absorbed photons such that the concentration does not significantly change during the exposure. Therefore, it can be assumed that the absorbance does not vary significantly with time,

and the rate of radical production, r', can be approximated by

$$r' = \phi\epsilon[PI]I_0 exp^{-\epsilon[PI]z} \tag{2.8}$$

The steady-state density of the photo-generated radicals is controlled by the termination processes. These can be either bi-molecular, wherein two radicals react with each other, or unimolecular, wherein a single radical reacts with an inhibiting species such as oxygen. The radical density of the material can be written as

$$\frac{\delta r'}{\delta t} = \phi\epsilon[PI]I(z)e^{-\epsilon[PI]z} - k_t[r']^2 - k_O[r'][O_2] \tag{2.9}$$

where k_t is the bimolecular termination rate constant and k_o is the unimolecular termination rate constant. The quasi-steady-state approximation [104] can then be used to estimate the concentration of radicals by equating radical production and consumption, making radical density constant throughout the simulation. The radical density within the layer is therefore

$$r' = \frac{k_o[O_2] + \sqrt{(k_o[O_2])^2 + 4\phi\epsilon[PI]I(z)e^{-\epsilon[PI]z}k_t}}{2k_t} \tag{2.10}$$

The diffusion of radical species are not considered in the model. Although both the initiator and radicals species are small, strong concentration gradients will not develop within the modeled layer because the thickness of the layer is nearly two orders of magnitude smaller than the absorption depth and diffusion rate is proportional to spatial scale squared.

The density of oxygen is controlled by the termination and diffusion processes. The diffusion of oxygen is included in the model because it is critical to the LDP process and the constant flux of oxygen from the PDMS layer creates strong concentration gradients that drive diffusion. Additionally, the size of molecular oxygen is small compared to the other chemical species modeled and thus its diffusivity is larger, potentially creating rapid changes in other reaction processes. The oxygen transport and consumption is described by

$$\frac{\delta[O_{2,\text{PEGDA}}]}{\delta t} = D_{o,\text{PEGDA}}\frac{\delta^2[O_{2,\text{PEGDA}}]}{\delta z^2} - k_o[r'][O_{2,\text{PEGDA}}] \tag{2.11}$$

where $D_{o,\text{PEGDA}}$ is the diffusion coefficient of oxygen in PEGDA and $[O_{2,\text{PEGDA}}]$ is the concentration of oxygen in PEGDA.

The density of monomer and polymer are controlled by the polymerization rate and radical density in the layer. Monomer is consumed when it reacts with a radical. The concentration of monomer is then given by

$$\frac{\delta[m]}{\delta t} = -k_p[m][r'] \tag{2.12}$$

where k_p is the polymerization rate constant and $[m]$ is the concentration of monomer. When a monomer molecule is consumed in the chain propagation step it is directly converted to polymer, so the production of polymer is equivalent to the monomer consumption. The concentration of polymer is then given by

$$\frac{\delta[p]}{\delta t} = k_p[m][r'] \tag{2.13}$$

The process of monomer diffusion is not included in the model because it should not effect the function of the chamber window. While the diffusion constant of monomer in the partially-converted PEGDA solution is unknown, a numerical study found that the results were not changed by monomer diffusion until the monomer diffusion coefficient was nearly equal to the oxygen diffusion coefficient. Since this is unreasonable given the ratio of their molecular weights, I conclude that monomer diffusion can safely be ignored.

2.5.1 Non-dimensional equations

If the reaction and diffusion coefficients of the material system are known, monomer and oxygen concentration for a given time interval can be accurately simulated. However, there is little insight into the relationship between the key parameters and variables in the material system. Non-dimensional analysis, on the other hand, can provide such insights into the reaction/diffusion dynamics. The parameters and variables of the oxygen transport and consumption equation were properly scaled to create non-dimensional equations using

the following relationships

$$t' = \frac{tD_o}{L^2}, \quad z' = \frac{z}{L}, \quad D_{a1} = \frac{k_o^2[O_{2,\text{eqib}}]L^2}{2k_tD_o}, \quad D_{a2} = \frac{k_pk_o[O_{2,\text{eqib}}]L^2}{2k_tD_o},$$

where $[O_{2,\text{eqib}}]$ is the equilibrium concentration of oxygen and L is represents the spatial extent of the simulation. Time is normalized to the diffusion time of oxygen across the spatial extent on the simulation. Space is normalized to the thickness of the exposure geometry. D_{a1} is a dimensionless number that quantifies the ratio of the rate of oxygen inhibition to the diffusion of oxygen into the monomer. D_{a2} is a dimensionless number that quantifies the ratio of the rate of radical propagation to the diffusion of oxygen into the monomer. The concentration of the chemical components were normalized to their initial concentrations using the following relationships

$$\theta = \frac{[O_2]}{[O_{2,\text{eqib}}]}, \quad [M] = \frac{[m]}{[m_0]},$$

where m_0 is the initial concentration of monomer and $[M]$ is the normalized concentration of monomer. The equation for oxygen transport and consumption becomes the following

$$\frac{\delta\theta}{\delta t'} = \frac{\delta^2\theta}{\delta z'^2} - D_{a1}\theta(-\theta + \sqrt{\theta^2 + \frac{4\phi\epsilon[PI]I_0k_t}{k_o^2[O_{2,\text{eqib}}]^2}e^{-\epsilon[PI]Lz'}}) \tag{2.14}$$

The non-dimensional equation for monomer consumption becomes the following

$$\frac{\delta[M]}{\delta t'} = D_{a2}[M](\theta - \sqrt{\theta^2 + \frac{4\phi\epsilon[PI]I_0k_t}{k_o^2[O_{2,\text{eqib}}]^2}e^{-\epsilon[PI]Lz'}}) \tag{2.15}$$

2.5.2   Initial and boundary conditions

There are two external boundaries in the simulation, one at the edge of the PDMS/PEGDA interface and the other at the liquid photopolymer/platform interface. Since the diffusivity of oxygen in PDMS is orders of magnitude greater than the diffusivity of oxygen in PEGDA [105], it is assumed that the oxygen concentration maintains it atmospheric concentration at the interface between the PDMS and PEGDA. So the PDMS/PEGDA interface boundary condition is

$$[\theta](0, t') = 1 \tag{2.16}$$

The liquid photopolymer/platform interface is a hard boundary, so a Neumann boundary condition is imposed. A Neumann boundary condition defines the flux across the boundary to be zero. The liquid photopolymer/platform boundary condition is

$$\frac{\delta[\theta]}{\delta z'} = 0 \tag{2.17}$$

The initial conditions for chemicals concentrations in PEGDA are

$$
\begin{aligned}
[\theta](z, 0) &= 1 \\
[M](z, 0) &= 1 \\
[P](z, 0) &= 0
\end{aligned}
$$

$$\tag{2.18}$$

2.5.3   Model parameters

.

Polyethylene (glycol) diacrylate (PEGDA), molecular weight 575 Daltons, was used as the model material system to understand chamber window behavior. PEGDA was used for all the initial and proof of concept experiments, however, the material was later changed to a multi-component material system to create high contrast refractive index structures. I will present results from PEGDA because all of the rates and constants are known in the literature. Typical values of rates and constants for PEGDA and the photoinitiator, Irgacure 651, are shown in Table 2.5.3.

2.5.4   1D simulation results

The differential equations were integrated in time to find the depth dependence of all the chemical species. The intensity of polymerizing light was held constant throughout the depth of the layer, as shown in Figure 2.13(a). The results of the simulation are shown below in Figure 2.13(b).

Table 2.2: Reaction rates and diffusion constants used in the reaction/diffusion simulation

Parameter	Value	Units	Source
k_p	25	$\frac{m^3}{(mols)}$	[106]
k_t	2520	$\frac{m^3}{(mols)}$	[106]
k_o	5 x 10^5	$\frac{m^3}{(mols)}$	[91]
D_o	28.4	$\frac{\mu m^2}{(s)}$	[105]
ϵ	40	$\frac{m^3}{(mols)}$	[107]
$[O_{2,eqib}]$	1.5	$\frac{(mol)}{m^3}$	[108]
ϕ	.6	—	[109]
I_0	4 x 10^{-3}	$\frac{E}{m^2 s}$	-

The simulation results shown in Figure 2.13(b) demonstrate the fundamental performance of the window, that diffusion of oxygen from the PDMS maintains an inhibited, liquid layer directly adjacent the PDMS layer. The concentration of oxygen diffusing from the PDMS must drop approximately two orders of magnitude before monomer can successfully compete with oxygen for radicals and begin to polymerize. This inhibits conversion in a one-micron layer, preventing polymer adhesion to the window and stiction between layers. The oxygen-inhibited layer also provides a high-concentration monomer source for subsequent diffusional mass transport of unreacted monomer into the exposed layer required to develop index structures.

The reaction/diffusion dynamics of the system also result in a 50 nm thick transition between the inhibited and high conversion regions. If the thickness of the inhibited region can be well controlled, layers thicknesses under 100 nm can be sequentially layered. Additionally, this 50 nm transition region has a gradient of monomer conversion from zero through high conversion, so it is reasonable to assume it aides polymerization and adhesion between subsequent fabricated layers.
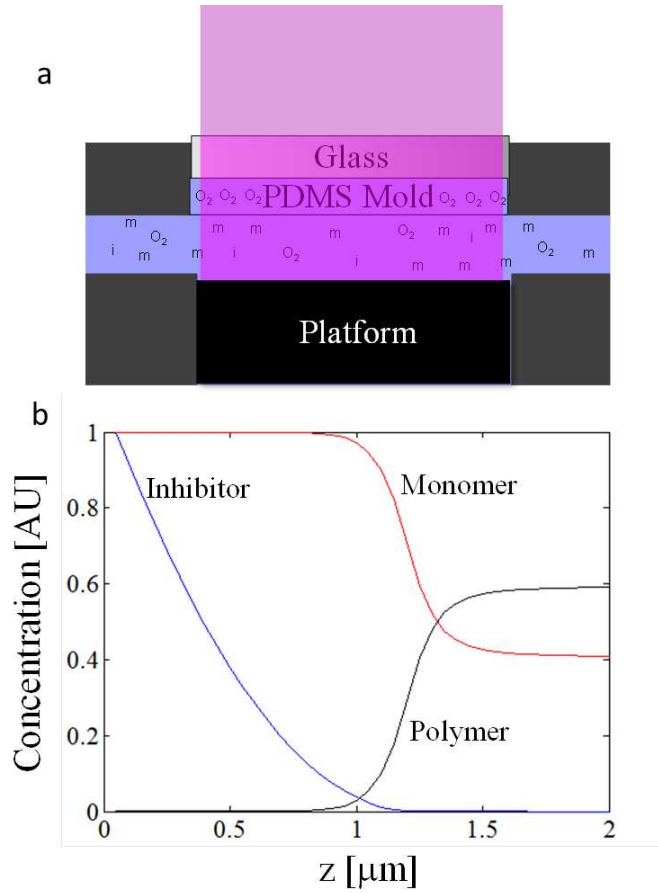
Figure 2.13: Reaction/Diffusion simulations of LDP. (a) representation of the intensity used in the simulation. (b) The concentration of oxygen, monomer, and polymer immediately after completion of exposure.

2.5.5   2D simulation results

To understand how the presence of oxygen effects the concentrations of monomer and oxygen in the transverse dimension, the numerical technique described in the previous section was extended to two spatial dimensions, one in depth and one transverse to the window. The intensity pattern used in the simulation is shown in Figure 2.14. The monomer and oxygen distribution were time-advanced via a simple $2 + 1$D forward difference scheme. The physical parameters used in the simulation were the same as the $1 + 1$D simulation and can be found in table 2.5.3. The results of the simulation are shown in Figure 2.15.
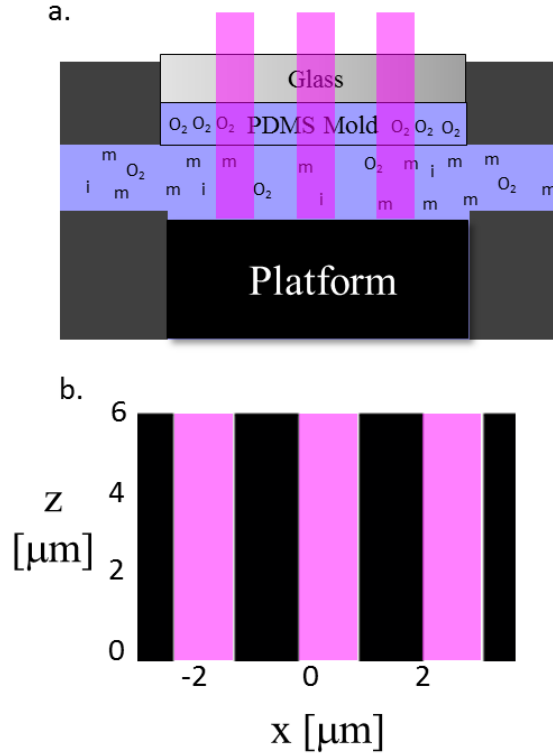
Figure 2.14: 2D intensity pattern used for the 2+1D Reaction/Diffusion simulation of LDP. (a) Representation of the intensity in the simulation where m represents monomer, i represents photoinitiator and O_2 represents oxygen. (b) Spatial dimensions of the 2D intensity pattern.

The simulation results shown in Figure 2.15 demonstrate that oxygen performs two functions: it diffuses from the PDMS to maintain an inhibited region directly adjacent to the PDMS and it narrows transverse polymer feature size. On the edges of the illumination pattern, the oxygen has not been consumed and there is an inhibited region at the edge of the illuminated area, which narrows the polymerized feature. In the center of the exposed region all the oxygen has been consumed, so polymerization is not spatially inhibited and the polymerized features are copies of the illumination pattern. The depletion of oxygen in the dark regions is due to oxygen diffusing from the dark regions to the illuminated regions where it is immediately consumed. This demonstrates decreased feature size requires a
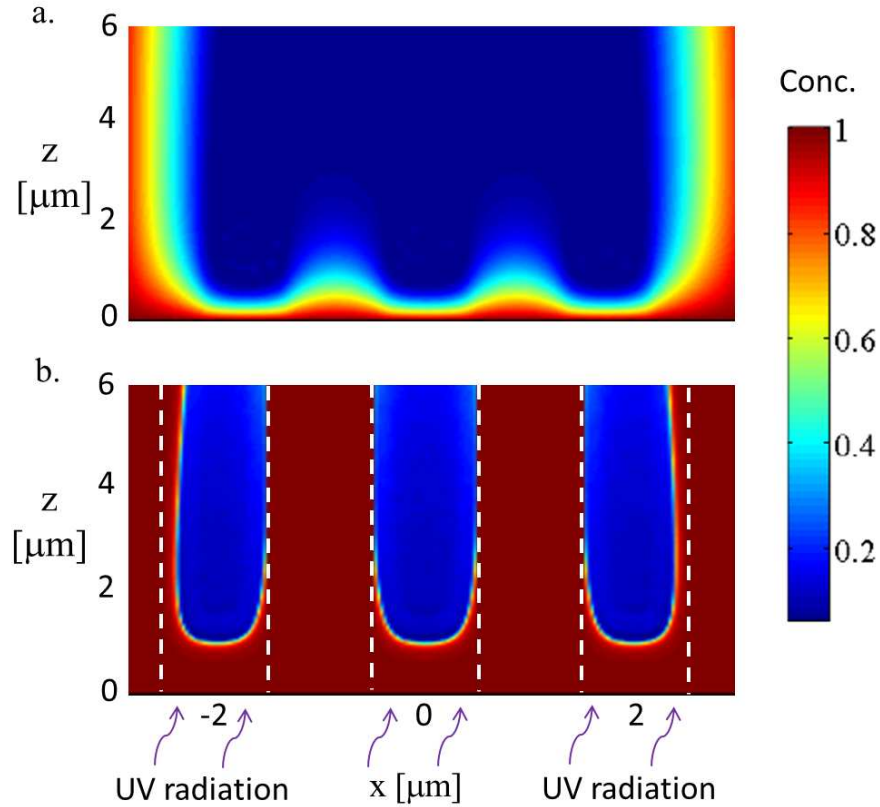
Figure 2.15: 2D Reaction/Diffusion simulation of LDP. (a) The concentration of inhibitor immediately after completion of exposure. (b) The concentration of monomer immediately after completion of exposure. The concentration of polymer is the inverse of the monomer concentration.

concentration gradient of oxygen at the edge of the illuminated region to inhibit conversion. A large supply of oxygen around the illuminated region is needed to create the concentration gradient necessary for improved resolution. This effect is seen experimentally in the LDP process by a narrowing of the exposed waveguide diameters in the sparse waveguide array shown later in this chapter.

2.6   The fabrication and characterization of index structures in a volume

With this process I demonstrate various fabricated volumes with multiple layers containing 3D index structures. In order to determine the fidelity and index contrast of the

index structures I have fabricated through the volume, various characterization methods have been used to determine the refractive index distribution.

2.6.1 Characterization methods for fabricated structures

In order to characterize the fabricated structures and maximize index contrast, measurements of the refractive index distribution of the fabricated volume is required. Several methods, such as phase microscopy, interferometry, optical diffraction tomography [110], and scanning surface reflectivity [111] have been developed to measure refractive index structures. These methods either collect the transmitted, scattered, or reflected optical field to measure the refractive index either of the surface of a volume, the strength of a known periodic structure, or the projection of the refractive index distribution in depth onto a 2D plane.

Interferometry is widely used to characterize thin phase objects with small refractive index changes. However, LDP fabricates thick volumes containing strong index features, so interferometry is not an appropriate imaging modality. Phase contrast microscopy, such as DIC microscopy [112], is usually limited to producing a qualitative image of the refractive index distribution of the volume that has been integrated through the depth of field. While this is a useful for determining the shape and relative strength of the refractive index structures, it is difficult to make conclusions from the images it produces. Quantitative implementations of DIC microscopy have been demonstrated, but are limited to thin objects [113], making the technique unfit for quantitatively measuring the thick volumes produced by LDP.

In order to obtain a quantitative measure of the refractive index distribution, a scanning optical microscope that scans surface reflectivity and uses confocal filtering to improve resolution [114, 115], was developed by Keith Kamysiak of the McLeod research group. This method measures refractive index of gradient index structures at the surface of a volume. The surface creates a sharp boundary and thus allows reflection imaging of slowly-varying index structures. The gradient index structures fabricated in depth do not have a sharp

boundary and do not contain spatial frequencies in the reflection band of a microscope and therefore, cannot be resolved. To characterize the fabricated structures, DIC microscopy is used in conjunction with the scanning optical microscope to obtain both qualitative and quantitative information about the fabricated structures.

2.6.1.1   Scanning optical microscope

The DIC microscope produces qualitative information, but lacks the ability to provide quantitative information. However, in order to determine the maximum index contrast and design optical devices, quantitative information about the refractive index distribution is required. Therefore, a scanning optical microscope is used that determines the refractive index distribution of a volume's surface by measuring the reflectivity across the surface. A high NA lens used in conjunction with oversampling of the volume and additional data processing, produces a highly resolved refractive index map of the surface of the volume. The optical setup of the scanning optical microscope is shown below in Figure 2.16.
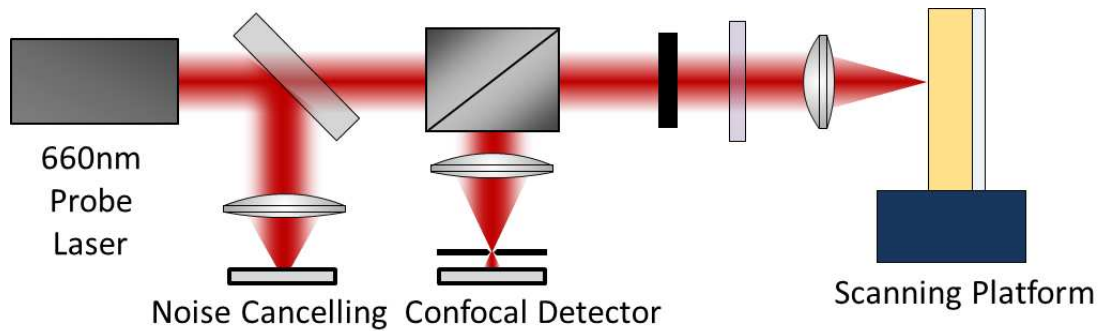
Figure 2.16: Optical setup of the scanning optical microscope used to quantitatively characterize refractive index structures at the surface of a volume fabricated by LDP.

Laser instability and noise in the detection system can significantly reduce the accuracy and precision of microscopes that quantify the refractive index distribution through reflection [116]. In order to reduce these effects in the scanning optical microscope used here, a noise canceling detector and confocal filter were implemented within the optical sys-

tem. The confocal filter and noise canceling detector enable precision of the refractive index distribution on the order of 10^{-4}.

An issue with using the scanning optical microscope, however, is the amount of time required to produce a refractive index map of the surface. The scanning optical microscope must raster through 4 x 10^6, 50 nm^2 voxels with a 50μm/s transverse scan speed in order to produce the 2D image. Additionally, the volume to be measured must be made perpendicular to the scanning laser, where less than 0.1 mrad of angular deviation of the surface to the laser is required for areas measuring one mm^2. Therefore, an hour long, iterative alignment procedure is required before each measurement to adjust the tip and tilt of the part, further increasing the time to produce an image.

2.6.2   Thin fabrications

With this process I demonstrate fabricated volumes with multiple layers containing 3D index structures. To illustrate the process of high resolution 3D index structuring within a large volume, a one μm thick index pattern is sandwiched between two unpatterned layers each 2 mm thick, as shown in Figure 2.17. Figure 2.17 illustrates LDP's ability to fabricate 3D index structures deep within a volume and its ability to fabricate large volume polymer structures.

LDP is also capable of fabricating programmable refractive index patterns in independent layers with sub-μm transverse resolution within each layer. Figure 2.18(a) shows a DIC micrograph of a one-μm thick University of Colorado (CU) buffalo pattern, followed by a one-micron CU seal pattern, demonstrating multiple patterned layers. The large transverse structures shown here would take months to develop without longitudinal diffusion and would extend through the entire depth of the volume. The one-μm layer thickness enables longitudinal diffusion and creates a short diffusion path, so development time is minutes instead of months. Additionally, the index structure is limited to the extent of the layer, so complex 3D index patterns can be fabricated. Figure 2.18(b) shows a one-μm pitch hologram,
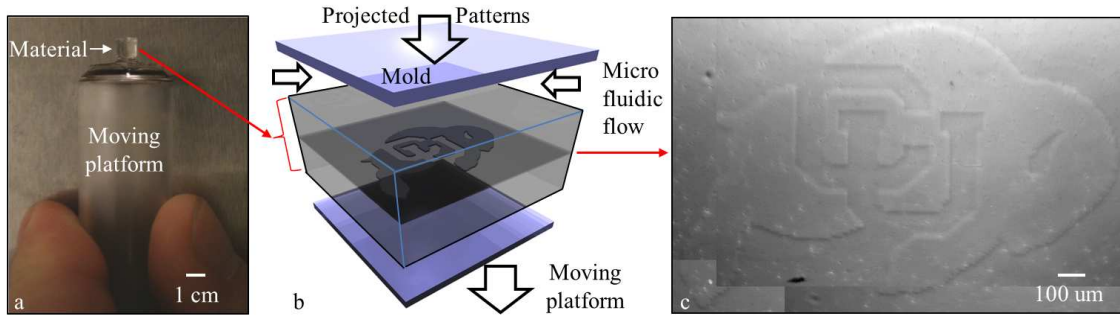
Figure 2.17: Layout of device fabrication using the LDP instrument. (a) Photo of part printed in LDP. (b) Deposition chamber layout where a 2D mask has been projected onto a single thin layer which has been encapsulated by additional non-patterned layers. (c) DIC micrograph of part shown in (b). The exposure conditions are described in Appendix B.

corresponding to 500 nm line widths, written using two beam interference, demonstrating both analog response and sub-μm transverse resolution. Figure 2.18(c) demonstrates the flexibility of LDP via the fabrication of a photonic crystal fiber structure.

2.6.3   Waveguide array fabrication

To demonstrate LDP's ability to manufacture photonic devices, a one-mm-thick rectangular waveguide array containing over 3,000 waveguide arrays was fabricated. To fabricate the one-mm-thick rectangular waveguide array, 100 layers measuring 12 μm thick were sequentially patterned with a 2D cross-section of a waveguide array, as shown in Figure 2.19(a). The fabricated waveguide array was tested by illuminating the front facet with a plane wave and imaging the end facet onto a CMOS camera, shown in Figure 2.19(b). The dark regions adjacent to the guided outputs are the result of the plane wave projecting onto the propagating modes of the waveguide at the input facet of the device. The coherent plane wave scatters off dust particles and imperfections in the cover glass, producing the background noise shown in the image, common for coherent imaging systems.

The index contrast of the waveguide array, measured by the scanning optical microscope, was measured to be 0.1, as shown in Figure 2.19(c). This index contrast is 100 times
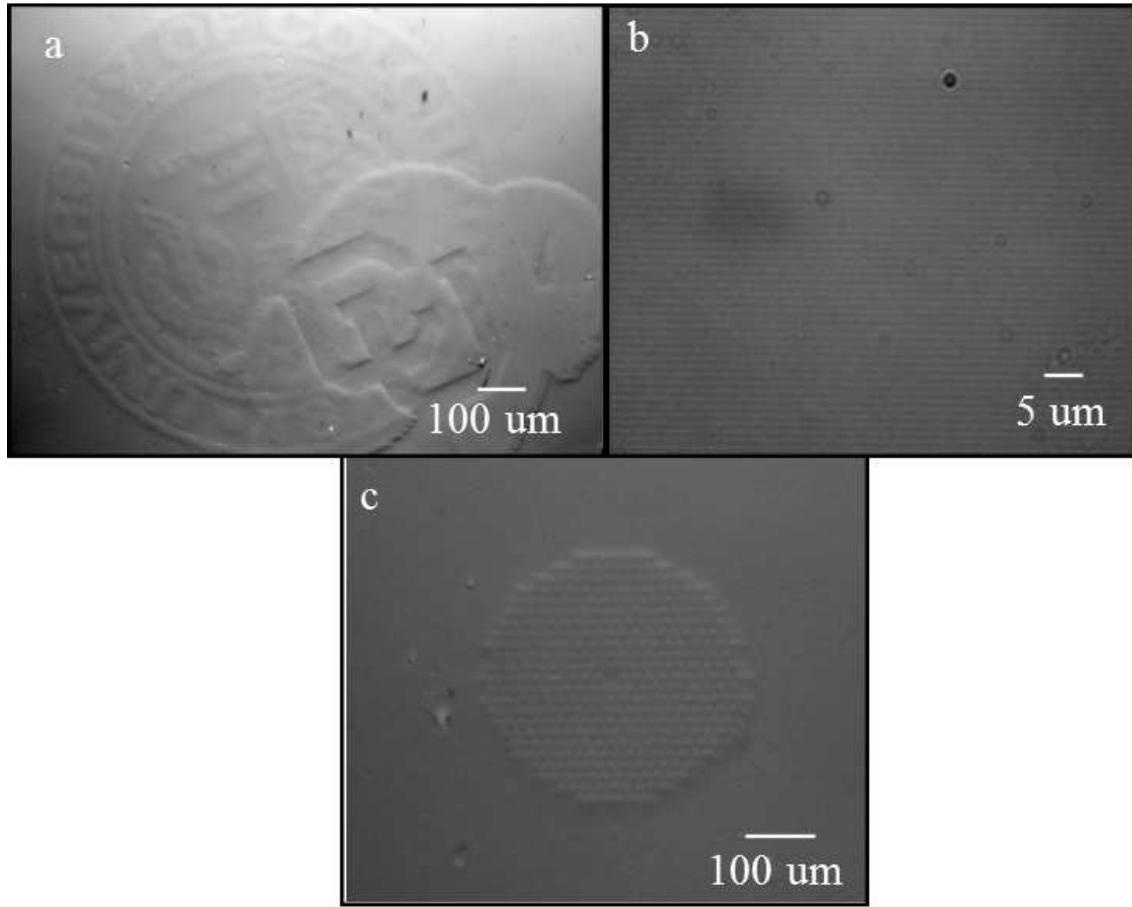
Figure 2.18: DIC micrograph images of single layer index structures written with LDP.(a) Two sequentially written 3μm layers of the buffalo, written first, and the CU seal, written second. (b) 1μm pitch hologram, corresponding to 500 nm line widths. (c) Photonic crystal fiber written in a 3 μm layer demonstrating LDP's programmability.

larger than femtosecond micromachining and 20 times larger than commercial holographic photopolymers, allowing greater flexibility in photonic device fabrication. The index contrast shown is 25 times larger than expected from bulk measurements, shown in Chapter 3, and is verified by comparing a numerical an experimental data at the output of the waveguide array, shown in section 2.6.4. The fabrication rate for the completion of the waveguide array shown in Figure 2.19, was 1.2 hours per mm^3, which is 10^5 faster than femtosecond micromachining, see appendix A for the calculation.
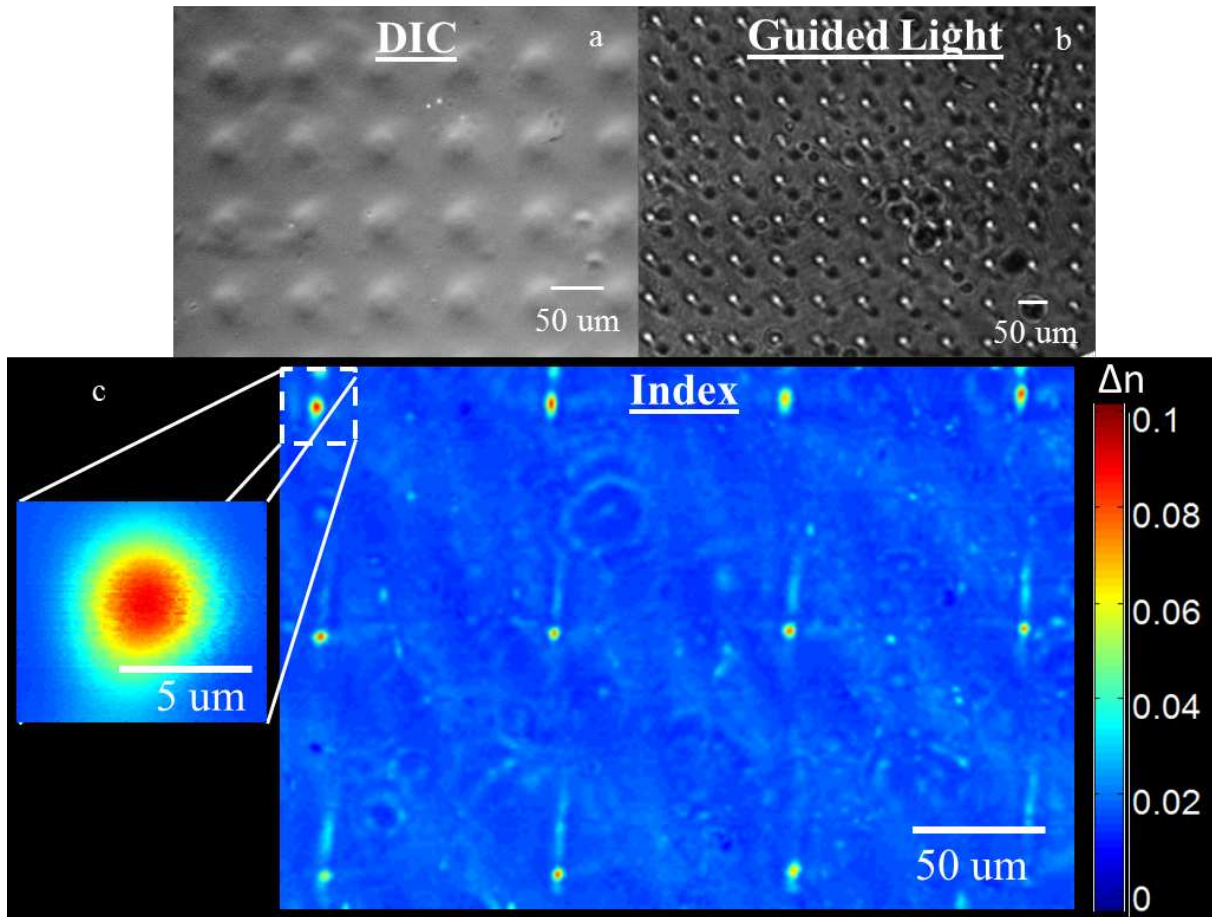
Figure 2.19: (a) DIC micrograph of a 80 m pitch rectangular waveguide array pattern written in a single 10 μm layer. (b) Image of the end facet of 80 μm pitch rectangular waveguide array, fabricated by sequentially-writing 100, 10 μm thick layers, where the front facet was illuminated with a plane wave at 633 nm. (c) Refractive index map of the end facet of the rectangular waveguide array shown in (a-b).

The difference in the imaged structure shown by the DIC image(Figure 2.19(a)), plane-wave illuminated image(Figure 2.19(b)), and index map(Figure 2.19(c)), is the result of using different imaging modalities, each measuring different quantities. The DIC microscope, used to produce Figure 2.19(a), is a qualitative measurement technique that produces an image nonlinearly related to the transverse gradient of the phase. The confocal scanning microscope, however, produces a quantitative map of the refractive index distribution by measuring the reflected light at of a large number of positions on the surface of the structure. The additional structure in the index map is dust particles and imperfections in the glass, imaged due to the high sensitivity of the confocal scanning microscope.

The waveguides have a gradient refractive index profile with a full width half max (FWHM) of approximately 3 μm, even though a binary pattern of 12 μm was used to expose each layer. This is most likely the result of molecular oxygen diffusing transversely within the layer, completely inhibiting polymerization at the edge of the light pattern and narrowing the gradient of the index profile. A reduction in the extent of the spatial profile of binary feature is also demonstrated by the numerical simulation, see Figure 2.15, which shows that oxygen diffuses transversely in the layer and inhibits polymerization at the edge of the light pattern.

2.6.4   Characterizing the waveguides

The index contrast of .1 measured by the scanning optical microscope is well beyond expected index change(see section 3.5.3), so the guiding properties of the waveguide were investigated to confirm the large index change. The modal spectrum of the output of a waveguide is numerical calculated by a modal propagation simulation and experientially determined by a mode characterization tool. In order to numerically calculate the expected output of the waveguide, the number of bound modes of the waveguide must be determined. To determine the number of bound modes in the waveguide the NA and normalized frequency of The numerical aperture acceptance angle for a gradient index waveguide [117] is defined

as

$$NA = \sqrt{\frac{N_{core}^2 - N_{clad}^2}{N_{core}^2}} = sin(\frac{\theta_a}{2}) \tag{2.19}$$

where n_{core} is the maximum index at the center of the core, n_{clad} is the refractive index of the cladding, and θ_a corresponds to the acceptance angle of the waveguide. The numerical aperture of a waveguide in the fabricated waveguide array is 0.335, corresponding to an acceptance angle of approximately 40 degrees. The normalized frequency, or V-number, of the waveguides can then be determined, where V-number is defined as

$$V = 2\pi \frac{a}{\lambda_0} NA \tag{2.20}$$

where a is the radius of the waveguide and λ_0 is the wavelength of light in vacuum. The V number at 660 nm, the probe wavelength used in the next section, is 9.45. The approximate modal volume for the waveguide, assuming a quadratic index profile, is defined as

$$M = \frac{V^2}{4} \tag{2.21}$$

and the number of bound modes, M, in a waveguide within the array is 22. To determine the modal spectrum in the waveguide, a finite difference mode solver for dielectric waveguides [118] was used. The numerical mode solver determines the bound modes of both orthogonal polarizations and each bound modes effective index as well as the spatial intensity profile for each mode. The normalized electric field for the bound modes polarized in the x-direction is shown in Figure 2.20. Since the waveguide is symmetric, the bound modes polarized in the orthogonal direction will have approximately the same intensity profiles and effective indices.

The modal spectrum of the waveguide enables the implementation of a modal propagation simulation to investigate the properties of the waveguide. The modal propagation method [119] represents the electromagnetic fields in terms of the bound modes which propagate without loss along the waveguide and radiation modes which carry power away from the waveguide. To determine the output of the waveguide, the incident field used in the
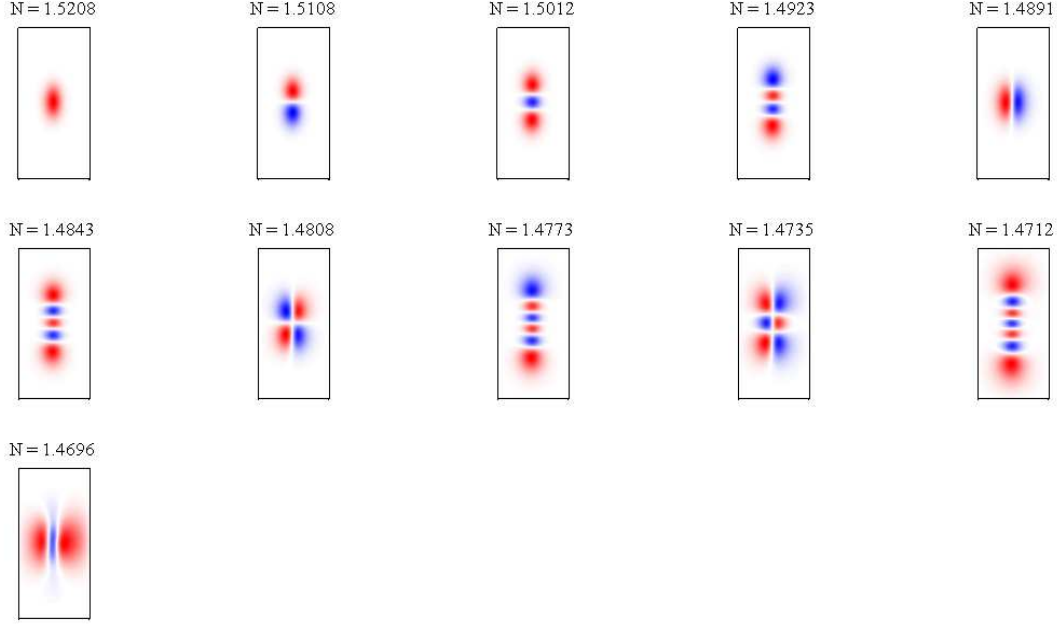
Figure 2.20: The bound modes of a singular waveguide where the electric field is polarized in the x-direction. The effective index of each mode is shown above the mode profile. The red represents positive polarity and the blue represents negative polarity.

mode characterization tool, described later in the section, is projected onto the 22 bound modes of the waveguide. The excited bound modes are propagated down the volume and then interfered at the output of the waveguide. The incident electric field and the amplitudes of the bound modes excited by the incident field are shown in Figure 2.21.

Figure 2.21(b) shows that when the incident beam is aligned with the waveguide approximately 90% of the incident field is projected onto the first order mode. The electric field after the excited modal spectrum has propagated the length of the waveguide is shown in Figure 2.22.

Figure 2.22 shows that after the coupled field propagates through the volume the electric field is no longer symmetrical. The loss in symmetry at the output is most likely due to the slight asymmetry of the waveguides in the array. To determine if the output electric field became more symmetrical than Figure 2.22(b), the incident electric field was
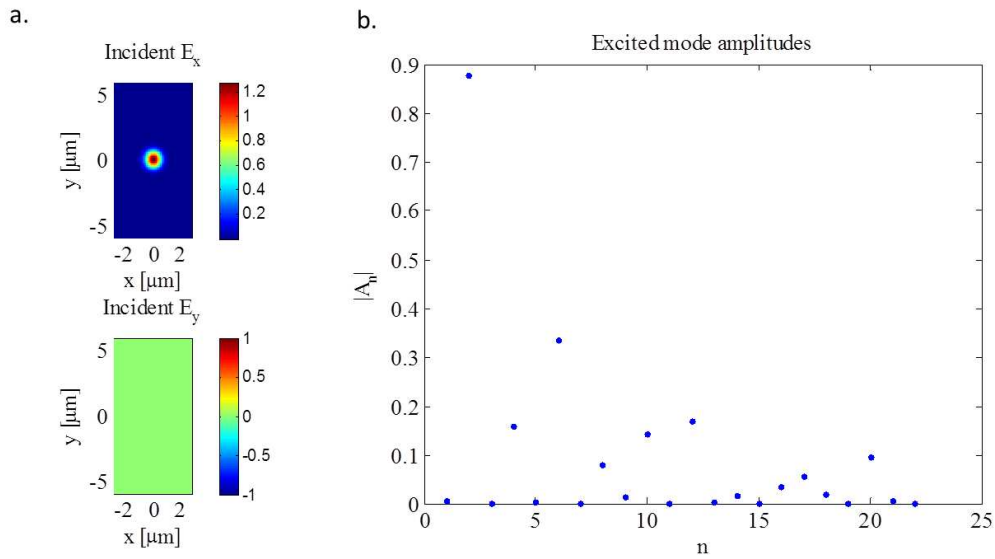
Figure 2.21: (a) The incident electric field used to couple onto the modal spectrum. (b) The amplitudes of the bound modes excited by the incident electric field.
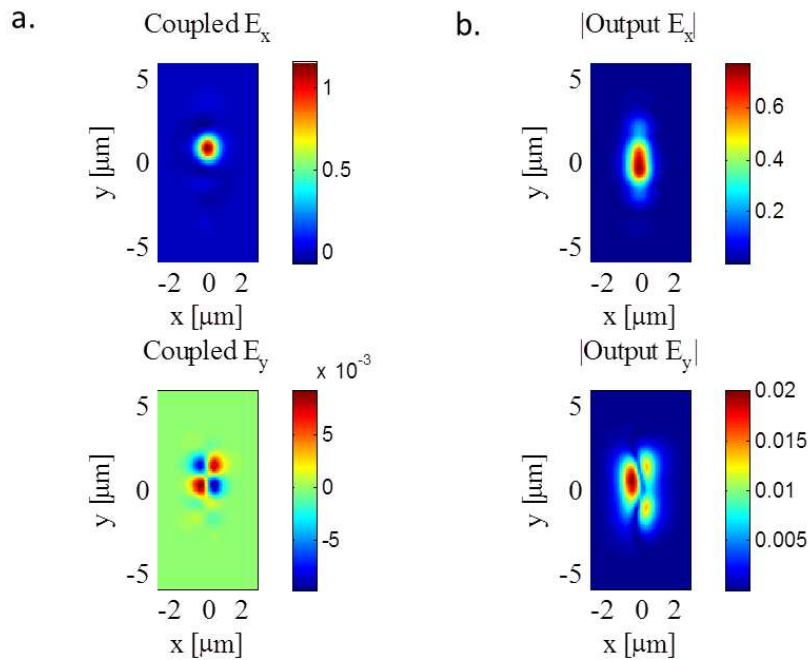
Figure 2.22: (a) The electric field immediately after the incident electric field has been projected onto the model spectrum of the waveguide (b) the electric field at the output of the waveguide.

translated about the waveguide in the simulation. The electric field at the output of the waveguide when the incident electric field is translated 500 nm vertically is shown in Figure 2.23. Figure 2.23 demonstrates that a slight offset of the incident field results in an output that has a 97.3% correlation to the measured intensity profile shown in Figure 2.22.
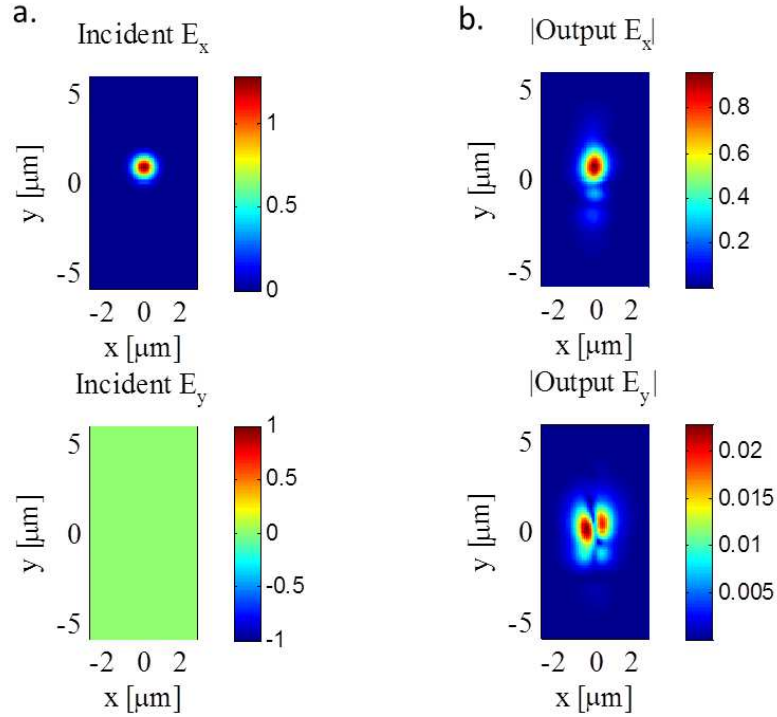
Figure 2.23: (a) The incident electric field used to couple onto the modal spectrum. The incident beam has been translated by 500 nm. (b) The electric field at the output of the waveguide.

In order to experimentally characterize a waveguide within the fabricated array and compare with the modal propagation simulation, a waveguide characterization tool is used to probe waveguides within the array [120]. The optical setup of the waveguide characterization tool, as shown in Figure 2.24, employs a reflection geometry where the modal spectrum is excited and collected by the same lens. The fabricated waveguide array is adhered to a front-surface metal mirror in order to be tested with this system. A reflection geometry, such as this, provides two advantages over a more conventional transmission system. First,

the propagation length is doubled, providing further separation of the guided from the radiation modes. Secondly, the waveguide only needs to be aligned to a single lens, improving measurement repeatability and reducing the alignment time required for every measurement.
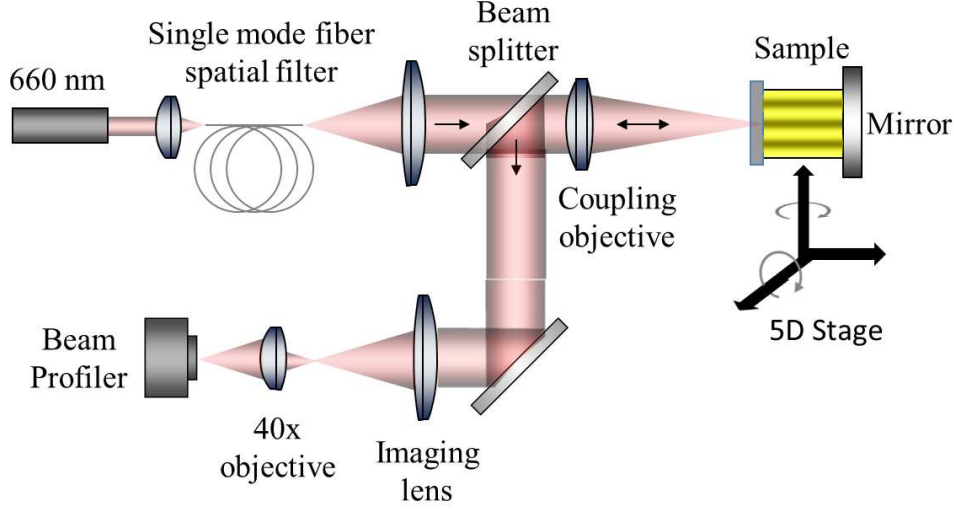
Figure 2.24: Optical setup of the waveguide characterization tool utilized to probe single waveguides of the waveguide array. The focal length of the coupling objective is 20 mm, the focal length of the imaging lens is 25 mm, and the 40x objective lens is used to further magnify the intensity profile.

In the optical setup, the incident laser is focused to a 2.6 μm $1/e^2$ diameter using an objective and then aligned to the front facet of the fabricated waveguide array using the 5D stage. The incident laser beam is then coupled into the modal spectrum of the waveguide, the excited bound modes will propagate through the waveguide, reflect at the mirror, and then propagate back through the waveguide. The propagating modes then exit the waveguide and are captured by the same coupling objective, where the imaging system magnifies the image of the propagating modal spectrum. The magnified image of the guided mode is captured by a commercial beam profiler, WinCamD-UCD12 from DataRay Inc. The coupling efficiency of the incident laser beam into the guided mode is then optimized by maximizing the power returned through the confocal filter, rejecting radiation modes and out-of-focus reflections.

The image of the transmission of a single waveguide, after coupling was maximized, is shown in Figure 2.24.
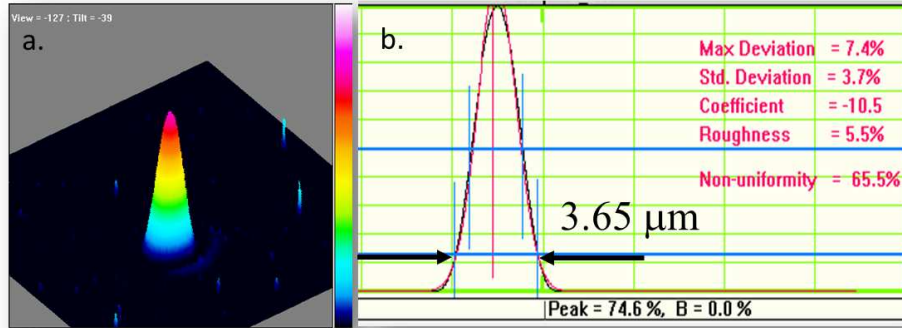
Figure 2.25: The intensity profile measured by the mode characterization tool. (a) Two dimensional intensity profile of the measured transmission. (b) Cross section of profile shown in (a).

The coupling efficiency of the output of the waveguide to the first order mode is 95.8%. In addition to finding the spatial dimensions of the transmitted field when there is maximum coupling, the sample was translated around the waveguide to determine if the waveguide demonstrated single mode behavior. If the fabricated waveguide only supported a single bound mode, the coupling efficiency would match the dimensions of the Gaussian probe beam. However, the coupling efficiency was not consistent with single mode behavior and did not resemble a Gaussian shape. This measured output profile allows a direct comparison between expected behavior given the index profile predicted by the modal propagation simulation and the measured behavior, as shown in Figure 2.26.

Figure 2.26 demonstrates the waveguide behavior observed with the mode characterization tool agrees with the predicted waveguide behavior shown by the modal propagation simulation. These results confirm the index profile measured by the scanning optical microscope is relatively consistent through the depth of the volume and the measured index contrast is not an inhomogeneity at the surface of the volume.
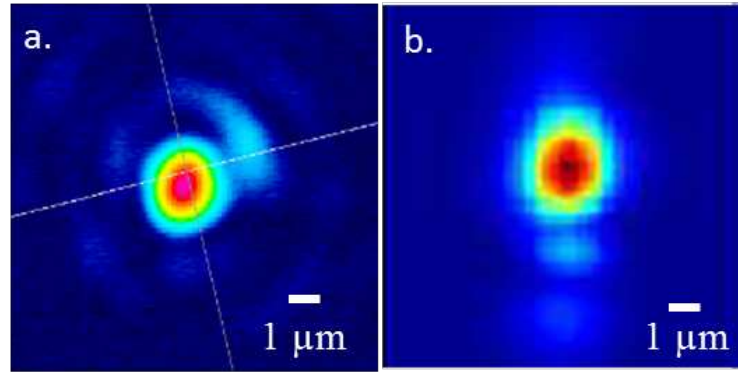
Figure 2.26: Comparison of the intensity profile of the output of a waveguide measured by the mode characterization tool and a modal propagation simulation. (a) Intensity profile measured by the mode characterization tool. (b) Intensity profile calculated by a modal propagation simulation.

2.7   Fabrication of physical structures

With this process, a fabricated volume with multiple layers containing 3D physical structures is demonstrated. The process steps for physical structure fabrication differ from index structure fabrication. To begin the process, liquid monomer is drawn through a microfluidic gap between the chamber window and platform created as the platform is lowered. This produces a thin layer of liquid monomer between the chamber window and platform, with the layer thickness fixed by the distance the moving platform is lowered. In step (b), the new liquid layer is patterned by two dimensional (2D) projection lithography created by optical projection of a chrome-on-glass mask, polymerizing the liquid monomer into a solidified gel of the projected 2D pattern. Polymerization is suppressed just below the chamber window via inhibitor diffusion from the PDMS enabling repetitive layering. The diffusion and post-cure steps for index structure fabrication, as shown in Figure 2.1, are not required for the fabrication of physical structures. This liquid injection and exposure process, steps a-c, is repeated until the 3D physical part is completed.

To illustrate the process of three dimensional physical structuring within a large vol-
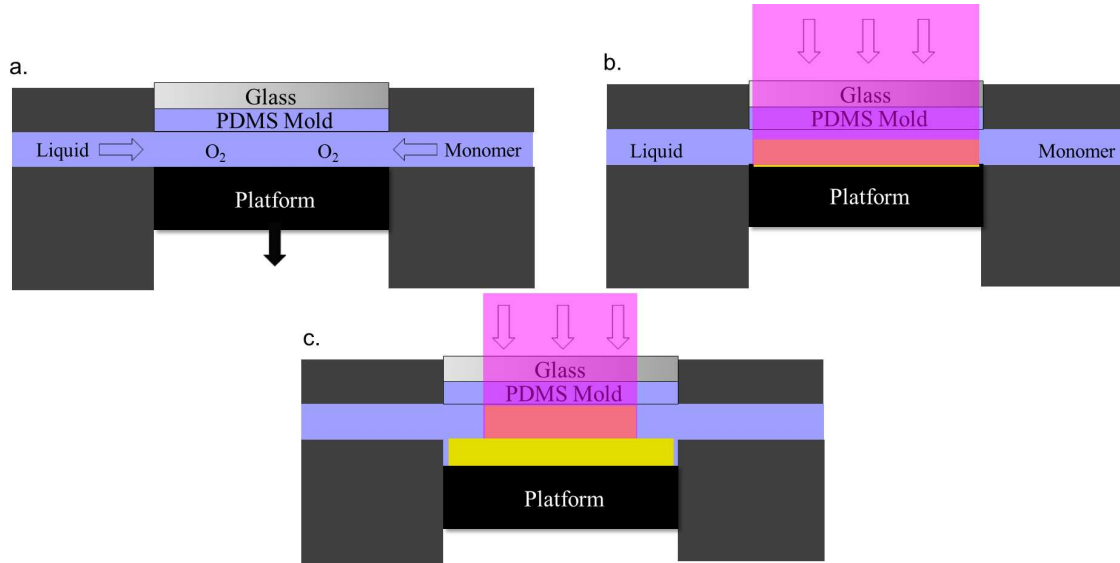
Figure 2.27: Process steps for physical structure fabrication using LDP. (a) UV sensitive liquid monomer is drawn through a microfluidic gap created as the platform is lowered, producing a new layer. (b) The new liquid layer is patterned by 2D projection lithography, using 365 nm light, polymerizing the liquid monomer into a gel of the 2D pattern. (c) A new layer of UV sensitive liquid monomer is injected on top of the first gelled layer and another 2D pattern is projected onto the layer, polymerizing a new gelled 2D pattern polymerized which is adhered to the first pattern. This liquid injection and exposure process is repeated until the 3D physical part is completed.

ume, four 10 μm thick circular layers with decreasing diameters were stacked on top of each other, shown in Figure 2.28. This simple structure was chosen because it demonstrated LDP's ability to fabricate physical structures, while simultaneously avoiding the complications in processing that structures with small resolution or complex geometires, such as a overhanging features, require for fabrication. Fabricating structures with micron vertical resolution by simply making thinner layers is not sufficient to control the vertical resolution of the object. If the light is not confined to only the new layer, it will penetrate deep within the lithographic chamber and result in unintended polymerizations in the fabricated layers of the object, resulting in a loss of fidelity for the structures.

The control of both the light penetration in the material and polymerization depth are the parameters of importance for the improvement of the vertical resolution when fab-
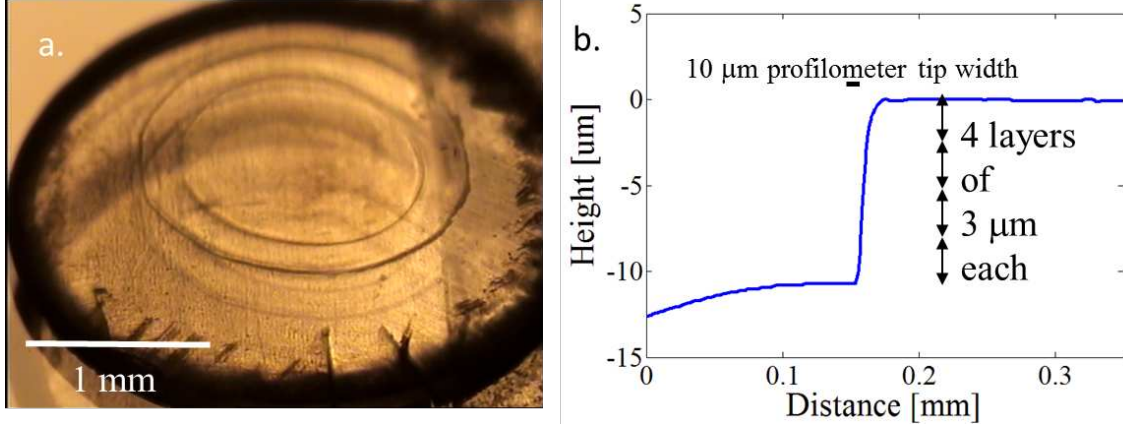
Figure 2.28: Physical structuring results. (a) Image of physical structure fabricated using LDP. (b) Results from profilometer demonstrating depth resolution.

ricating physical 3D objects. The stereolithographic process has the same light penetration and polymerization depth issue [121], and has shown improved vertical resolution by either irradiating the material close to the polymerization threshold, using a highly absorptive material or adding a neutral absorber. These additional processing steps could be implemented within LDP or a different solution, and will be discussed further in the future work section of the thesis.

Even with the current vertical and transverse resolution limits in physical structuring, Figure 2.28 demonstrates LDP's ability to fabricate physical and index structures with high throughput, using a single instrument. This enables efficient fabrication of devices containing both physical and index structures, giving greater flexibility and function to photonic devices.

2.8   Conclusions

In summary, the LDP process enables efficient production of index structures with nearly arbitrary index feature size and shape not limited by out of focus exposure or transverse diffusional distances. The 3D volume containing the arbitrary index features is created through repetitive layering of a liquid diffusive photopolymer, where each layer is structured

by projection lithography. The enabling technology of the process is the chamber window, which planarizes each new liquid layer, allows optical pattern access to the material, prevents polymer adhesion to the optical window and maintains a monomer-rich liquid layer next to the exposed volume, enabling longitudinal monomer diffusion. Longitudinal monomer diffusion makes total fabrication time independent of transverse feature scale and density, and gives the process the unique property that increased axial resolution decreases the fabrication time, enabling rapid fabrication of high resolution devices and structures. In addition to rapid longitudinal monomer diffusion, fabrication time is minimized by the processing of the entire volume on a single instrument, eliminating time intensive processes, such as spin coating, pre and post bakes, planaraization and solvent washing. Both these attributes enable fabrications of 3D volumes five orders of magnitude faster than femtosecond micromachining.

The fabricated 3D index structures have an index contrast up to 0.1, 100 times larger than femtosecond micromachining, allowing greater flexibility in design of 3D refractive index devices. The large index contrast and fast fabrication rate of LDP potentially enable the fabrication of large scale, arbitrary 3D refractive index devices, such as, photonic crystal waveguides [122], diffractive elements and 3D integrated photonic devices. The next chapter describes how the diffusive photopolymer was designed to provide high index contrast and rapid diffusion.

Chapter 3

Liquid Photopolymer for Liquid Deposition Photolithography

3.1   Introduction

The novel fabrication process described in the previous chapter can efficiently fabricate sub-micron resolution 3D index structures within a diffusive photopolymer. In order to maximize the index contrast of the 3D index structures, the diffusive photopolymer must be properly designed and formulated. Initial exposures used PEGDA as the material, attempting to build off the work presented in reference [89] and the numerical simulation presented in section 2.5.3. However, the index structures had very low index contrast, as shown in Figure 3.1. This is ascribed to it's high glass transition temperature and because it is a single component polymer. This motivated design of a multiple-component material for high index contrast in LDP.

The multiple-component material for high index contrast is based on materials initially developed for holographic data storage [123, 124] and integrated optics applications [120]. These materials have the capability to form 3D refractive index structures through localized optical exposure. The process of 3D refractive index structure formation is self developing, so baking or solvent washing are not required for development. Index structure fabrication only requires a minimal dose of energy, approximately 100 mJ/cm^2, and can have a broad wavelength sensitivity range. In order to maximize index contrast, the glass transition temperature of these materials is usually below -20 degrees Celsius, which enables diffusion after exposure. The material after completion of the volume can have low optical absorption
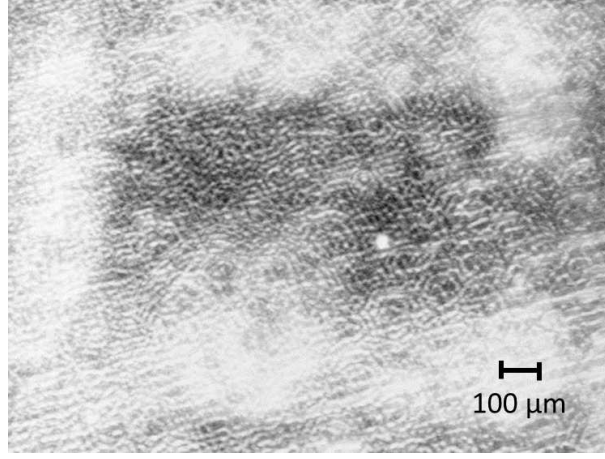
Figure 3.1: DIC micrograph of 10 μm thick single layer index structure written in PEGDA. The lack of index contrast between the structured and unstructured areas results in a poorly resolved DIC image. The weak index contrast demonstrates why a multiple-component material was developed.

and scatter. Demonstrated index contrast can range from to 10^{-3} to 10^{-2} depending on the material components chosen [80] and the fabrication process.

In this chapter, the material design of the diffusive photopolymer used within the LDP fabrication process and the mechanism for index structure formation is presented. The formulation of the diffusive photopolymer and how the material achieve high index contrast is presented. Bulk measurements of the refractive index and polymerization rate are shown to estimate index contrast. The effect the binary index structure feature size has on the index contrast is investigated by writing index patterns with both small and large scale structures and comparing their index contrast. Additionally, the crosstalk between layers is quantified using the scanning optical microscope. The amount of crosstalk is determined by exposing multiple layers with different patterns at varying depths through the volume and measuring the refractive index crosstalk at a singular interface.

3.2   Index structure formation in liquid diffusive photopolymers

Diffusive photopolymers are composed of an initiator and a mixture of one to many monomer species. Index structure formation in diffusive photopolymers is still an active area of research [125, 126], however the predominant theory is that index structures are formed by a spatially controlled increase in the monomer density. The increase in the monomer density is created when structured optical excitation of the photoinitiator initiates polymerization of the monomer in the illuminated regions. This locally depletes monomer in the exposed region, creating a concentration gradient of unreacted monomer between the illuminated and the dark regions. The concentration gradient causes diffusional mass transport of unreacted monomer from the dark regions to the exposed regions. This results in an increased material density and index of refraction in the exposed areas. To enable the process of monomer diffusion, a solid matrix material is required to provide a physical scaffold for the monomer to diffuse into. In one-component photopolymers, this scaffold is formed by incomplete polymerization of a single monomer. Photopolymerization and diffusion of the remaining monomer creates the index pattern, however this results in low index contrast as previously demonstrated. To increase index contrast, two component photopolymers that contain both a low-index and a high-index monomer, where the high index monomer preferentially diffuses into the exposed area have been developed. In these materials, the scaffold enabling monomer diffusion is formed by using a thermal-set matrix as the low-index monomer. However, this thermal-set matrix can not be sequentially layered, which is required for the LDP process, so traditional two-component photopolymers can not be used. Therefore, a two-component mixture, in which both the matrix and high-index diffusing monomer are liquid photopolymers was developed. This two-component mixture can be injected and photo-cured into thin layers like a one-component photopolymer, but can achieve the high-index contrast typical of traditional thermal-set two-component photopolymers. The physical scaffold in this material is formed by optical exposure and polymerization of both monomers, however the high-index

monomer preferentially diffuses into the optically formed scaffolding, creating high contrast index structures.

3.3 Design of liquid two component diffusive photopolymer

The diffusive photopolymer used in this work is a two-component mixture in which both the matrix and high-index diffusing wiriting monomer are liquid photopolymers. To maximize index contrast the material formulation contains two photopolymerizable monomers with different refractive indices and molecular weights. The large molecular weight, low refractive index monomer is intended to be approximately uniform throughout the volume, where the small molecular weight, high refractive index writing monomer density is controlled by photo-patterning it through the volume. An illustration of the material function is shown in Figure 3.2.
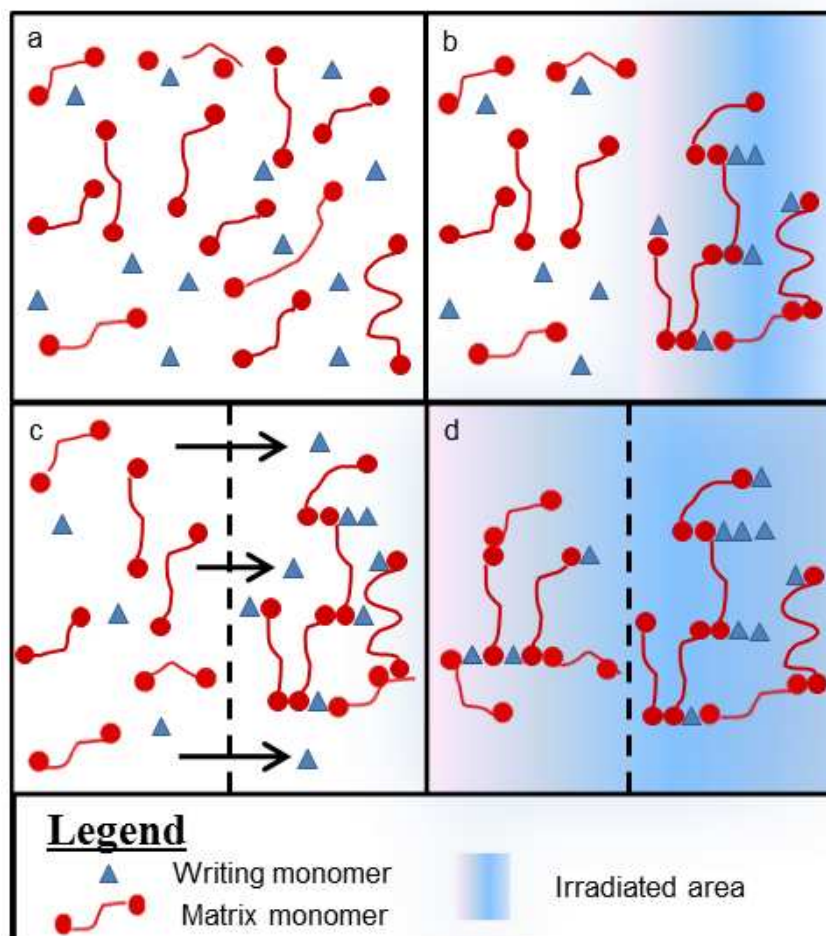
Figure 3.2: Representation of the material function. The low index, high molecular weight, matrix monomer is represented by two red circles connected by a line indicating its multiple functional groups. The high index, low molecular weight, writing monomer is represented by a single blue triangle indicating its single functional group. (a) The mixture of photoinitiator and monomers are injected into the exposure region in the form of a thin liquid layer. (b) A portion of the area is exposed, locally consuming both monomers, creating a low-index solid. (c) Due to its smaller molecular weight, writing monomer preferentially diffuses in to replace that consumed by polymerization, increasing the index of the exposed region. Note that in the LDP system, the majority of this diffusion is out of the inhibited layer through the thin depth of the part, not transversely across the large part width. (d) After the mass transport of writing monomer has concluded, the entire layer is exposed, polymerizing the remaining monomer to create a solid, cross-linked, insensitive polymer with approximately uniform matrix monomer and photo-patterned writing monomer.

To demonstrate the efficacy of this material design and the importance of the high-index writing monomer, a liquid photopolymer with and without the high-index monomer was exposed to the University of Colorado seal pattern. The material without the high index writing monomer develops very low index contrast as shown in Figure 3.3(a), but a material with the high-index monomer under the same exposure conditions exhibits much stronger contrast, as shown in Figure 3.3(b).
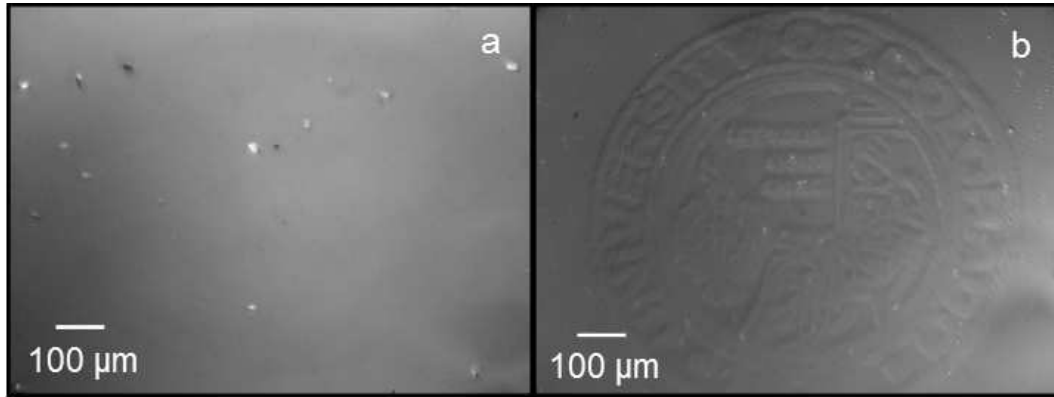
Figure 3.3: Demonstrating the purpose of the writing monomer in the formulation. (a) DIC micrograph of 3 μm thick index structure where material had no writing monomer. (b) DIC micrograph of 3 μm thick index structure with the same exposure conditions as (a) but containing writing monomer.

3.4   Specific material implementation

The photopolymer used to fabricate the structures shown throughout this thesis was made using the solutions shown in table 3.4. The chemical symbols and the respective refractive indices of the formulation components are shown in Figure 3.4. The chemicals tribromo-phenyl acrylate and irgacure 651 were used as received, but Poly(ethylene glycol)-di(urethane methacrylate) (PEA-DUMA) was synthesized at the University of Colorado Boulder.

Poly(ethylene glycol)-di(urethane methacrylate) (PEA-DUMA) is not commercially

Table 3.1: LDP material formulation

Material	Amount (wt %)	function
Poly(ethylene glycol)-di(urethane methacrylate)	95	matrix monomer
Tribromo-phenyl acrylate	4	writing monomer
Irgacure 651	1	initiator
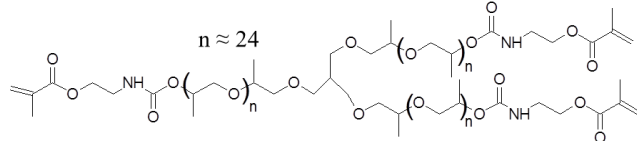
Matrix monomer
Poly(ethylene glycol)-di(urethane methacrylate)
$n_D = 1.4525$
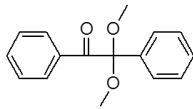
UV Initiator
Irgacure 651
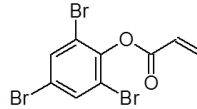
Writing monomer
Tribromophenyl Acrylate
$n_D = 1.5425$, $n_P \sim 1.62$

Figure 3.4: Chemical diagrams and the refractive indices of the liquid components in the LDP diffusive photopolymer.

available, so it was synthesized at the University of Colorado Boulder. Synthesizing (PEA-DUMA) was preferable to using a different, commercially available methacrylate, because PEA-DUMA is large, flexible molecule and there was no methacrylate as large or flexible available. Lower molecular weight urethane methacrylates were tested but resulted in lower index contrast. A large, flexible molecule is desirable, because it maximizes the amount of writing monomer diffusion into the exposed area. The (PEA-DUMA) was synthesized by mixing 92.7 % w/w glycerol propoxylate mw 4300 (Sigma Aldrich), 7.2 weight percent iso-cyanethyl methacrylate(Sigma Aldrich), and 0.1 % w/w dibutyltin dilaurate (Sigma Aldrich)

over 40 degree heat for 10 hours. All components were used as received without additional purification. The chemical components for the synthesis of PEA-DUMA are shown in Figure 3.5.
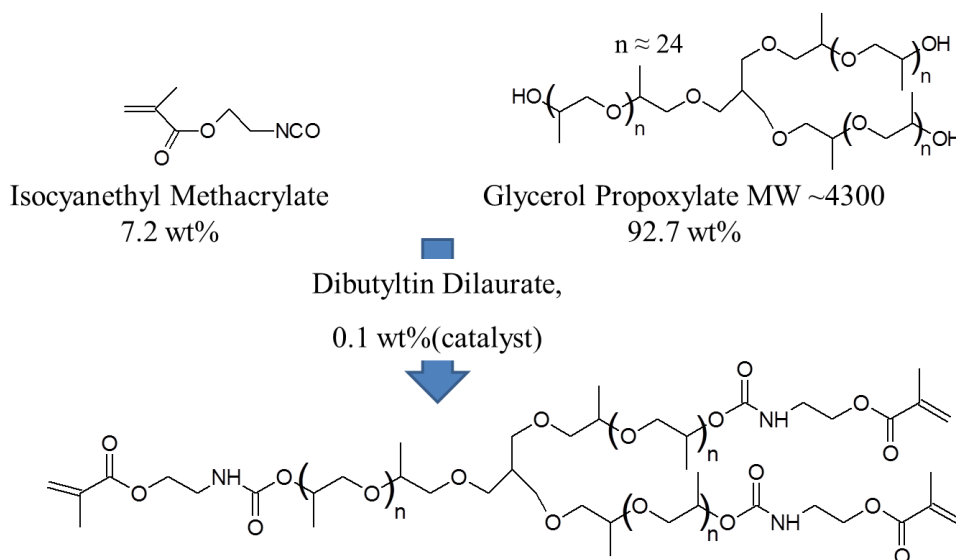
Figure 3.5: Chemical components for the synthesis of Poly(ethylene glycol)-di(urethane methacrylate).

3.5   Material Performance

3.5.1   Shrinkage and dimensional control of the cross-linked polymer

The shrinkage of the material has not characterized, in part because bulk measurements are not relevant and nano-scale dimensional measurements within the closed chamber are difficult. However, to first order, shrinkage is not relevant since if the layer shrinks slightly away from the PDMS or the polymer features shrinks transversely, new liquid material is automatically drawn into the gap and polymerized. Thus, the layer thickness and transverse feature size is approximately independent of shrinkage. This limits potential birefringence of the material from fabrication, because there is little to no shrinkage stress in the volume. This was confirmed by fabricating a 50 layer volume with LDP and imaging it with a micro-

scope with crossed polarizers. The microscope image revealed the sample had no apparent birefringence.

3.5.2   Measured resolution

The smallest index feature that can be written within the material was quantified using a Holographic Material Tester (HMT). The HMT is an optical media characterization tool for measuring the parameters of materials (such as potential transverse resolution, shrinkage, etc.), used in applications such as data storage, lithography and other photonic systems. The HMT has the ability to record multiple holograms at a single location using angle multiplexing, and find the material parameters by analyzing the holograms angular selectivity and diffraction efficiency. A diagram of the optical recording and readout system of the HMT is shown below in figure 3.6.
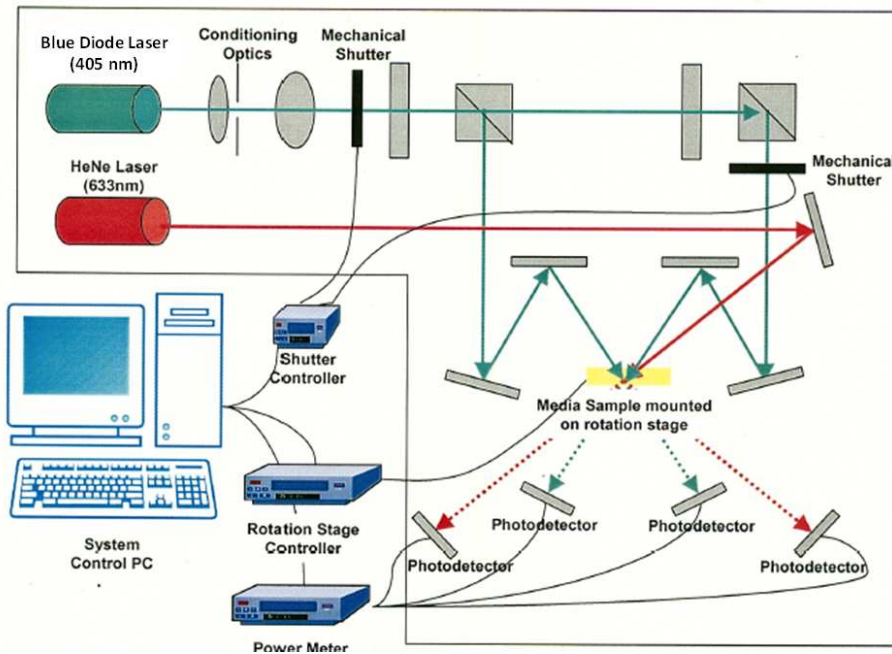
Figure 3.6: HMT optical recording and readout system layout. Image created by InPhase Technologies.

A 50 μm thick sample of the photopolymer used in this work was mounted on the rotation stage of the HMT. The photoinitiator of the photopolymer was changed from Irgacure 651 to TPO to adjust the wavelength sensitivity of the photopolymer; however this does not affect the function of the material. After the sample was mounted, the half angle of the interfering beams of the blue laser diode were set to 45 degrees, resulting in a 286 nm pitch grating with 143 nm line widths. The photopolymer was exposed for 15 seconds with an irradiance of 10 mW/cm^2. After the material was allowed to diffuse for 10 seconds, the hologram was readout by allowing a single arm of the blue laser propagate through the sample, while simultaneously rotating the sample from -2 to 2 degrees, recording the diffraction efficiency at 0.01 degree intervals. The angular scan results are shown below in figure .
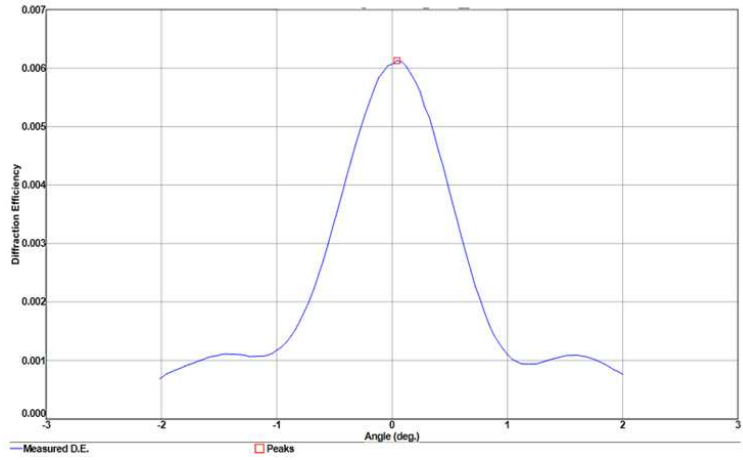
Figure 3.7: Diffraction efficiency vs. angle of the sample for a hologram written and sampled with the optical setup shown in Figure 3.6.

The angular selectivity of the diffraction efficiency with a peak at 0 degrees, confirms there is a high fidelity holographic grating with the desired pitch of 286 nm. This demonstrates that transverse index structures with resolution less than 150 nm can be recorded within the material, showing that transverse resolution is limited by diffraction and not the material.

3.5.3 Estimating achievable index change from bulk measurements

The refractive index of several variants of the liquid formulation were measured with an Abbe Refractometer(Sodium D line), a common optical device that measures the refractive index of liquids with high-precision. These variants included a control 0% TBPA, the formulation with (4% TBPA) and the formulation with twice the writing monomer (8% TBPA). The result of the measurement are shown in Figure 3.8.
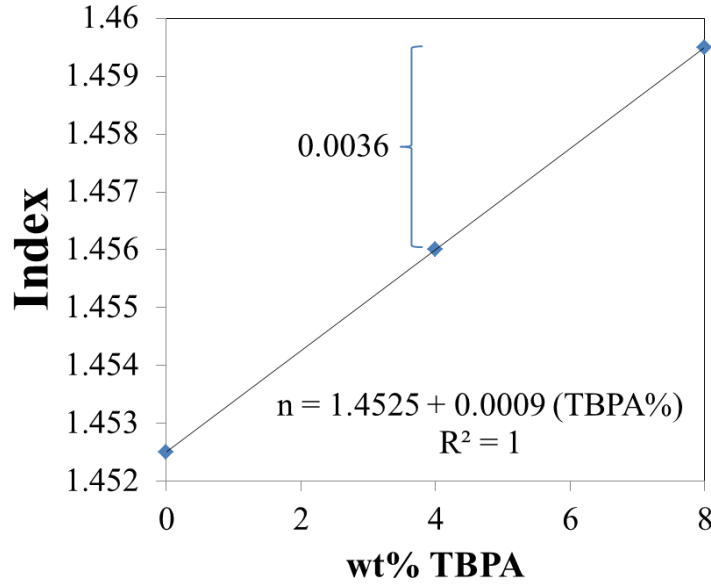
Figure 3.8: Refractive indices for solutions of the diffusive photopolymer with varying concentrations of TBPA. The refractive indices of all the material solutions were measured with an Abbe Refractometer.

To estimate the achievable index contrast of the material, complete conversion of the 4% TBPA in the patterning exposure was assumed. It was assumed that monomer is not depleted in the surrounding liquid and that diffusion is able to fully replace the TBPA consumed by polymerization. After flood cure, the TBPA concentration in the initially unexposed regions will then be 4% while TPBA concentration in the initially exposed regions will be 8%. From Figure 3.8, the estimated achievable index change is 0.0036. This corresponds to an M number of 4.4 per 200 microns of thickness at $\lambda = 0.5 \mu m^2$, which is typical

of commercial-grade holographic films [127].

To confirm the accuracy of the abbe refractometer measurements, the refractive index of several variants of the polymerized formulation were measured with a Metricon prism coupler [128, 129]. The variants measured were 0, 2, 4, 5, 7, 8 and 9 (% w/w.) TBPA, as shown in Figure 3.9.
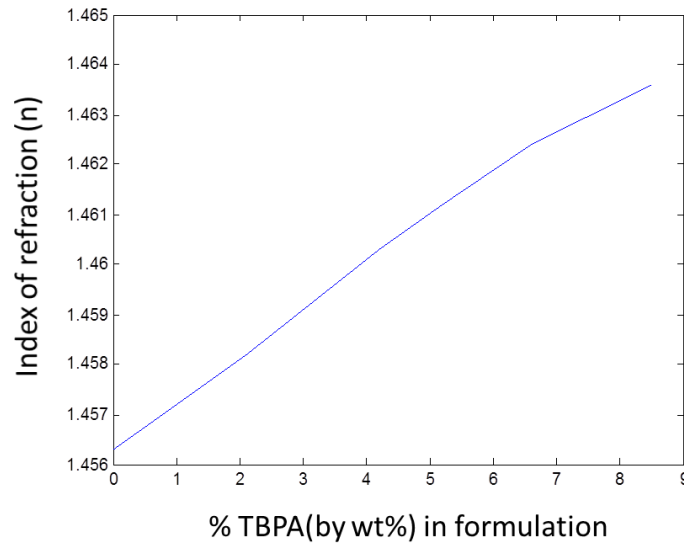
Figure 3.9: Measured refractive index for bulk, polymerized samples using a Metricon prism coupling device.

This confirms that the estimated achievable index change of the material is approximately 0.0035. However, the index contrast of the waveguide array measured by a scanning optical microscope was approximately 0.1, as shown in Figure 2.19c. If the same assumptions were made as before and the amount of TBPA replacement was forced to matched the measured index change, the amount of TBPA would be occupy, approximately 100 percent of the volume in the center of the waveguide, as shown in Figure 3.10.

Not accounting for a change in free volume in the high index regions, this would imply that the PEA-DUMA was completely excluded in the those regions. Another potential explanation for the large index contrast is a significant amount of free volume was replaced
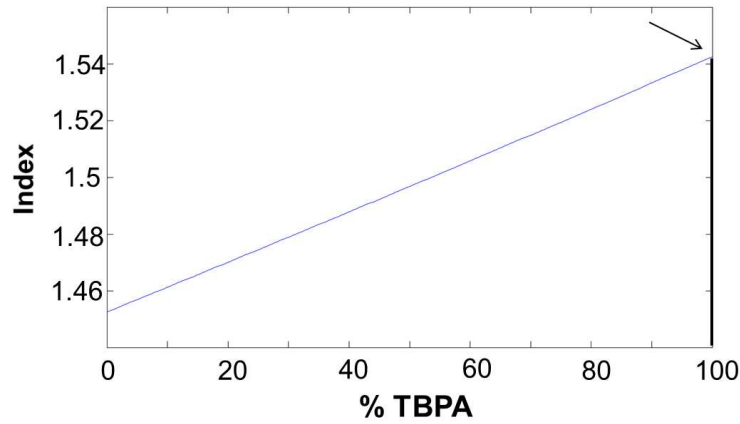
Figure 3.10: Refractive indices for solutions of the diffusive photopolymer with varying concentrations of TBPA. The graph demonstrates to achieve the measured index contrast shown in Figure 2.19(c) there must locally be 100 percent TBPA.

with the TBPA [130]. Since free volume has a refractive index of 1, replacement with TBPA would result in a very large index change for even a small percentage of replacement.

3.5.4 Refractive index contrast of large binary structures

In order to quantify the achievable index change for large binary structures, a single binary exposure of the University of Colorado buffalo logo was fabricated and measured with the scanning optical microscope. The refractive index map of the University of Colorado buffalo logo exposure is shown in Figure 3.11. Figure 3.11 shows the refractive index recording has poor fidelity. The edges of the structure have a higher index than the other portions of the structure.

The important parameter for high fidelity structure formation, as discussed in reference [79], is the normalized diffusion to reaction rate constant, R. When the normalized diffusion rate is greater than the polymerization rate, (R >1), monomer is never depleted at the center of the exposure so polymerization remains linear until saturation, resulting in high fidelity recording. Additionally, larger R results in higher index contrast. When the normalized diffusion rate is less than the polymerization rate, (R <1), depletion of monomer at the
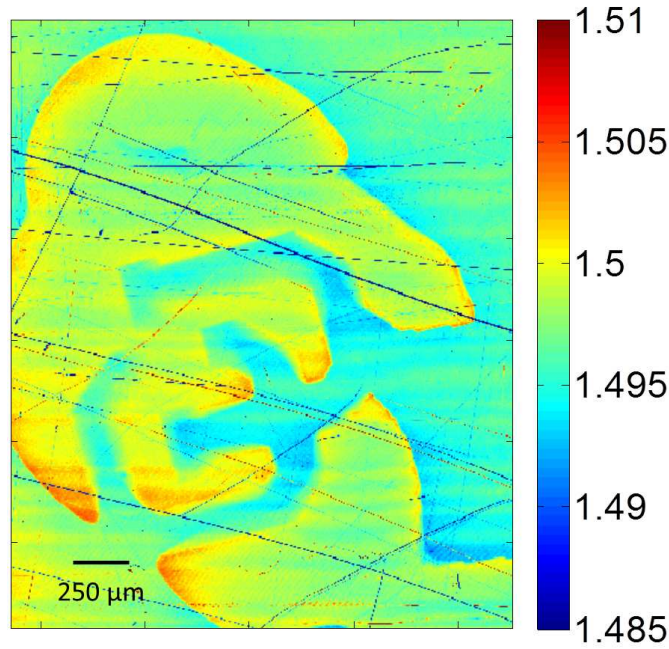
Figure 3.11: Refractive index map of a single binary exposure of the University of Colorado buffalo logo, the layer thickness is approximately 30 μm.

center of an exposure can slow polymerization, leading to poor recording fidelity. Therefore, the refractive index recording of the University of Colorado buffalo logo most likely had a normalized diffusion rate smaller than the polymerization rate. This is demonstrated at the edge of the buffalo pattern, where higher spatial harmonics developed during recording of the structure.

In order to increase the fidelity of large binary structures, the normalized diffusion to reaction rate constant, R, of the recording must be increased. To increase R there are three methods: reduce the intensity of light, reduce the size of the fabricated structure, or increase the monomer diffusion coefficient. The monomer diffusion coefficient can not be easily increased unless the material system is changed. The intensity of light for a recording can be decreased but at the cost of additional exposure time for each layer, increasing total fabrication time. The size of the fabricated structure can be decreased by reducing the layer thickness of each layer. Beyond increasing R, which results in high fidelity, high contrast

recording, the axial resolution of the volume would increase as well. Additionally, total fabrication time for a volume would decrease, as demonstrated by Figure 2.2.

3.5.5   Determining physical mechanism of crosstalk between layers

When the volume contains multiple patterned layers, the material response of each layer varies. DIC images of volumes with multiple patterned layers revealed the index contrast of the second exposure to be reduced within the body of the first exposure, indicating crosstalk between the independent layers. However, the DIC microscope is a qualitative measure of refractive index, so the precise amount of crosstalk can not be determined. Additionally, a DIC image does not contain information about the refractive index distribution in depth, so potential sources of crosstalk cannot be easily tested. To demonstrate crosstalk, multiple binary exposures of University of Colorado logos were written at different depths in the fabricated volume. The fabricated volume was then measured with the scanning optical microscope to quantify the crosstalk, shown in Figure 3.12.
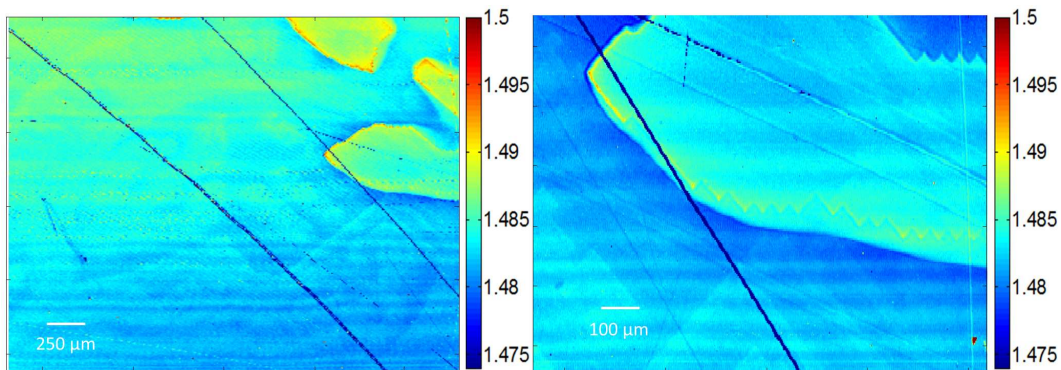
Figure 3.12: Refractive index map of binary exposures of different University of Colorado logos written at different depths in the fabricated volume. The first layer, measuring 20 μm, was structured with the CU buffalo logo, while the 2nd layer was structured with the CU seal logo. (a) Refractive index map of the first layer, demonstrating the second exposure is unintentionally written within the first layer. (b) magnified image of (a) showing the CU seal pattern has been written in the first layer in both the structured and unstructured areas of the first layer.

Figure 3.12 shows the second exposure is unintentionally written within the first layer, demonstrating crosstalk between the layers. A potential explanation for the appearance of the CU seal logo in the first layer is the structure is within the scanning optical microscope depth of field. To demonstrate this is not the case, the NA of the lens used in the scanning optical microscope was increased by a factor of two, reducing the depth of field by a factor of four. A refractive index map of the same fabricated volume with the higher NA lens is shown in Figure 3.13.
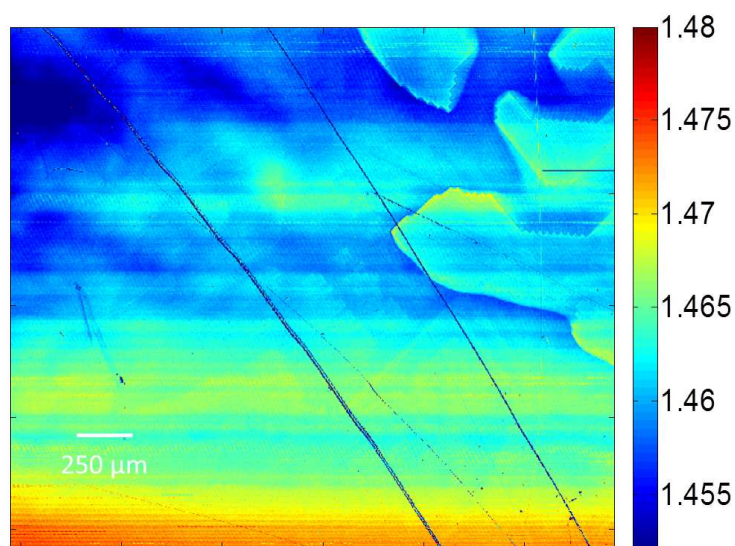
Figure 3.13: Refractive index map of first layer of the same fabricated volume as shown in Figure 3.12, but the depth of field of the scanning microscope was decreased by a factor of four, demonstrating the crosstalk shown in Figure 3.12 was not an artifact of the microscope.

Figure 3.13 illustrates the existence of crosstalk in the refractive index distribution between structured layers. Potential sources of this crosstalk are diffusion of reactants into or out of the initial layer and changes in thickness of the liquid layer due to depletion of inhibitor. However, changes in thickness of the liquid layer due to depletion of inhibitor is unlikely the mechanism causing the crosstalk. While this effect is demonstrated in Chapter 5, it results in a change in the thickness of the written layer and would not effect the index distribution of a previously written layer. The more likely cause of the observed crosstalk is diffusion

of unreacted initiator from unexposed liquid monomer into the previously fabricated layer. While the diffusion coefficient of unreacted initiator is unknown, comparing its molecular weights to TBPA suggest they should have similar diffusion coefficients. Therefore, if there is complete replacement of TBPA in a previously exposed layer, there will also be complete replacement of unreacted initiator.

To demonstrate that this is indeed the most likely cause of the crosstalk, the thickness of the first layer was increased by 30 μm, increasing the diffusion length by a factor of 2 and diffusion time by a factor of 4. This should decrease the amount unreacted initiator within the portion of the layer that can be resolved with the scanning optical microscope, decreasing the amount of measured index change of the second structured pattern within the first layer. The refractive index map of the volume is shown in Figure 3.14.
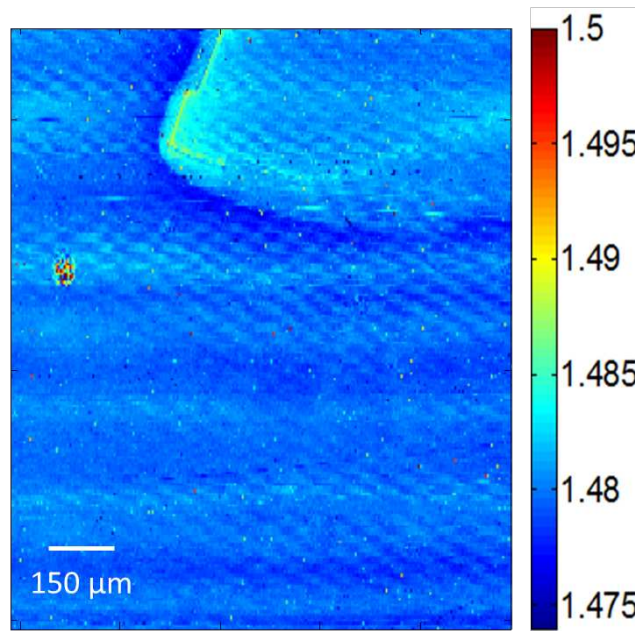
Figure 3.14: Refractive index map of multiple binary exposures of two different University of Colorado logos at different depths in the fabricated volume. The layer thickness of the first layer, where the buffalo logo was written, was increased by 30 μm compared to Figure 3.12.

In addition to decreasing the amount of crosstalk, Figure 3.14 also shows a decreased index change in the structured pattern, particularly in the center of the pattern. This is expected because large structures rely on lateral diffusion of unreacted monomer to increase the refractive index. The increase in thickness of the first layer, increases the diffusional length of unreacted monomer by the same amount as unreacted initiator, reducing the amount of index change. This demonstrates that a similar molecular mobility of unreacted initiator and monomer is the most likely cause of the crosstalk. Therefore, crosstalk could potentially be significantly reduced, if the mobility of the unreacted initiator was decreased in comparison the the unreacted monomer. The mobility of unreacted initiator could be decreased by increasing the size of the unreacted initiator molecule by attaching a large pendent molecule to it. This addition to the material is discussed further in the future work chapter of the thesis.

3.6   Summary and conclusion

In this chapter, the function of the diffusive photopolymer used with the LDP process and how it was designed to achieve high index contrast was presented. The maximum refractive index contrast demonstrated in Chapter 2, is shown to be an order of magnitude larger than what is expected from the estimated achievable index contrast using bulk measurements. Further analysis of the high index contrast structures needs to be performed in order to accurately characterize the mechanism for high index contrast and explain the discrepancy between bulk and quantitative measurements. A potential tool for further exploration is confocal Raman spectroscopy [131], which has the ability to quantify the spatial differences in the chemical composition of the volume, described further in Chapter 6.

The refractive index map of the CU buffalo binary index structure demonstrates the importance of the ratio between the diffusion rate and polymerization rate for high fidelity structure formation. In order for large binary structures to have high fidelity, thin layers must be fabricated to reduce the longitudinal diffusion distance of unreacted monomer. This has

the additional benefits of increasing longitudinal resolution and decreasing total fabrication time. The amount of crosstalk between layers was quantified, and the likely mechanism for the crosstalk hypothesized and experimentally demonstrated. However the crosstalk does not limit LDP's ability to fabricate photonic devices. This is demonstrated in the next chapter, which describes the fabrication of large, arbitrary gradient index structures in LDP.

Chapter 4

Writing Gradient Index Structures with Liquid Deposition Photolithography

4.1   Introduction

In implementations of LDP shown thus far, the system was only capable of exposing layers with binary light patterns. Here, a method of fabricating nearly arbitrary gradient index profiles throughout a diffusive photopolymer volume is presented. To create GRIN structures, control of the exposure light intensity distribution is required, because there is a direct correlation between the induced index change and the energy dose delivered by the light source. The desired index pattern in a layer can be fabricated by an appropriate exposure light intensity distribution and dose.

In this chapter, the optical system is redesigned to include a deformable mirror device (DMD) to enable gray-scale structuring. 125 μm thick, single layer samples are fabricated to determine exposure parameters that result in high fidelity, high contrast GRIN recordings. The exposure doses are then applied to a 25 layer, 125 μm thick volume fabricated using the LDP process. The throughput and index contrast of the LDP fabricated volume are shown to be higher compared to the single 125 μm thick layer volume. Finally, LDP is used to fabricate 125 μm thick volumes containing index structures with 10 different Zernike polynomials, demonstrating LDP's ability to create high fidelity, nearly arbitrary GRIN structures.

4.2   GRIN structuring in LDP

4.2.1   Light source

The light source used for LDP in previous chapters, was a 365 nm line of an ion argon laser that used a moving diffuser to reduce the spatial coherence of the laser. While this light source met technical specifications, it was expensive, heavily used and a poor use of a coherent light source. Therefore, a high pressure mercury vapor arc lamp that provided spatially incoherent light without the use of a diffuser was implemented. High pressure mercury vapor arc lamps are highly reliable and produce very high flux densities in the ultra violet spectral region.The lamp has an output irradiance of 10 mW/cm^2 at the 365 nm spectral line over a 1" diameter. It also has a field uniformity of +/- 5 percent, enabling high fidelity gradient light patterns, and beam divergence of 1.5 degrees, allowing high throughput through the optical system. An image of the high pressure mercury vapor arc lamp and it spectrum is shown in Figure 4.1. To reduce the absorption spectrum to contain only the 365 nm spectral line of the mercury arc lamp, a notch filter was used to remove wavelengths lower than 350 nm and higher than 450 nm from the system. The absorbed spectrum is further reduced by the absorption spectrum of the initiator, because it has no absorptivity at the 405 and 435 nm lines of the lamp.

4.2.2   Determining the gray-scale pattern generator

There are multiple ways to create a gray scale pattern generator to structure each layer within LDP. In the following sections different implementations will be outlined and potential strengths and limitations of each implementation discussed. Many of the gray scale pattern generator implementations have been previously discussed in Chapter 2, with the focus being fabricating multiple layers of binary index structures section. The discussion in the following sections will be an extension of that section with the focus on gray scale structuring of layers.
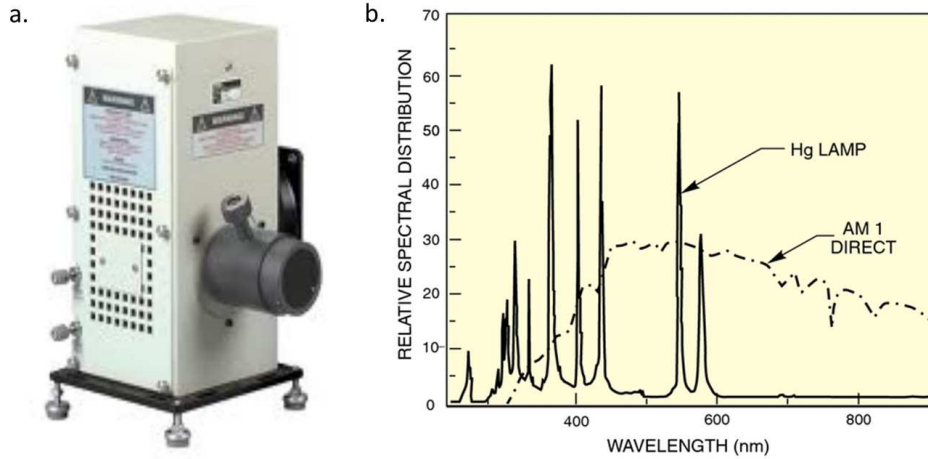
Figure 4.1: Light source used in LDP. (a) Image of lamp chosen as light source for the system. The lamp's intensity uniformity is +/- 5 % and its beam divergence is 1.5 degrees. (b) Spectrum of Mercury Arc lamp.

A way to create 2D gray scale pattern generator is to use a large gray-scale mask containing multiple patterns, which is dynamically translated transversely by computer-controlled stages. Gray-scale masks have been used to exposing photopolymer for optical device fabrication [132, 133], demonstrating that gray-scale masks could be used for LDP. However, unlike binary masks, which are widely available and inexpensive, gray-scale masks can be expensive or lack performance. High quality gray-scale mask can be fabricated in a photosensitive glass by changing their transmission with either a laser or electron beam [134, 135]. However, these masks are very expensive and time consuming to fabricate, creating long lead times between mask design and fabrication. A more cost-effective approach is to use commercial binary chrome masks to approximate a gray-scale light distribution [136, 137]. This is done by modulating the size and distribution of transparent pixels in the chrome mask [138] to create the different light transmission levels. However, the pixel size of the mask requires higher resolution than the optical projection system, limiting potential feature resolution. Additionally, the sharp edges of all the binary pixels create unwanted diffraction,

reducing fidelity of the recording pattern.

Another way to create gray-scale pattern generator is to implement a laser scanning system. The laser scanning system creates the gray-scale pattern by varying the exposure time at each voxel position. Even though the exposure is sequential it is significantly faster than the time scale of polymerization in the material. It can takes a laser scanning system less than a second to draw an exposure pattern, while the polymerization time of the material is over tens of seconds [95]. However, the material response is hard to predict and model for small transverse structures because oxygen can readily diffuse during the recording, rapidly changing the material response. To expose a million features simultaneously a liquid crystal display can be imaged onto the sample. By controlling the voltage applied across the liquid crystal layer in each pixel the different light levels can be achieved at each pixel. The LCD can contain as many as 12801024 pixels, have a pixel size of 20-30μm and a 100:1 contrast ratio [42]. The pattern can be modulated up to 500 Hz [97], two orders of magnitude faster than a chrome-on-glass mask.

Here I use a DMD as a gray-scale pattern generator. The gray scale pattern is achieved by binary pulse width modulation of the micro-mirrors [139] and enables 256 different light levels to be modulated at 40 Hz, over two orders of magnitude faster than the polymerization time. It has a superior modulation rate, contrast ratio and pixel size compared to a LCD. The cost over the lifetime of the DMD will most be less than gray-scale masks because after the capital investment in the DMD no additional materials need to be purchased. Conversely, a new gray-scale mask must be purchased each time the required refractive index distribution is changed, increasing cost and development time.

4.2.3   Implementing the DMD in the LDP optical system

To implement the DMD within LDP, the optical system shown in Chapter 2 must be redesigned to accommodate the operation of the DMD. The DMD device generates a gray-scale pattern by reflecting light at different angles for the "off" and "on" states of each pixel

within the 2D array. The DMD pixels are micro-mechanically actuated on their diagonal to obtain the different reflection angles. Binary pulse width modulation of the micro-mirrors enables 256 different light levels to be modulated at 40 Hz. Greater bit depth can be achieved at the cost of reduction in modulation rate. An illustration of the actuation of the "off" and "on" positions for a single pixel is shown in Figure 4.2.
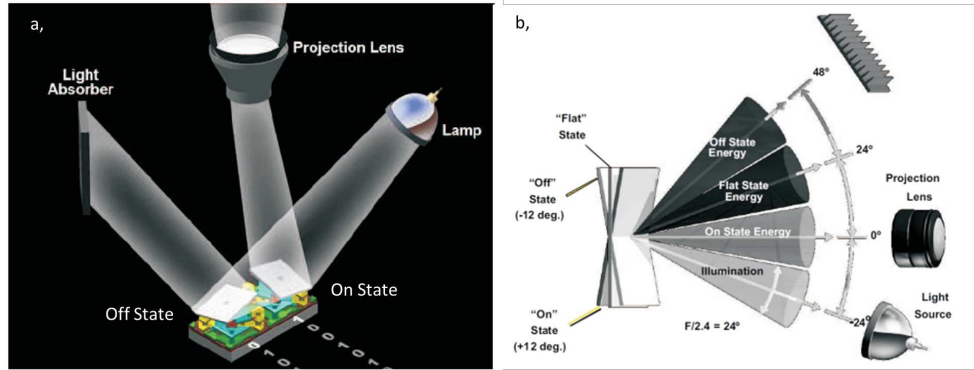
Figure 4.2: Detailed operation of a single pixel in the DMD array. (a) An illustration of the mechanical position of a single mirror of the Deformable Mirror Device in both the on and off state. In the "on" state it reflects light into the entrance pupil of the projection optics and the "off" state reflects light away from the projection optics. (b) An additional illustration showing the projection angles for each state of the DMD [140].

To best accommodate the DMD it was placed directly above the piston and lithographic chamber and the DMD's image plane was projected into the with a projection system. The projection system is a pair of matched UV transmissive doublets, which are attached to a kinematic mount to enable access to the lithographic chamber. The optical setup of showing the light source, exposure chamber and DMD is shown in Figure 4.3.

For the pre-cure and post-cure process steps, unstructured, uniform light is required to create a phase flat background within each fabricated layer. To create the a uniform light distribution a moving diffuser was translated above the chamber window. This increased the light uniformity to -/+ 1% as well as the angular content of the light, which has been shown to reduce unwanted index structures from developing [127].
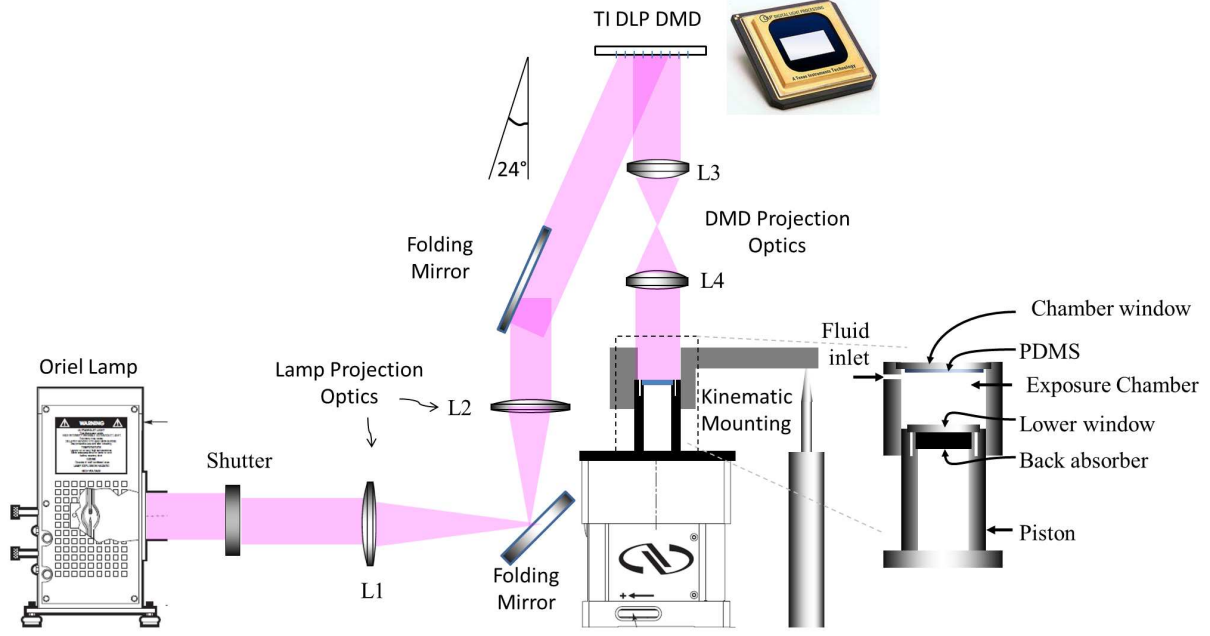
Figure 4.3: The optical setup of LDP. Light is relayed from the output of the Oriel lamp to the DMD using L1 and L2. Two UV doublets are used to project the DMD image plane into the lithographic chamber. L1 and L2 are UV transmissive singlets with a focal length of 250 mm. L3 and L4 have a focal length of 60 mm.

4.3   Quantitative index measurement of GRIN structures

In order to make controllable GRIN lenses and more complex arbitrary gradient index volumes, quantitative index measurements of the fabricated GRIN structures are required. Quantitative index measurements enable proper calibration of the fabrication system. Previous quantitative imaging used a scanning optical microscope to measure the refractive index distribution of the surface of a LDP fabricated volume. However, this imaging method is time consuming because it requires a long, iterative alignment procedure and it must raster through 4 x 10^6, 50 nm^2 voxels with a 50μm/s transverse scan speed to produce the 2D refractive index map. This high resolution, quantitative measurement was required to resolve volumes with μm scale structures, such as the waveguide array. However a high resolution refractive index map is not required to accurately measure slowly varying GRIN structures.

Therefore, I use a Shack-Hartmann wavefront sensor (SHWS) [141], to quantitatively characterize the index profile of arbitrary GRIN structures fabricated by LDP.

The SHWS significantly reduces the amount of time required to produce a 2D refractive index map, compared to the scanning optical microscope. Imaging time is reduced because the alignment procedure is not time consuming and the entire volume is measured with a single image. The SHWS quantitatively characterizes the index profile of a volume by measuring the optical path length through the sample. The optical path length of the structure can be compared to the optical path length of an unstructured area to determine the optical path length difference. The optical setup using the Shack-Hartmann wavefront sensor is shown in Figure 4.4.
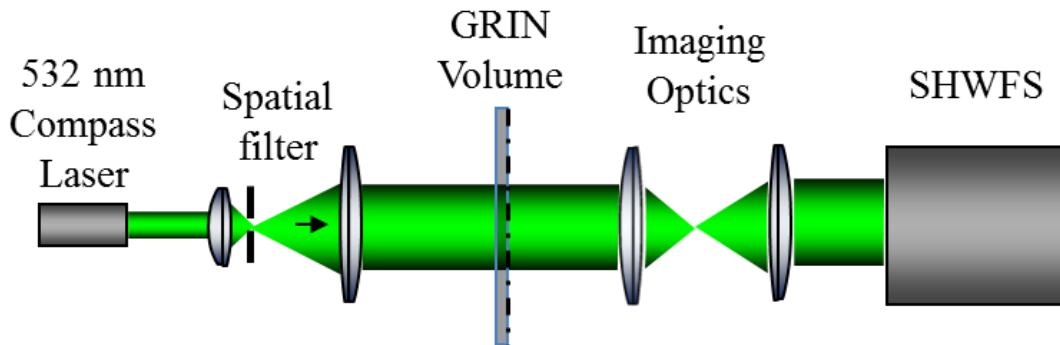
Figure 4.4: The optical setup for quantifying the index profile of arbitrary GRIN volumes fabricated with LDP using a Shack-Hartmann wavefront sensor.

In the optical setup, a 532 nm compass laser is spatially filtered and collimated to a beam diameter of 6 millimeters to ensure the entire GRIN structure is illuminated. The illuminated GRIN structure is then imaged by a pair of doublet lenses onto a Wavefront Sciences Shark-Hartmann wavefront sensor, measuring the phase of the GRIN structure. The magnification of the imaging component is varied to have the structure fully fill the aperture of the wavefront sensor, resulting in the best spatial resolution.

4.4 Parabolic GRIN structure fabrication

4.4.1 Introduction

In this section, parabolic GRIN structures are fabricated in 125 μm thick volumes to determine exposure parameters and process steps required to fabricate GRIN lenses. GRIN lenses are highly used optical devices that can reduce the complexity of optical components, increase reliability and/or reduce cost. GRIN lenses create the optical path length difference to perform the lens function by varying the index of refraction in the material. There are two way the GRIN is modulated to perform the lens function: axially, where the index varies parallel to the optical axis, and radially, where the index varies perpendicular to the optical axis. Radial GRIN lenses have been shown to correct chromatic aberrations and reduce field curvature in optical systems [142], enabling the reduction of lens elements. Axial GRIN lenses have been shown to have performance similar to aspheric lenses [143, 144].

GRIN lenses have several features that make them more well suited to meet specific application requirements compared to homogeneous refractive index lenses. The flat surfaces of GRIN lenses can simplify the mounting of the lens, making them more attractive for photocopiers, scanners and telecom components [145], where many very small lenses need to be mounted together. The flat surfaces also allow a GRIN lens to be connected to an optical fiber [146] that enables collimation or focusing at the output of the fiber. GRIN components can be combined with optical coherence tomography [147, 148] to improve lateral resolution and scanning speed for biomedical imaging. Gradient index components can be combined with homogeneous refractive index lenses to enhance the focusing power, correct aberrations and provide additional degrees of freedom for optical system optimization [149, 150].

4.4.2 Current methods

Several methods have been developed to fabricate GRIN lenses [151], such as neutron irradiation [152], chemical vapor deposition (CVD) [153], ion exchange and diffusion [154]

and polymerization [86]. Certain fabrication methods are often more well suited than others to meet specific requirements for different applications. Neutron irradiation creates a GRIN distribution by changing the index of refraction of boron glass (ex. BK7 glass) by locally altering the boron concentration. The variation in the index of refraction is approximately linear to the neutron irradiation dose, enabling arbitrary GRIN patterns and high fidelity GRIN recordings. However, large neutron doses are required to induce the index change and the fabricated GRIN pattern can disappear over time.

The CVD technique fabricates GRIN lenses by sequentially depositing thin layers of glass materials onto a substrate, where each layer has a homogeneous index of refraction The GRIN pattern is produced by depositing glasses with different refractive indices as the volume is created. Due to the nature of the recording the GRIN varies axially through the volume. However, CVD has limitations for large diameter lenses due to the step index formation by the deposition process.

The ion exchange and diffusion technique creates a GRIN lenses by diffusing ions from a bath of salt(ex. lithium bromide) into a glass substrate where ions from the bath replace the ions originally residing in the glass. The ions have different densities and different refractive indices, resulting in a GRIN distribution in the glass matching the diffusion profile of the ions. Both radial and axial GRIN lenses have been demonstrated with this technique [155]. The ion exchange technique can make lenses with diameters ranging from 0.5 - 10 mm and is the main technology used for mass production. However, ion diffusion profiles limit potential index profiles formed to either Gaussian, Lorentzian or linear, making arbitrary GRIN distribution impossible to fabricate with the method.

Several methods have been developed to fabricate GRIN lenses in polymers. GRIN lens rods have been fabricated in polymers through thermal treatment [156] and UV irradiation [157], however the index pattern of these lenses applications GRIN lenses have also been fabricated in diffusive photopolymers by exposing 100 μm - 1 mm thick, flat samples with a defocused Gaussian beam [86]. Arbitrary radial GRIN patterns are possible with this

technique if a gray-scale pattern generator is used in the exposure system. However, GRIN lens diameters were practically limited to 100's of microns because of the required diffusion time for development. Large diameter polymer GRIN lenses measuring over 50 millimeters in diameter have been fabricated using multiple monomers and longitudinal diffusion to create the gradient index profile [158]. However, the fidelity of the resulting lenses was poor, the fabrication procedure was time consuming and axial GRIN patterns cannot be fabricated.

Liquid deposition photolithography of diffusive photopolymers offers a promising alternative to existing GRIN lens fabrications techniques. The sequential deposition and exposure of sub-micron thin layers enable the fabrication of both axial and radial GRIN lenses. It also offers the potential to fabricate more complex GRIN lenses, where the refractive index distribution can vary both radially and axially. Additionally, the processing of μm thin layer reduces the required diffusion time for development, allowing large polymer GRIN lenses to be fabricated. The ability to change the index distribution for a wide range of depths allows the fabrication of additional optical elements in the same volume, yielding hybrid optical systems.

4.4.3   Parabolic GRIN structure fabrication

To determine the exposure parameters for high refractive index contrast and fidelity, parabolic GRIN structures are fabricated in 125 μm thick volumes. This is not thick enough to perform the lens function, however the exposure parameters determined here can be applied to the fabrication of thick volumes. The index profile of the parabolic structures written can be described by

$$n^2(x, y, z) = (n_0 + \Delta n)^2 [1 - (A)(x^2 + y^2)] \quad \text{for} \quad sqrt(x^2 + y^2) < a, 0 < z < t$$
$$n(x, y, z) = n_0 \quad \text{for} \quad sqrt(x^2 + y^2) > a, 0 < z < t$$

$$(4.1)$$

where n is the refractive index at any spatial position within the structure, n_0 is the refractive index of unstructured polymer, Δn is the peak index change, t is the thickness of the volume and A is the gradient constant. The parabolic light pattern used to expose the material is shown in Figure 4.5.
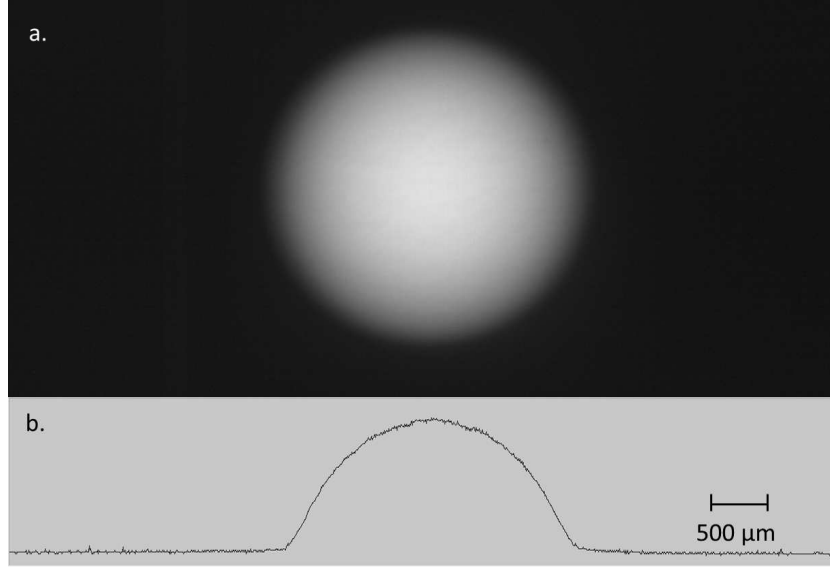
Figure 4.5: Patterned exposure used for all fabrications. (a) Image of parabolic light pattern used to expose the material. (b) cross-section of measured light intensity.

To determine the exposure parameters for high refractive index contrast and fidelity, 125 μm thick, single layer photopolymer volumes were fabricated. To simulate an LDP exposure, liquid photopolymer was cast between the chamber window and a microscope slide. The thickness of the volume was set to 125 μm by spacers placed next to the photopolymer. After the samples were written, the chamber window was removed and liquid photopolymer was poured onto the top of the polymerized volume to enable longitudinal monomer diffusion. If transverse diffusion was relied upon to develop the structures, total diffusion time for a single volume would be longer than a month. After the samples were allowed to develop, the refractive index change and fidelity of the GRIN structure was quantitatively measured using the SHWS.

4.4.3.1 Pre-cure process step for high fidelity exposure

To fabricate parabolic GRIN structures with a fidelity of 95% or greater, a pre-cure is required before the patterned exposure. The fidelity of the parabolic GRIN structures was quantified by the Pearson correlation coefficient. For the binary index structures shown in Chapter 2, index contrast was optimized with an exposure dose of 250 mJ/cm^2 and no pre-cure. A parabolic GRIN structure with a patterned peak exposure dose of 250 mJ/cm^2 is shown in Figure 4.6.
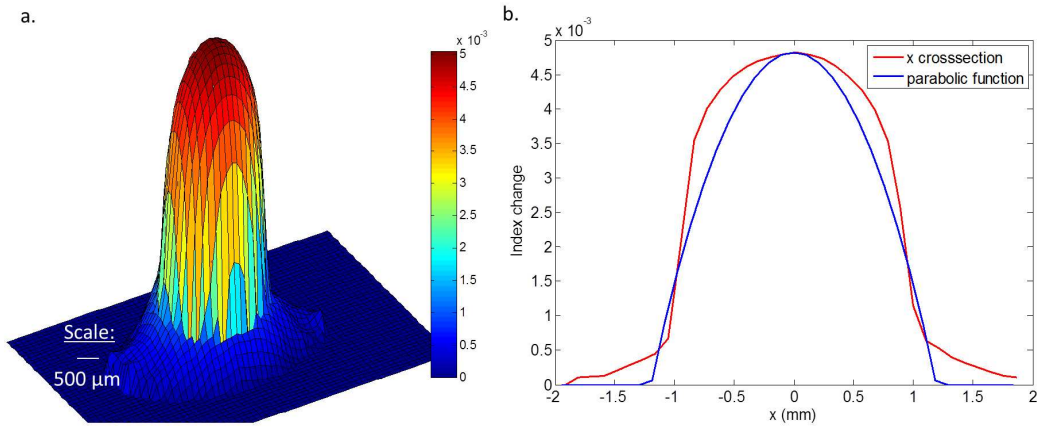
Figure 4.6: Quantitative measurement results of a parabolic GRIN structure with an patterned exposure dose of 250 mJ/cm^2. (a) mesh plot of measured GRIN structure. (b) line plots of cross section through the center of the measured index profile (red) and the intended parabolic profile (blue)

Figure 4.6 demonstrates a parabolic GRIN has good but not the fidelity demonstrated by similar techniques [86]. The parabolic GRIN profile is visibly narrowed compared to the intended pattern and the spatial area directly adjacent to the peak appears to have been overexposed. The measured fidelity of parabolic GRIN structures fabricated with patterned peak exposure doses of 100-300 mJ/cm^2 were less than 0.955 and had similar profiles as the profile shown in Figure 4.6.

To increase the fidelity of the parabolic GRIN structures a pre-cure was done before the patterned exposure. Adding a pre-cure to an exposure to remove oxygen has been

demonstrated to improve fidelity of GRIN recordings [95]. An example of an parabolic GRIN profile that has included a pre-cure is shown in Figure 4.7.
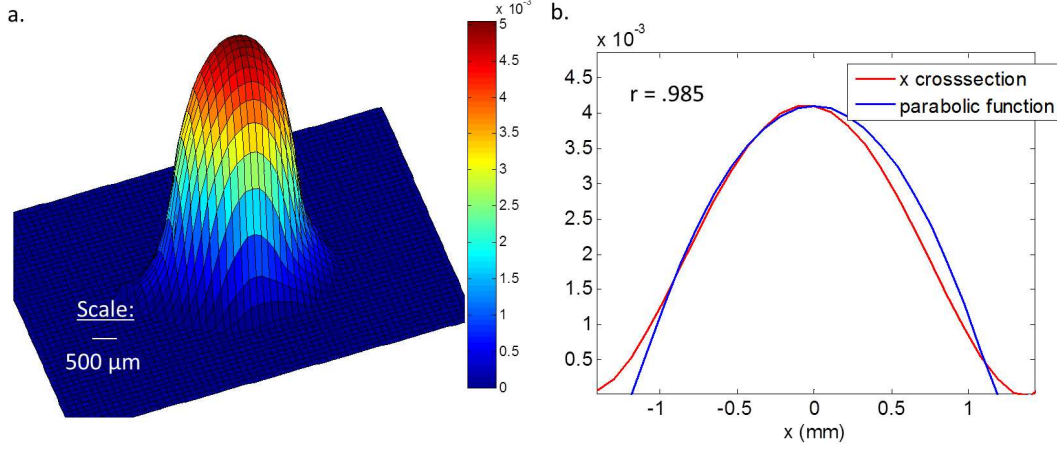
Figure 4.7: Quantitative measurement results of the parabolic GRIN structure with an patterned peak exposure dose of 100 mJ/cm^2 and precure dose of 40 mJ/cm^2. (a) mesh plot of measured parabolic GRIN structure. (b) Line plots of cross section through the center of the measured index profile (red) and the intended parabolic profile (blue). The Pearson correlation coefficient of the written parabolic compared to the intended parabolic pattern is 0.985

Figure 4.7 demonstrates that by including a pre-cure exposure the fidelity of the parabolic GRIN structure improves without significantly reducing index contrast. The Pearson correlation coefficient is 0.985, higher by 0.045 compared to the parabolic GRIN structures shown in Figure 4.6. The measured index contrast is 0.0041 which is within 10% of the index contrast demonstrated by parabolic GRIN structures with no pre-cure. The next section determines the optimal pre-cure and exposure dose for high index contrast, high fidelity parabolic GRIN recordings.

4.4.3.2   Determining high fidelity exposure parameters

To determine the effect the patterned and pre-cure exposure dose has on the refractive index change and fidelity of the structure, the refractive index profile was measured for samples with different pre-cure and patterned exposure doses. The pre-cure doses used were

20, 40, 60, and 80 mJ/cm^2. The patterned peak exposure dose was increased in 20 mJ/cm^2 increments until the measured peak index change saturated and the fidelity of the GRIN structure began to significantly decrease. The measured peak index change for each parabolic GRIN structure as a function of exposure dose for different pre-cure doses is shown in Figure 4.8.
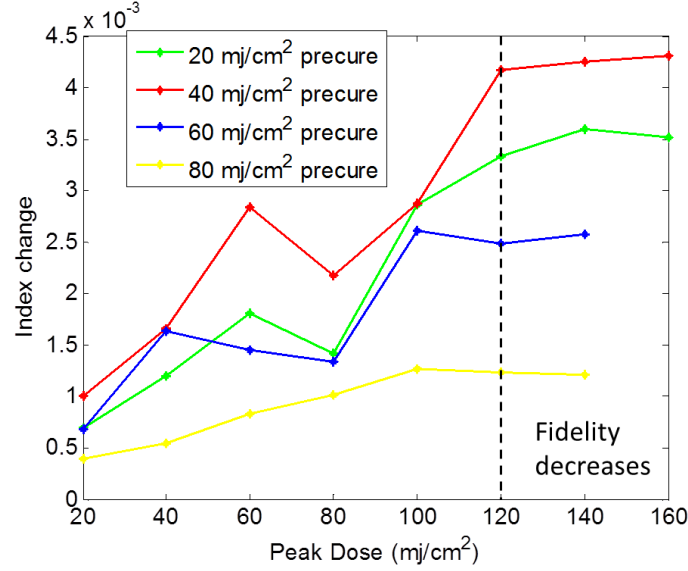
Figure 4.8: The measured index change as a function of pre-cure and patterned peak exposure dose for single layer samples. The pre-cure doses used were 20, 40, 60, and 80 mJ/cm^2.

The largest peak index contrast occurs for a pre-cure dose of 40 mJ/cm^2 and patterned peak exposure dose of 120 mJ/cm^2. As the pre-cure dose increases beyond 40 mJ/cm^2 the potential peak index contrast begins to decrease rapidly as dynamic range of the material decreases. For patterned peak exposure doses beyond 120 mJ/cm^2 the the peak index contrast saturates. Additionally, the fidelity of the parabolic GRIN structure begins to decrease and the index profile begins to resemble Figure 4.6, which is most likely due to overexposure.

4.4.3.3   Development time for a single layer volume

To compare single layer exposures to volumes fabricated with the LDP process, the development time for a single layer volume must be determined. The exposure time for single layer structures is approximately 30 seconds, which is much smaller than the required development time so it can be neglected. To determine the development time of a 125μm thick, single layer structure, the index profile of the parabolic GRIN structure was was quantitatively measured as it developed. The measured index profiles and index contrast as a function of development time are shown in Figure4.9.
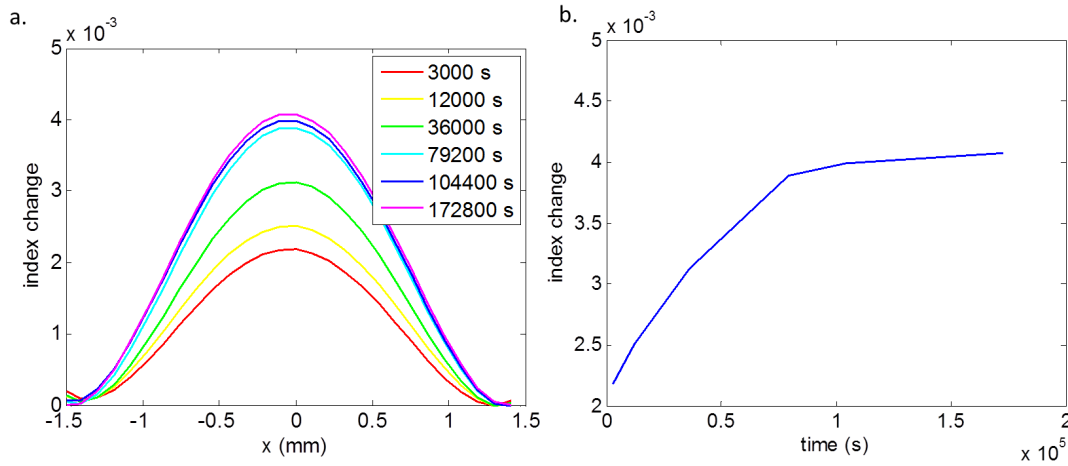
Figure 4.9: Quantitative measurement results of the parabolic GRIN structure with a patterned peak exposure dose of 120 mJ/cm^2 and pre-cure dose of 40 mJ/cm^2. (a) Measured index profile of parabolic GRIN structure at different times during development. (b) Peak index contrast as a function of development time.

Figure 4.9 shows the development time of a 125μm thick, single layer structure is approximately 180,000 seconds. By Fick's law, the diffusion time scales as the layer thickness squared, so for volumes measuring 400μm or thicker the development time would be longer than a month and thus not practical.

4.4.4 LDP fabricated GRIN structures

LDP can fabricate large GRIN structures with higher index contrast and throughput compared to thick, single layer volumes. This is demonstrated by sequentially-writing 25, 5 μm thick layers using the LDP process to fabricate the parabolic GRIN structure. A pre-cure dose of 40 mJ/cm^2 and patterned peak exposure doses of 120 mJ/cm^2 was used for each layer. The index profile of the parabolic GRIN structure is shown in Figure 4.10.
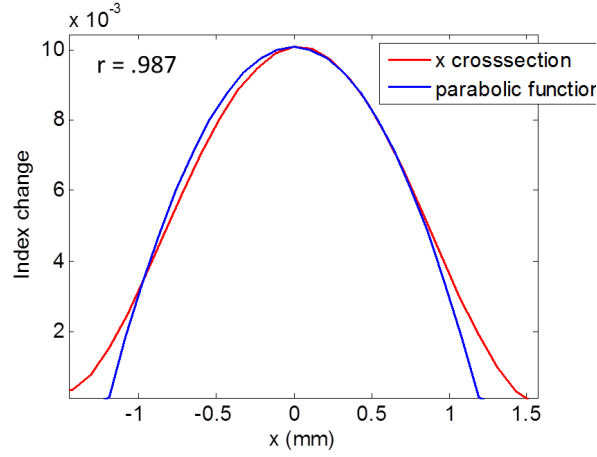
Figure 4.10: Quantitative measurement results of a parabolic GRIN structure fabricated by sequentially-writing 25, 5 μm thick layers, where each layer had a patterned exposure dose of 120 mJ/cm^2 and pre-cure dose of 40 mJ/cm^2. The fabrication was completed in approximately 12,000 seconds. The line plots are a cross section through the center of the measured index profile (red) and the intended parabolic profile (blue). The fabrication time was approximately 12,000 seconds.

Figure 4.10 demonstrates that parabolic GRIN structures fabricated with the LDP process can achieve a higher index contrast and throughput compared to single layer volumes. To achieve higher index contrast, the 5 μm thick layers must enable a greater amount of monomer diffusion compared to 125 μm thick layers. This hypothesis is supported by reference [79], which demonstrates structures with small feature size result in higher index contrast compared to structures with large feature size. The fabrication time is less for LDP compared to a single layer fabrication because 5 μm thick layers reduce total diffusion time.

4.4.5 Comparing LDP to single layer exposures

LDP fabricated volumes have a higher index contrast, higher throughput and more flexibility in the 3D GRIN structure compared to single layer fabrications. The demonstrated index contrast of LDP is 2.4 time greater than single layer fabrications, as shown in previous sections. In single layer volumes the exposure time is insignificant compared to the development time so total fabrication time is equivalent to the development time. By Fick's law, the total development time for single layer volumes scales as volume thickness squared. Conversely, LDP fabricated volumes the total fabrication times scales linearly with volume thickness, making the fabrication time of thick fabrications orders of magnitude smaller compared to single layer volumes. Table 4.4.5 compares the parabolic GRIN structures fabricated with LDP to the single layer volumes, demonstrating LDP's superior index contrast and throughput.

Table 4.1: Quantitative comparison between volumes fabricated with multiple layers using LDP and single layer volumes

Parameter	LDP (5 μm layers)	Single layer
Peak index contrast	0.01	0.0045
Fabrication time (125μm)	3.5 hours	50 hours
Fabrication time (2 mm)	53 hours	1.45 years
Pearson correlation coeff.	0.983	0.978
3D GRIN	yes	no

4.4.6 Conclusion

In this section, LDP has shown it has the ability to fabricate high fidelity parabolic GRIN structures within a volume. To fabricate a parabolic GRIN lenses with a diameter of 2.5 mm with LDP, the volume thickness will have to significantly increase to create a GRIN

lens with significant optical power. The focal length of a parabolic GRIN lens is

$$f = \frac{1}{(n_0 + \Delta n)\sqrt{A}sin(t\sqrt{A})} \qquad (4.2)$$

where n_0 is the refractive index of unstructured polymer, Δn is the peak index change, t is the thickness of the volume and A is the gradient constant. The thickness of a lens for a given focal length is

$$t = \frac{1}{\sqrt{2A}}sin^{-1}(\frac{1}{(n_0 + \Delta n)\sqrt{2A}f} \qquad (4.3)$$

The peak refractive index change is 0.01 for LDP fabricated GRIN lenses, so the gradient constant is 0.004 $(1/mm^2)$. To fabricate a GRIN with a focal length of 50 mm the thickness of the GRIN lens is

$$t = \frac{1}{\sqrt{0.008}}sin^{-1}(\frac{1}{(1.47)\sqrt{0.008}50} = 1.48mm \qquad (4.4)$$

The total fabrication time for LDP to fabricate this lens would ne approximately 40 hours.

4.5   Arbitrary Gradient Index Structuring

Arbitrary GRIN structuring using the LDP process is demonstrated by the fabrication of the first 10 Zernike polynomials as refractive index structures within a volume of photopolymer. Zernike polynomials are a sequence of polynomials that are orthogonal on the unit disk and used throughout optics as the basis set to describe wavefronts of optical systems. In particular, they are used to characterize higher-order errors observed in interferometric analyses, and are also commonly used in adaptive optics where they are used to cancel out distortions of optical systems and objects [159, 160]. Zernike polynomials are a complete orthogonal basis set, so there are an infinite number of functions, however for most applications the first 10 polynomials are used. The first 10 Zernike polynomials are shown in Figure 4.11.

In order to fabricate the Zernike polynomials as index structures within a volume, the phase of each zernike polynomial must be mapped onto an 8 bit bitmap with the same
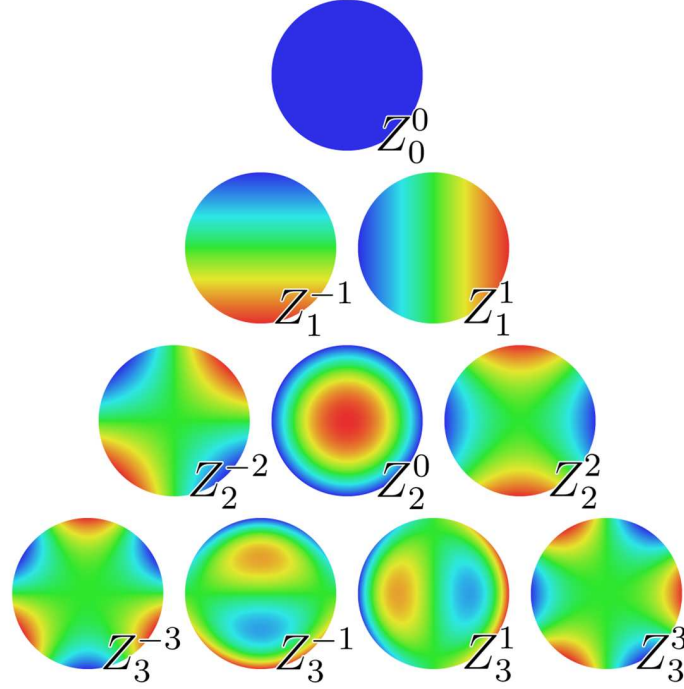
Figure 4.11: The first 10 Zernike polynomials. The color quantifies the amount of phase delay in the wavefront, where blue represents -π and red represents π.

dimensions as the DMD. The DMD uses the bitmap to varying the exposure dose at each pixel. To represent -π phase the pixel value was set to 0, corresponding to no exposure dose time, and for phase value of π the was set to 255, corresponding to the maximum amount of exposure dose the optical system can deliver. Figure 4.12 shows the bitmaps used in the experiments.

The 125 μm thick layers were exposed with exposure parameters found in the previous section for high index contrast and fidelity. The quantitatively measured index profiles of the Zernike polynomials fabricated by the LDP process are shown in Figure 4.13.

Figure 4.13 demonstrates that LDP can fabricate nearly arbitrary refractive index structures with high recording fidelity. The measured index profiles shown in Figure 4.13 demonstrate a high degree of correlation to the intended pattern. The Pearson correlation coefficients for each pattern shown in Figure 4.13 was determined by comparing a 1D cross-
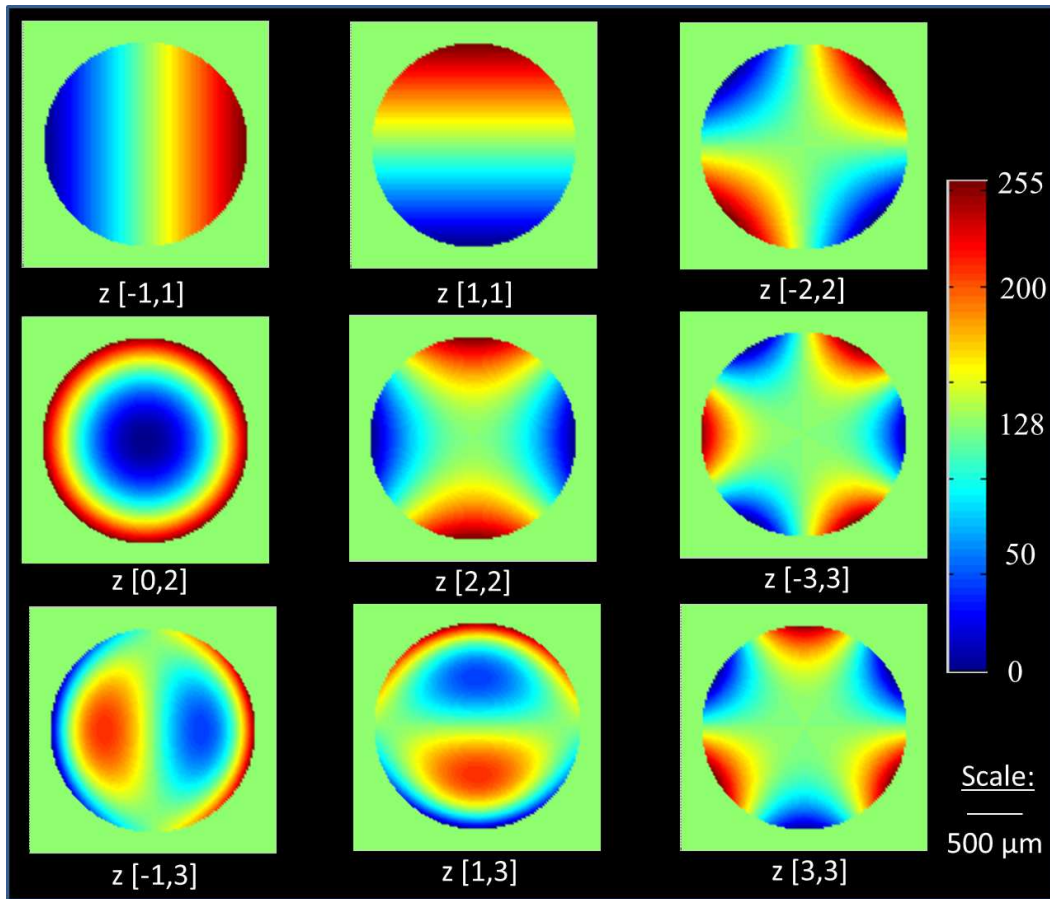
Figure 4.12: The bitmaps used to expose each Zernike polynomial in a single layer of a volume fabricated by LDP. The bitmaps vary in value from 0 to 255, where 0 corresponds to no exposure dose and 255 corresponds to the maximum amount of exposure dose the optical system can deliver.

section of the fabricated and intended index structure for each volume.

The results demonstrate that the LDP process can create phase masks with superimposed Zernike polynomials to reduce or eliminate aberrations in a optical system. These potential phase masks would have the ability to correct aberrations of optical systems. For example, in the fields of optometry and ophthalmology, wavefront aberrations in the eye can be measured with a wavefront sensor [161] and described by a set of Zernike polynomials. The measured wavefront aberrations in the eye can be compensated for by a phase plate fabricated with LDP with the proper superimposed Zernike polynomials.
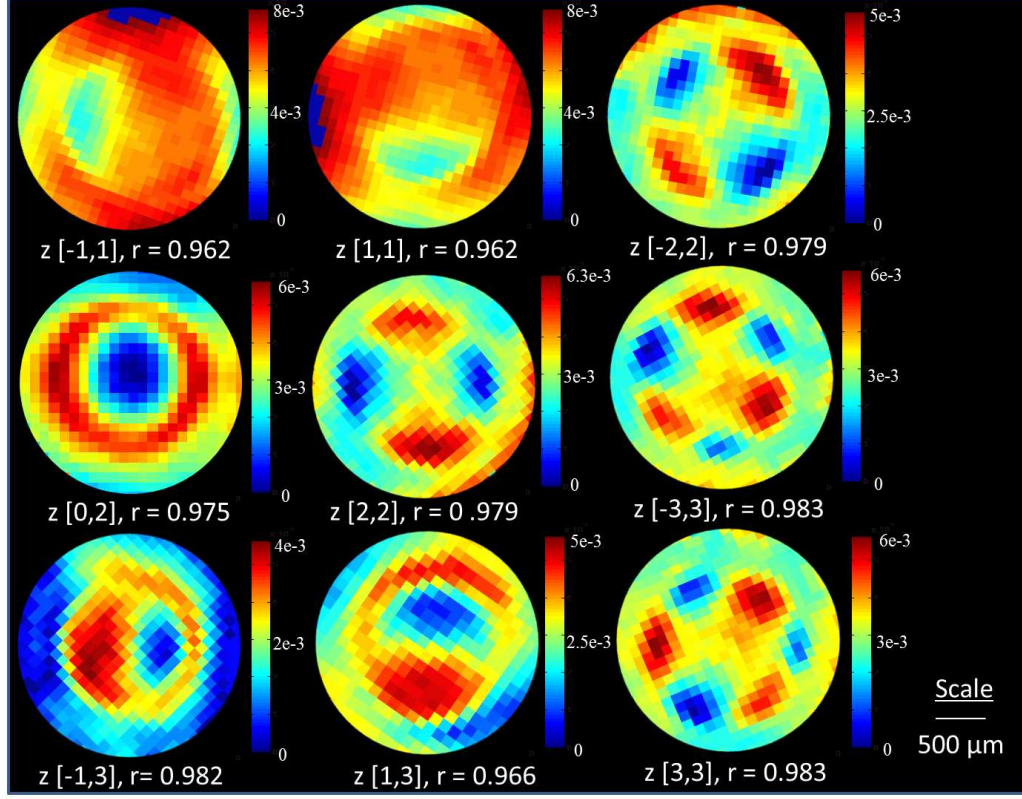
Figure 4.13: Measured index profiles of the Zernike polynomials fabricated by the LDP process. Pre-cure doses of 40 mJ/cm^2 and patterned peak exposure doses of 120 mJ/cm^2 were used for the fabrication of each volume.

4.6   Summary and conclusion

In summary, the LDP process enables efficient production of GRIN structures with arbitrary index profiles not limited transverse diffusional distances. The process of longitudinal monomer diffusion allows the fabrication of millimeter scale GRIN structures, demonstrated by single and 25 layer fabrications. To ensure a high fidelity GRIN recording of each layer, a pre-cure exposure is required before the patterned exposure. The fabrication of 125 μm thick parabolic GRIN structures demonstrated the LDP process has a higher throughput and index contrast compared to single layer fabrications. For transverse structures measuring over 2 millimeters in diameter and 2 millimeters in depth, LDP enables fabrications two orders of

magnitude faster than single layer exposures. The index contrast was also demonstrated to be twice as large for LDP fabricated structures. The exposure conditions and process steps determined in this chapter can be applied to the fabrication of GRIN lenses.

LDP's ability to create high fidelity, nearly arbitrary GRIN structures was demonstrated by the fabrication of 125 μm thick volumes containing index structures with 10 different Zernike polynomials. The index contrast and fabrication rate of LDP potentially enable the fabrication of large scale, nearly arbitrary 3D refractive index devices and phase structures. The next chapter presents a thorough study of the oxygen dynamics of the chamber window.

Chapter 5

Study of the Chamber Window

5.1   Introduction

In the previous chapters, I have demonstrated LDP's ability to fabricate millimeter scale polymer volumes that contain encapsulated three dimensional binary and gradient index structures. The fabrication of these encapsulated 3D index structures is enabled by the use of the chamber window, a flat, 125 μm thick PDMS layer adhered to a piece of cover glass.

The chamber window enables the LDP process by performing four functions: allowing optical pattern access to the material, preventing polymer adhesion to the window, passively planarizing new layers and maintaining a monomer-rich liquid layer next to the exposed volume. Optical clarity of the window minimizes aberrations of the optical pattern, allowing multiple independent layers to be written in the volume with high recording fidelity. Preventing polymer adhesion to the window allows multiple independent layers to be written on top of one another to create the volume. Each new layer to be structured is automatically planarized by the flat PDMS surface. The monomer rich liquid layer next to the exposed part, enables longitudinal diffusion, which significantly decreases fabrication time for large transverse structures and increase fidelity and index contrast.

All of these functions are made possible by the inhibition of free radical polymerization at the casted PDMS coating on the cover glass. This inhibition is caused by oxygen within the PDMS diffusing to the liquid photopolymer [91]. The permeability of PDMS to oxygen

is well-known and has previously been exploited to grow cells for biological applications [162, 163] achieve gas separations through PDMS membranes [164, 165] and fabricate micron sized particles within microfluidic devices [166]. In implementations that used PDMS microfluidic devices, such as the fabrication of micron sized particles, the oxygen consumed during the reaction is replenished by oxygen that constantly diffuses through the PDMS. However, this can not be how the chamber window used in the LDP process functions, because the opposite side of the PDMS is adhered to glass, which prevents oxygen in the air from diffusing into the PDMS. Still, the LDP process is able to sequentially write over 100 layers without polymer adhering to the chamber window, so oxygen must be replenished within the PDMS through a different mechanism. This motivates a detailed study of the oxygen dynamics in the LDP process to understand and optimize the exposure conditions that guarantee adhesion-free operation.

In this chapter, a reaction/diffusion model is presented to predict the spatial and temporal variation in the concentration of oxygen and unconverted monomer as sequential layers are fabricated within LDP. From the simulation results, the longevity of the chamber windows and the amount of polymer adhesion for a given exposure can be inferred. The simulation results are validated experimentally by a test stand for uniform exposures that incorporated a strain gauge into the LDP mechanical design. The test stand is referred to as the pull tester and quantifies the polymer adhesion for each layer. The pull tester determines polymer adhesion to the window by measuring the force as the polymer volume is pulled away from the chamber window. The simulation and experimental results are then used to optimize the LDP process.

5.2   Reaction/Diffusion simulation of the chamber window

To gain a understanding of how the oxygen concentration within the PDMS layer of the chamber window effects the inhibition and polymerization dynamics, the reaction/diffusion simulation presented in Chapter 2 was extended to include the PDMS layer in the simu-

lation. In the previous implementation of the reaction/diffusion simulation the chamber window/monomer interface was considered an external boundary of the numerical simulation volume and a Dirichlet boundary condition was implemented for the concentration of molecular oxygen. Here, the concentration was assumed to be constant throughout, not only for the exposure of a single layer, but for the fabrication of the entire volume.

The simplified reaction/diffusion model implemented here only considers the photolysis, chain initiation, chain propagation, chain termination and oxygen inhibition processes [91, 103]. However, in the implementation presented in this chapter the quasi-steady state approximation is not used and the concentration of photoinitiator and radicals are calculated for each time step of the simulation.

5.2.1 Exposure geometry

The experimental and simulation geometry is illustrated in Figure 5.1. A 1D model is considered which is adequate when longitudinal dominates transverse diffusion, which is the case for most LDP exposures. To experimentally accommodate this simplification, unstructured light 4 millimeters in diameter is used for all experiments.

5.2.2 Reaction/Diffusion model of the PDMS layer

In the previous implementation of the reaction/diffusion simulation, I assumed the oxygen concentration within the PDMS remained at its atmospheric equilibrium concentration throughout the exposure. However, this is not an accurate representation of the system when multiple layers are fabricated and the oxygen concentration may be significantly depleted in the PDMS. Therefore, in this reaction/diffusion simulation the concentration of oxygen in the PDMS is accounted for in the model. Since there are no photo-generated reactions within the PDMS, only the process of oxygen diffusion is considered and can be described by

$$\frac{\delta[O_{2,\text{PDMS}}]}{\delta t} = D_{o,\text{PDMS}} \frac{\delta^2[O_{2,\text{PDMS}}]}{\delta z^2} \tag{5.1}$$
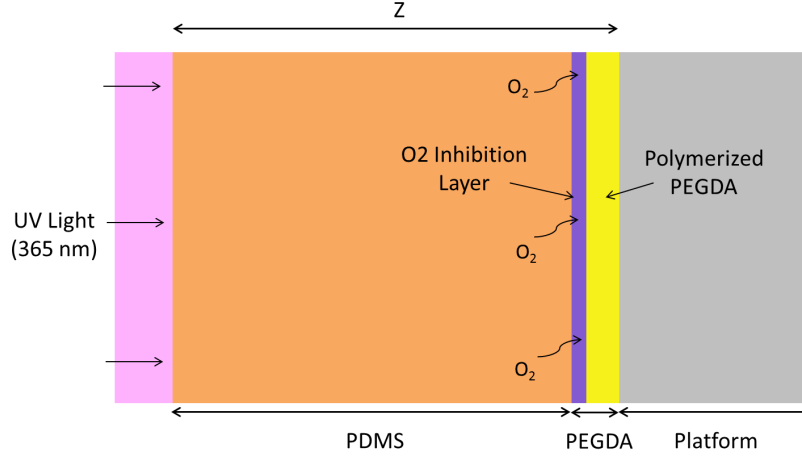
Figure 5.1: Experimental and stimulation geometry. Illustration of thin layers of polymer being formed using LDP. Unstructured UV light is projected from the left to form thin layer of PEGDA adhered to a platform. The polymer layer is separated from the PDMS by a thin oxygen inhibition layer consisting of un-gelled PEGDA. The thickness of the PDMS is 125 μm and the thickness of the PEGDA layer is 15μm.

where $D_{o,\text{PDMS}}$ is the diffusion coefficient of oxygen in PDMS and z is the spatial variable. The concentration of oxygen in PDMS is depleted by diffusion from the PDMS to PEGDA. This depletion is the result of photo-generated radicals consuming molecular oxygen in PEGDA, creating a concentration gradient that drives the oxygen diffusion from the PDMS.

5.2.3   Reaction/Diffusion rate expressions in PEGDA

In this section a model of the photo-chemical processes in PEGDA is introduced. To initiate the photo-chemical processes in PEGDA, UV light incident on the sample photolyzes the initiator molecules (pi) to produce primary radical species (r') through a photo-cleavage process. The rate of radical production in a thin layer of material is proportional to the rate at which incident photons are absorbed in that layer. In a layer of thickness dz at a depth z the rate of radical production, r' is given by

$$r' = 2\phi\epsilon[pi]\frac{\delta I(z)}{\delta z} \tag{5.2}$$

where $[pi]$, ϵ and ϕ are the concentration, molar absorptivity, and quantum yield of the photoinitiator respectively, and $I(z)$ is the light intensity. The light intensity varies through the depth of the material in accordance with Beer's law and is given by

$$\frac{\delta I(z)}{\delta z} = -\epsilon[pi]I(z) \tag{5.3}$$

However, the the layer is optically thin so the absorption can be ignored and set equal to the incident intensity I_0. The radical production is therefore

$$r' = 2\phi\epsilon I_0[pi] \tag{5.4}$$

The concentration of the photo-generated radical species is controlled by the termination processes. In this model, only bi-molecular and unimolecular termination are considered. Other modes of termination, such as the trapping of radical species are neglected. the model does not distinguish between primary and propagating radicals, so consumption of monomer does not change the radical density. The radical density in the material is then given by

$$\frac{\delta r'}{\delta t} = 2\phi\epsilon[pi]I_0 - k_t[r']^2 - k_o[r'][O_2] \tag{5.5}$$

where k_t is the bimolecular termination rate constant and k_o is the unimolecular termination rate constant. The diffusion of initiator and radicals species are not considered in the model. Although both the initiator and radicals species are small, strong concentration gradients will not develop within the modeled layer because the thickness of the layer is nearly two orders of magnitude smaller than the absorption depth and diffusion rate is proportional to spatial scale squared.

The density of oxygen is controlled by the termination and diffusion processes. The diffusion of oxygen is included in the model because it is critical to the LDP process and the constant flux of oxygen from the PDMS layer creates strong concentration gradients that drive diffusion. Additionally, the size of molecular oxygen is small compared to the other chemical species modeled and thus its diffusivity is larger, potentially creating rapid changes

in other reaction processes. The oxygen transport and consumption is described by

$$\frac{\delta[O_{2,\text{PEGDA}}]}{\delta t} = D_{o,\text{PEGDA}} \frac{\delta^2[O_{2,\text{PEGDA}}]}{\delta z^2} - k_o[r'][O_{2,\text{PEGDA}}] \tag{5.6}$$

where $D_{o,\text{PEGDA}}$ is the diffusion coefficient of oxygen in PEGDA and $[O_{2,\text{PEGDA}}]$ is the concentration of oxygen in PEGDA.

The density of monomer and polymer are controlled by the polymerization rate and radical density in the layer. Monomer is consumed when it reacts with a radical. The concentration of monomer is then given by

$$\frac{\delta[m]}{\delta t} = -k_p[m][r'] \tag{5.7}$$

where k_p is the polymerization rate constant. When a monomer molecule is consumed in the chain propagation step it is directly converted to polymer, so the production of polymer is equivalent to the monomer consumption. The concentration of polymer is then given by

$$\frac{\delta[p]}{\delta t} = k_p[m][r'] \tag{5.8}$$

The process of monomer diffusion is not included in the model because it should not effect the function of the chamber window. While the diffusion constant of monomer in the partially-converted PEGDA solution is unknown, a numerical study found that the results were not changed by monomer diffusion until the monomer diffusion coefficient was nearly equal to the oxygen diffusion coefficient. Since this is unreasonable given the ratio of their molecular weights, I conclude that monomer diffusion can safely be ignored.

5.2.4   Non-dimensional equations

The parameters and constants from the equations in the previous section were appropriately scaled to create non-dimensional equations using the following relationships

$$t' = \frac{tD_{02,\text{PDMS}}}{Z^2}, \quad z' = \frac{z}{Z}, \quad \Omega = \frac{\phi\epsilon I_0 Z^2}{D_{02,\text{PDMS}}}, \quad \gamma = \frac{D_{02,\text{PEGDA}}}{D_{02,\text{PDMS}}},$$

$$\zeta = \frac{2k_t Z^2 [pi_0]}{D_{02,\text{PDMS}}}, \quad \chi = \frac{k_o Z^2 [O_{2,\text{PEGDA}}]^*}{D_{02,\text{PDMS}}}, \quad \rho = \frac{2k_o Z^2 [pi_0]}{D_{02,\text{PDMS}}}, \quad \kappa = \frac{2k_p Z^2 [pi_0]}{D_{02,\text{PDMS}}}$$

where Z is the total simulation thickness and $[O_{2,\text{PEGDA}}]^*$ is the equilibrium concentration of oxygen in PEGDA. Time is normalized to the diffusion time of oxygen across the exposure geometry. Space is normalized to the thickness of the exposure geometry. γ is the ratio of oxygen diffusivity in PEGDA to that in PDMS. The concentration of the chemical components were normalized to either their initial concentrations or in the case of the radical and polymer concentration the maximum possible concentration using the following relationships

$$[PI] = \frac{[pi]}{[pi_0]}, \quad [R'] = \frac{r'}{2[pi_0]}, \quad [M] = \frac{m}{[m_0]},$$

$$[P] = \frac{p}{[m_0]}, \quad [\theta_{\text{PDMS}}] = \frac{[O_{2,\text{PDMS}}]}{[O_{2,\text{PDMS}}]^*}, \quad [\theta_{\text{PEGDA}}] = \frac{[O_{2,\text{PEGDA}}]}{[O_{2,\text{PEGDA}}]^*},$$

where $[O_{2,\text{PDMS}}]^*$ is the equilibrium concentration of oxygen in PDMS, $[m_0]$ is the initial concentration of monomer and $[pi_0]$ is the initial concentration of photoinitiator. with these definitions, the equations become

$$\frac{\delta[PI]}{\delta t'} = -\Omega[PI] \tag{5.9}$$

$$\frac{\delta[R']}{\delta t'} = \Omega[PI] - \zeta[R']^2 - \chi[R'][O_2] \tag{5.10}$$

$$\frac{\delta[\theta_{\text{PEGDA}}]}{\delta t'} = \gamma \frac{\delta^2[\theta_{\text{PEGDA}}]}{\delta z'^2} - \rho[R'][\theta_{\text{PEGDA}}] \tag{5.11}$$

$$\frac{\delta[M]}{\delta t'} = -\kappa[R'][M] \tag{5.12}$$

$$\frac{\delta[P]}{\delta t'} = \kappa[R'][M] \tag{5.13}$$

and the non-dimensional equation that describes the oxygen concentration in PDMS is

$$\frac{\delta[\theta_{\text{PDMS}}]}{\delta t'} = \frac{\delta^2[\theta_{\text{PDMS}}]}{\delta z'^2} \tag{5.14}$$

These equations are discretized and time advanced using the ODE15s function in Matlab. The ODE15s function is an ordinary differential equation solver that uses a 5th order implicit scheme to solve stiff problems such as this one. The ODE15s function reduces

processing time while limiting numerical error by estimating error at each time step and adjusting the next time step to be as large as possible while staying within a specified error tolerance.

5.2.5 Initial conditions

The initial conditions for the chemical concentration arise from the assumption that PDMS and PEGDA contain their equilibrium concentration of oxygen at t = 0. The initial conditions for oxygen in PDMS is

$$0 \leq z < \text{interface} : [\theta_{\text{PDMS}}](z, 0) = 1 \tag{5.15}$$

The initial conditions for chemicals concentrations in PEGDA are

$$
\begin{aligned}
\text{interface} < z \leq Z : [\theta_{\text{PEGDA}}](z, 0) &= 1 \\
[PI](z, 0) &= 1 \\
[R'](z, 0) &= 0 \\
[M](z, 0) &= 1 \\
[P](z, 0) &= 0
\end{aligned}
$$

$$\tag{5.16}$$

5.2.6 External boundary conditions

There are two external boundaries in the simulation, one at the edge of the PDMS/glass interface within the chamber window and the other at the liquid photopolymer/platform interface. In both cases these are hard boundaries, so a Neumann boundary condition is imposed at both of them. A Neumann boundary condition defines the flux across the boundary to be zero for every chemical species. So the PDMS/glass interface boundary, the boundary condition is

$$\frac{\delta[\theta_{\text{PDMS}}]}{\delta z'} = 0 \tag{5.17}$$

and at the liquid photopolymer/platform boundary, the boundary condition is

$$\frac{\delta[\theta_{PEGDA}]}{\delta z'} = 0 \tag{5.18}$$

All other species in the simulation do not diffuse, so the flux of those species is already zero at the boundary. Unlike Dirichlet boundary conditions, Neumann boundary conditions restrict additional species from entering the bounds of the simulation and therefore are meant for closed systems such as this one.

5.2.7   Internal boundary conditions

A final internal boundary condition is required to account for the presence of the interface between PDMS and PEGDA. The partitioning equilibrium of oxygen between PEGDA and PDMS can be represented as

$$[O_{2,\text{PDMS}}] \underset{k_2}{\overset{k_1}{\rightleftharpoons}} [O_{2,\text{PEGDA}}] \tag{5.19}$$

where k_1 and k_2 are the first-order interfacial rate constants of oxygen from PEGDA and PDMS, respectively. When the concentration of oxygen at the interface is at dynamic equilibrium, there is zero net flux of oxygen across the interface and this process can be described by the following equation

$$\frac{k_1}{k_2} = \frac{[O_{2,\text{PEGDA}}]^*}{[O_{2,\text{PDMS}}]^*} = K_p \tag{5.20}$$

where K_p is the distribution coefficient of oxygen between PEGDA and PDMS. The interfacial equilibrium is perturbed when photo-generated radical species deplete oxygen from PEGDA during an exposure, inducing the transfer of oxygen across the interface from PDMS to PEGDA. The flux of oxygen across the interface is governed by both the interfacial kinetics and the rates of mass transfer in each material [167]. As the system attempts to reestablish equilibrium following the depletion of oxygen in PEGDA, the diffusive flux of oxygen across the interface is

$$D_{o,\text{PDMS}}\frac{\delta[O_{2,\text{PDMS}}]}{\delta z} = D_{o_2,\text{PEGDA}}\frac{\delta[O_{2,\text{PEGDA}}]}{\delta z} = k_1[O_{2,\text{PDMS}}] - k_2[O_{2,\text{PEGDA}}] \tag{5.21}$$

The internal boundary condition, shown above, couples the time dependent diffusion equations described in the previous section and enables diffusion between the two materials.

Determining the correct values for the coefficient, concentrations and rates described above is important to ensure accurate simulation results. The precise value of the diffusion coefficient of oxygen in PDMS is not consistent in the literature, and the value reported varies from 520 to 3400 μm^2/s [168, 169]. This value was initially set to an averaged value from the values found in the literature, and then varied within the reported range to determine the effect, if any, it has on the results of the simulation.

In order to accurately model the interfacial kinetics between PDMS and PEGDA, the interfacial rate constants for the materials must be known. To gain a greater understanding of the interfacial kinetics in multiple phase systems, scanning electrochemical microscopy techniques have been used with numerous materials including PDMS [167, 170]. However the interfacial rate constant of oxygen flowing from PDMS to PEGDA has not been reported in literature. The interfacial rate constant of oxygen flowing from PDMS to water has experimentally been determined to be 0.01 m/s [167]. A comparison of viscosity indicates the interfacial rate constant of oxygen from PDMS to PEGDA should be approximately 50 times smaller than the interfacial rate constant of oxygen flowing from PDMS to water. Therefore in the simulation I estimated the interfacial rate constant for oxygen flowing from PDMS to PEGDA to be 0.0002 m/s. and find qualitative and reasonable quantitative agreement with experiment. However, more precise modeling will require direct measurement of this quantity.

5.2.8   Model parameters

.

Polyethylene (glycol) diacrylate (PEGDA) with molecular weight of 575 Daltons was used as the model material system to understand chamber window behavior. PEGDA is used as the model material system because the rate constants are known in the literature and it is

the material system used in the experimental section of the chapter. Irgacure 651 was used as the photoinitiator, with a concentration of 1% w/w in both the simulation and experiment. Typical values of rates and constants for PEGDA, PDMS, and the photoinitiator are shown in Table 5.2.8.

Table 5.1: Reaction rates, diffusion constants and chemical concentrations used in the reaction/diffusion simulation

Parameter	Value	Units	Source
k_p	25	$\frac{m^3}{mols}$	[106]
k_t	2520	$\frac{m^3}{mols}$	[106]
k_O	5 x 10^5	$\frac{m^3}{mols}$	[91]
$D_{o,\text{PEGDA}}$	28.4	$\frac{\mu m^2}{s}$	[105]
$D_{o,\text{PDMS}}$	1500	$\frac{\mu m^2}{s}$	[168, 169]
I_0	6 x 10^{-4}	$\frac{E}{m^2 s}$	measured
ϵ	40	$\frac{m^3}{mols)}$	[107]
ϕ	.6	–	[109]
$[O_{2,\text{PEGDA}}]^*$	1.5	$\frac{mol}{m^3}$	[108]
$[O_{2,\text{PDMS}}]^*$	2	$\frac{mol}{m^3}$	[171]
k_1	.0002	$\frac{m}{s}$	estimated from [167]
k_2	.000266	$\frac{m}{s}$	estimated from [167]
K_p	.75	–	[171],
exposure time	10	$\frac{s}{layer}$	set by experiment
layer thickness	10	μm	set by experiment

In the numerical simulation, it is assumed that the parameters of the model shown here are invariant with changes in monomer conversion. However, this basic assumption does not hold for the high monomer conversion regime, where anomalous behavior can occur [172]. This behavior includes autoacceleration and autodeceleration [173], incomplete functional group conversion [174] and radical trapping [175]. These processes result in a reduction in the mobility of reacting species in the cross-linked polymer network. The reduction in the mobility of reacting species results in a reduction of the diffusion coefficient, D_o, and a change in the polymerization (k_p) and termination (k_t and k_o) rates.

Additionally, the reduction in monomer mobility as a function of conversion results in a gradient in the oxygen diffusion coefficient as function of monomer conversion. The gradient in the oxygen diffusion coefficient results in a reduction of the thickness of the transition between the inhibited and high conversion regions because diffusion of oxygen can no longer broaden the transition region. This was confirmed by a numerical study, which demonstrated that the transition thickness decreased as the oxygen diffusion coefficient was decreased within the simulation, as shown in Figure 5.2. A conversion variant reduction in the oxygen diffusion coefficient reduces the thickness of the transition region, defined as the thickness required to increase polymer conversion from 20% to 80%, by a factor of approximately two. A conversion invariant reduction in the oxygen diffusion coefficient reduces the thickness of the transition region by a factor of approximately four, suggesting materials with higher viscosities than PEGDA, where oxygen mobility is smaller, could result in better axial resolution.

Another discrepancy between a physical system and the numerical simulation is the simulation results show high monomer conversion (100%) in the polymerized regions. However, this is also not likely due to the processes of autodeceleration, incomplete functional group conversion and radical trapping which increase the termination (k_t and k_o) rates in the high conversion regime. These effects usually limit conversion to less than 100%.

Additionally, the effect oxygen has on polymerization depends strongly on the type of
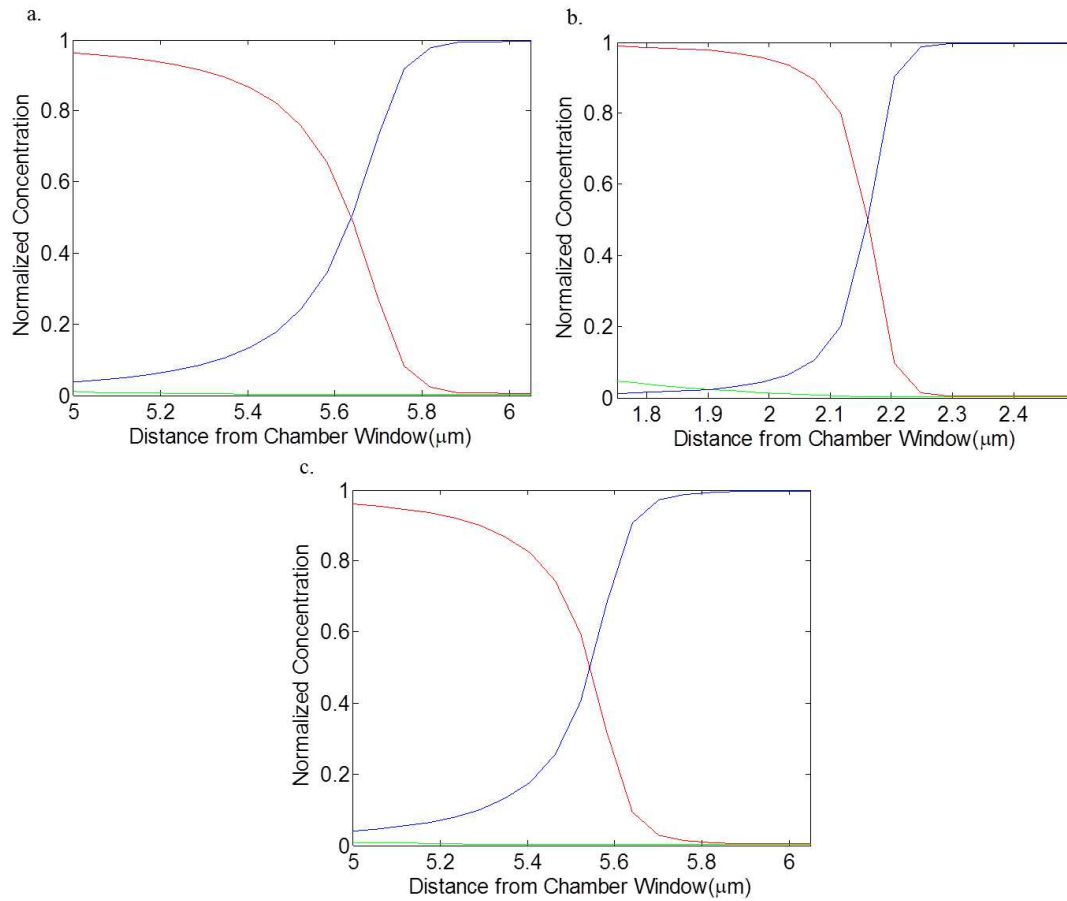
Figure 5.2: The concentration of monomer (red), oxygen (green), and polymer (blue) with different oxygen diffusion coefficients. (a) The oxygen diffusion coefficient is $28.4\mu\mathrm{m}^2/\mathrm{s}$ with no dependence on polymer concentration. (b) The oxygen diffusion coefficient is $2.84\mu\mathrm{m}^2/\mathrm{s}$ with no dependence on polymer concentration. (c) The oxygen diffusion coefficient varies from $28.4\mu\mathrm{m}^2/\mathrm{s}$ to $2.84\mu\mathrm{m}^2/\mathrm{s}$ as a linear function of polymer concentration. Where complete conversion corresponds to an oxygen diffusion coefficient of $2.84\mu\mathrm{m}^2/\mathrm{s}$ and no conversion corresponds to an oxygen diffusion coefficient of $28.4\mu\mathrm{m}^2/\mathrm{s}$.

monomer used. Both the monomer reactivity, which governs the cure speed and reaction time, and the monomer's viscosity, which determines the speed at which oxygen diffuses into the monomer can change the behavior of the chamber window [176]. The results presented here are thus expected to be qualitatively correct even for different monomers, but the quantitative performance (e.g. layer thickness) will vary with reactivity and diffusion rate.

5.3   Simulation results

The differential equations were integrated in time to find the depth dependence of all modeled chemical species. Figure 5.3 shows the oxygen, monomer and polymer as a function of depth in PDMS and PEGDA after a single layer is exposed.
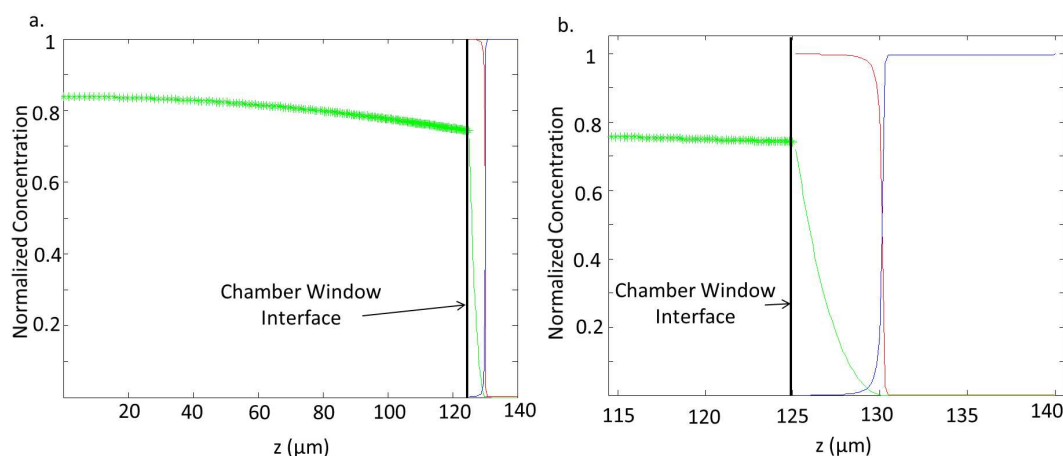
Figure 5.3: Chemical species as a function of depth after a single layer is exposed. (a) The concentrations of monomer (red), oxygen (green) and polymer (blue) through PEGDA and PDMS after a single layer is written. (b) Magnified image of (a) showing the concentration of monomer, oxygen and polymer at the chamber window/PEGDA interface. The concentration of the chemical species as a function of depth are different than the simulation results shown in Figure 2.13 because different exposure parameters were modeled.

The simulation shown in Figure 5.3 demonstrate the fundamental performance of the chamber window, indicating that diffusion of oxygen from the PDMS maintains an inhibited, liquid layer directly adjacent to the PDMS layer. In addition to confirming the chamber window performance, the simulation results also quantifies how much the oxygen concentration in the PDMS has been depleted from its atmospheric equilibrium concentration after only a single layer is fabricated. If the quantity of oxygen depleted is the same for each exposed layer, then it will be completely exhausted after only four layers.

To determine the oxygen concentration in PDMS as additional layers are fabricated, the model was extended to twenty layers. To model the creation of a new layer, positions on the

spatial grid with a polymer concentration larger than the gel point of PEGDA were replaced with initial concentrations of oxygen, monomer and photoinitiator. The concentration of oxygen was left unchanged at positions in space where the polymer concentration was less than the gel point. The oxygen concentration in the PDMS as a function of depth and layer number is shown in Figure 5.4.
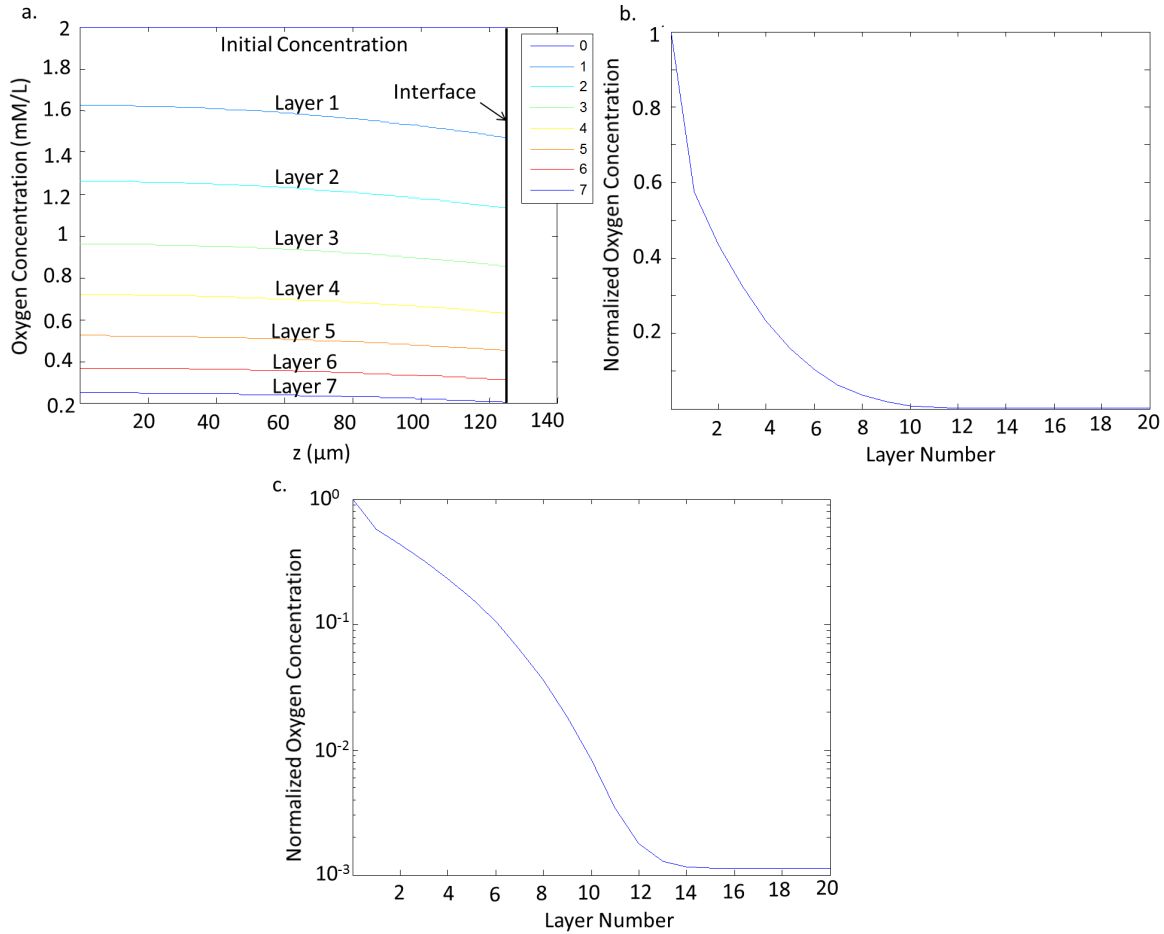
Figure 5.4: Oxygen concentration in the PDMS of the chamber windows as a function of space and layer number. (a) The oxygen concentration in the PDMS as a function of depth for the first 7 layers written. (b) Plot of the total oxygen concentration in the PDMS as a function of layer number. (c) Semi-log plot of the oxygen concentration in the PDMS as a function of layer number.

The simulation results show that if the LDP process is run continuously, the oxygen

concentration in PDMS will approximately exponentially decrease as a function of each layer written until it is depleted. Surprisingly, the oxygen concentration reaches a steady state at approximately 0.1% of its equilibrium concentration by the fourteenth layer. This effect is most likely due to oxygen diffusion from PEGDA and its atmospheric equilibrium concentration of oxygen into the PDMS, when the oxygen concentration in PDMS becomes significantly depleted. Oxygen is able to rapidly diffuse from PEGDA to PDMS at the beginning of an exposure when there is large concentration gradient of oxygen at the PDMS interface. The reduction in oxygen concentration within the PDMS as additional layers are written will reduce the thickness of the oxygen inhibition layer, demonstrated by Figure 5.5.
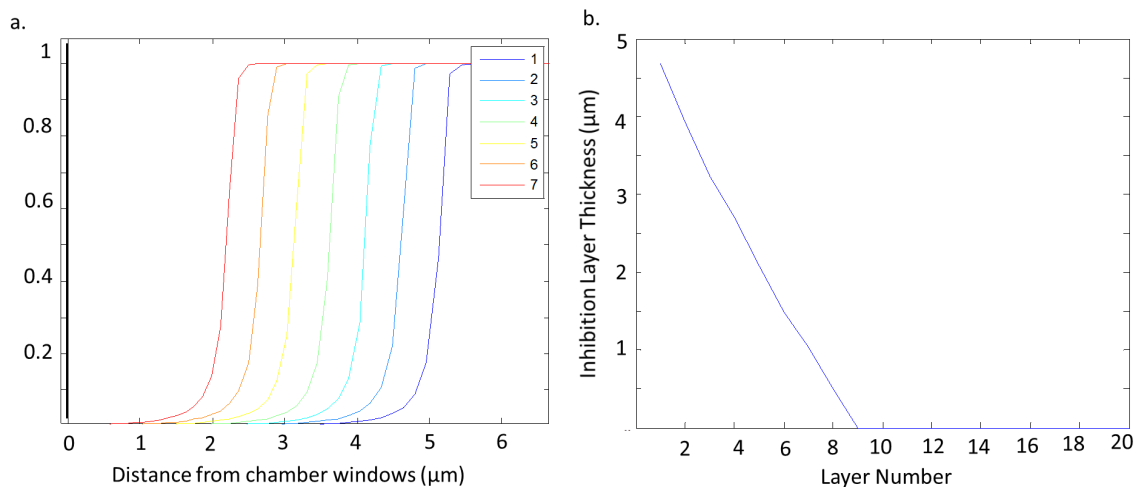
Figure 5.5: Oxygen inhibition layer thickness as a function of layer number. (a) The normalized conversion of polymer as a function of distance away from chamber window interface for the first 7 layers written. (b) Oxygen inhibition layer thickness as a function of layer number for the first 20 layers written. The thickness of the oxygen inhibition layer is defined as the distance from the PDMS/PEGDA interface to the first instance where the normalized polymer concentration is 0.02.

The simulation results shown in Figure 5.5 demonstrate that as more layers are written the oxygen inhibition layer created by the chamber window decreases with each layer written until it disappears entirely. This implies that the LDP process has lost the ability to control thickness of individual layers, because the oxygen inhibition layer is changing so layer

thickness no longer is equivalent to the stage motion. Figure 5.5b shows during the fabrication of the first 10 layers, the thickness of the inhibited layer decreases approximately 500 nm for each layer written. The reduction of the oxygen inhibition layer thickness increases the exposed layer thickness for each layer, changing the thickness of the written refractive index structures thus reducing fidelity of the fabricated volume. In addition to reduction in fidelity, after 10 layers are sequentially written, the oxygen inhibition layer completely disappears and the material begins to polymerize to the chamber window. The degree of polymerization of the material to the chamber window as a function of layers fabricated is shown in Figure 5.6. While the amount cross-linking and penetration of gelled PEGDA is not known, conversion right at the chamber window surface is an indication of failure.
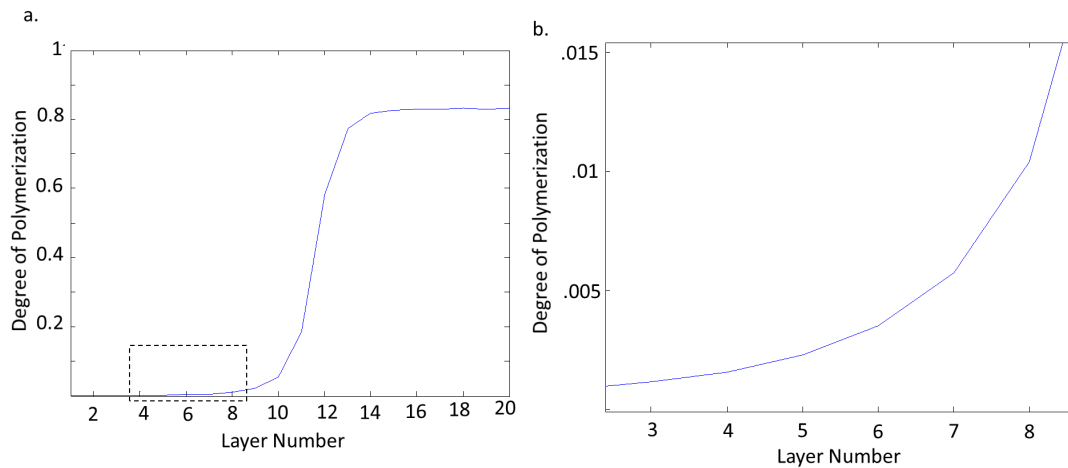
Figure 5.6: (a) Degree of polymerization on the chamber window as a function of layer thickness. (b) Magnified image of where there is potentially enough polymerization on the chamber window to cause adhesion.

As additional layers are exposed in LDP, the amount of polymerization that occurs on the window exponentially increases. As demonstrated by the experimental results, this is the onset of failure and after some number of exposures the chamber window or the part will tear. Figure 5.6 shows PEGDA will begin polymerize on the chamber window as the oxygen inhibition layer disappears. Polymerization to the chamber window begins to occur on the

window around the 8th layer and by the 15th layer there is complete polymer conversion to the chamber window. This restricts the number of layers that can be written using the LDP process to approximately 10 to 15 layers under the exposure and material conditions simulated, after which significant polymerization on the chamber window is likely and new liquid layers cannot be injected into the exposure region. This restriction on the number of layers limits the structured volumes LDP can fabricate, significantly reducing its usefulness.

However, as demonstrated by the fabrication of the waveguide array in Chapter 2, over 100 layers can be sequentially written with the LDP process. This suggests the current simulation is missing an aspect of the LDP process that enables sequential layering. A process step of LDP that is not represented in the current simulation is the injection of fresh monomer next to the chamber window and wait time following the injection. The intended function of this process step is to create a large supply of unreacted monomer adjacent to the exposed regions of the photopolymer. In addition to creating a large supply of unreacted monomer, this process step could also replenish the oxygen concentration in the PDMS by diffusion of oxygen from the fresh monomer. The fresh monomer contains its atmospheric equilibrium concentration of oxygen, so there is a sufficient oxygen concentration gradient to drive diffusion. To test the hypothesis, the injection of fresh monomer and wait time between exposures was added to the model.

To model the injection of fresh monomer and wait time after each exposure, the polymerized regions where monomer conversion was higher than the gel point, were assumed to be replenished with fresh monomer that had initial concentrations of all species including oxygen. The concentration of oxygen was left unchanged where the monomer conversion was less than the gel point. This assumes the platform motion is instantaneous and new fresh monomer was injected directly adjacent to the inhibited region with no mixing. Oxygen was then allowed to diffuse for the specified wait time. After the wait time the platform was returned to the proper depth and the next layer was modeled with the concentration of oxygen in the PDMS after the wait time.
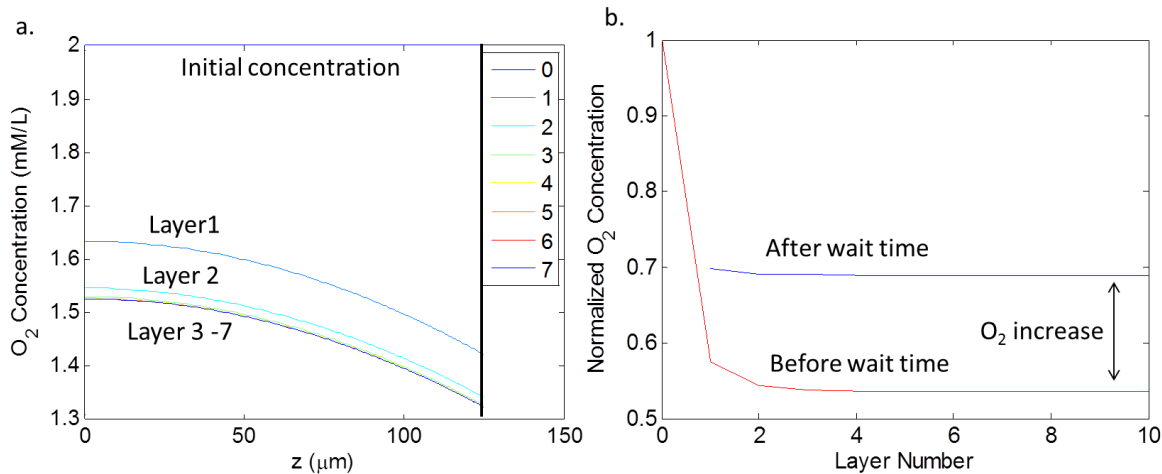
Figure 5.7: Oxygen concentration in the PDMS of the chamber windows as a function of depth and layer number with 180 seconds of wait time between exposures. (a) The oxygen concentration in the PDMS as a function of position for the first 7 layers. (b) Plot of the oxygen concentration in the PDMS before and after the wait time as a function of layer number.

Figure 5.7 shows that the oxygen concentration in the PDMS reaches steady-state in three layers if a wait time of 180 seconds is included between exposed layers. After the third layer is written, the amount of oxygen that diffuses from the PEGDA monomer into the PDMS layer during the wait time equals the amount of oxygen consumed during the exposure of a single layer. Therefore, the system has reached a steady-state operating point, where the oxygen concentration in the PDMS is the same at the beginning of the exposure for every layer.

A steady-state concentration of oxygen in PDMS results in a stable oxygen inhibition layer thickness and the layer thickness is constant. Figure 5.8 shows the oxygen inhibition layer quickly reaches steady state when a wait time of 180 seconds is included between exposed layers. The oxygen inhibition layer thickness decreases 150 nm from the first to the second layer, however this is a small reduction compared to fabrications that did not include a wait time. After the second layer is fabricated the thickness of the oxygen inhibition layer does not change, enabling a high degree of control of the exposed layer thickness. To
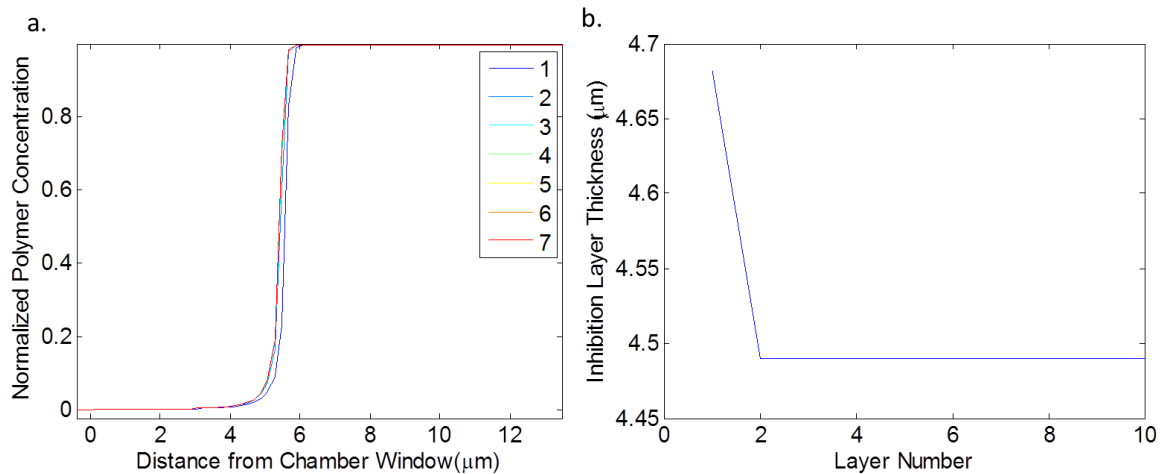
Figure 5.8: Oxygen inhibition layer thickness as a function of layer number with a 180 second wait time between exposures. (a) The normalized conversion of polymer as a function of distance away from chamber window interface for the first 7 layers written. (b) Oxygen inhibition layer thickness as a function of layer number for the first 10 layers written. The thickness of the oxygen inhibition layer is defined as the distance from the PDMS/PEGDA interface to the first instance where the normalized polymer concentration is 0.02.

compensate for the change in the oxygen inhibition layer thickness between the first and second written layer the thicknesses of layer can be adjusted or an unstructured base layer can be written.

The wait time between exposures also allows for repetitive layering because polymerization at the chamber window does not occur. The degree of polymerization on the chamber window as a function of layer number is shown in Figure 5.9.

Figure 5.9 demonstrates the amount of polymerization on the chamber window for wait times of 180 seconds is negligible. The maximum amount of polymerization on the chamber window is approximately 0.06 %, approximately two orders of magnitude less than the gel point of PEGDA, so the material will not polymerize at the window. Most likely, a small amount of short chain oligimers will be created near the window which diffuse away from the window during the wait time.

The simulation results demonstrate LDP's ability to fabricate many layers is dependent
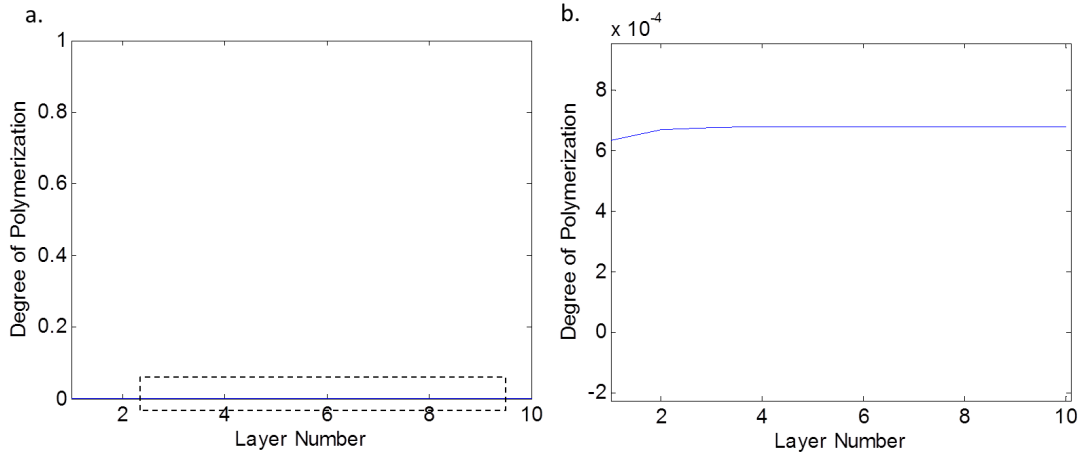
Figure 5.9: (a) Degree of polymerization on the chamber window as a function of layers written with a 180 second wait time in between exposures. (b), Magnified image of (a) demonstrating lack of polymerization on the chamber window.

on the wait time between exposures. The wait time allows oxygen from PEGDA to replenish the oxygen concentration in the PDMS and reach steady state oxygen concentration for many layers. If the wait time is not sufficient to reach steady state oxygen concentration, the oxygen inhibition layer will decrease with the layer number and polymerization to the chamber window will eventually occur.

5.4   Experimental validation of the model

To confirm the results of the model, a test system that used uniform exposures and incorporated a pressure transducer to measure the force required to detach the fabricated polymer volume from the chamber window was created. The process steps for the test setup, referred to as the pull tester, are shown in Figure 5.10.

5.4.1   Pressure transducer

The pressure transducer used in all experiments was an Omega LCL Series thin-beam load cell. Omega LCL series thin-beam load cells are specifically designed for frequent small-
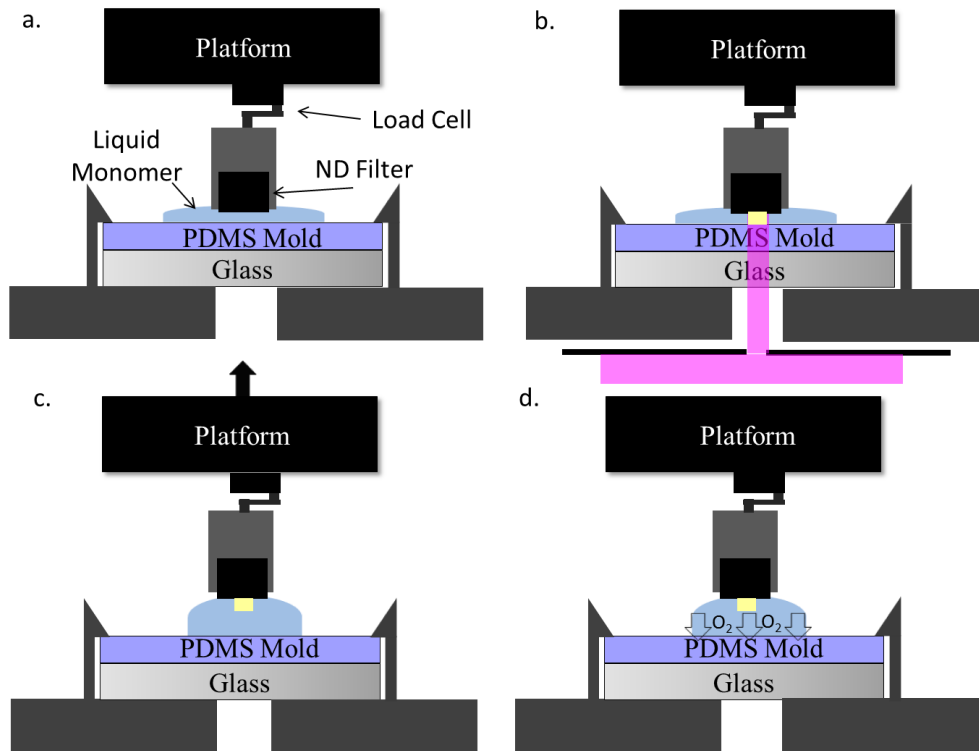
Figure 5.10: Experimental procedure for the pull tester. (a) An ND filter and pressure sensing load cell attached to a moving platform is lowered to 10 μm from the chamber window, producing a 10 μm thick liquid layer of PEGDA. (b) The PEGDA liquid layer is polymerized by uniform light, using 365 nm light, creating a solid cross-linked polymer attached to the platform. (c) The platform is then raised at 250μm/s, while the pressure sensor measures the amount of force required to pull the polymerized feature away from the chamber window. (d) Oxygen is then allowed to diffuse from the adjacent layer of liquid monomer into the chamber window to replace the oxygen consumed by polymerization. The platform is lowered to 10 μm from the chamber window again and Steps (b)-(d) are repeated to determine the force required to detach the fabricated polymer volume from the chamber window for each layer.

load measurements, making them ideal for this application. The integrated strain gage of the load cell includes all balancing, compensating, and conductive elements and is laminated to the beam to provide stability and reliability. The load cell is made of a thin metal beam with four thin foil strain gauges bonded to it, arranged into a Wheatstone bridge circuit configuration. Each strain gage bonded to the beam is an active element in the Wheatstone bridge, making the output from the bridge a linear function of force. The LCL-454g has an

accuracy of ± 20 percent, so it must be calibrated with known weights to obtain accurate results.

5.4.2   Electrical signal conditioning

In order to accurately measure the force, the output of the load cell must be conditioned to a level compatible with the A/D converter used to collect the data. To ensure the signal from the load cell compatible with the A/D converter, the conditioning circuit must buffer and amplify the output signal of the load cell. The specified voltage range of the load cell is ±2 mV per volt of excitation voltage given to the load cell. Using the recommended excitation voltage of 5 V results in a voltage range of -/+ 10 mV. A voltage gain of 500 brings the voltage range of the signal to -/+ 5 V, using the full dynamic range of the A/D converter.

The amplification and buffering tasks are both easily accomplished with an instrumentation amplifier. In addition to amplifying and buffering the output signal, the conditioning circuit must also include an low pass filter to reduce noise and improve signal fidelity. Therefore, the output of the instrumentation amplifier is filtered by a passive, single pole low pass filter with a cutoff frequency half that of the sampling frequency. The conditioning circuit is shown in Figure 5.11.

5.4.3   Electrical output of single pull

The force required to detach the polymerized material from the chamber window for each layer must be determined from the voltage measured during the pull tester procedure. During the pull tester procedure, the voltage increases linearly as the platform pulls further away from the chamber window until the pressure sensor imparts enough force to detach the polymer which returns the voltage to zero. After detachment, the platform either returns to the chamber window for the next exposure or remains away from the chamber window to allow oxygen diffusion into the PDMS. An example of the voltage measured from the
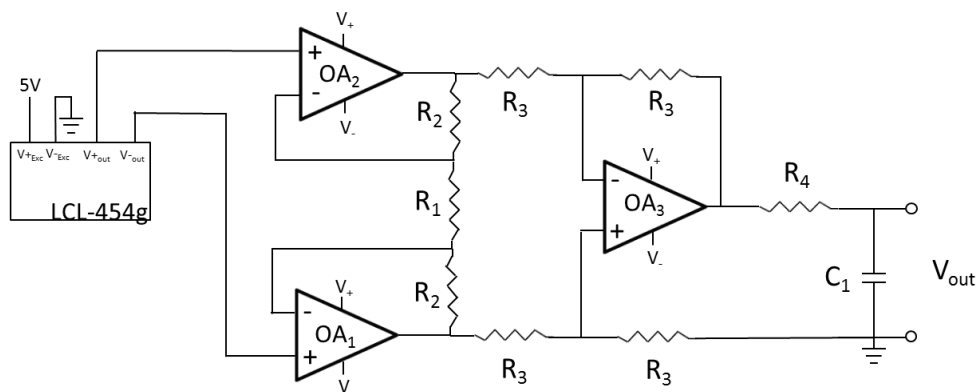
Figure 5.11: The conditioning circuit that amplifies, filters and buffers the output signal of the pressure sensor. R_1 is 470Ω, R_2 is 100kΩ, R_3 is 120kΩ, R_4 is 330kΩ and C_1 is 10nF.

pressure sensor during the pull tester procedure is shown in Figure 5.12.
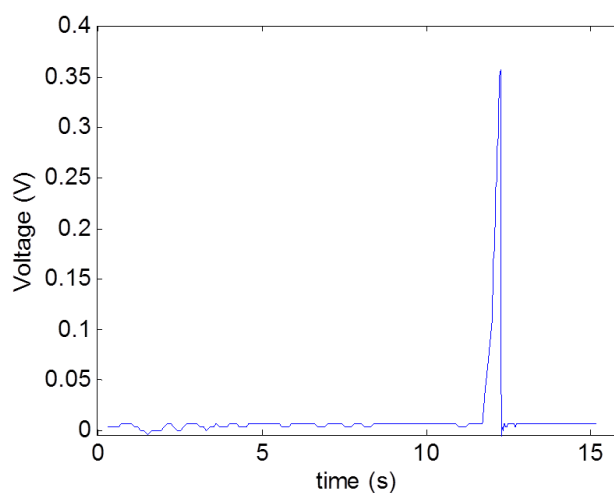
Figure 5.12: Plot of the measured voltage from the pressure sensor as a function of time. The first 10 seconds of the plot are during the exposure. At approximately 12 seconds the platform is raised away from the chamber window at a constant velocity of 250 μm/s. The voltage spike and return occurs when the polymer has detached from the PDMS.

The maximum voltage for a given pull is recorded and converted to a force using the calibration curve found in the next section. If there is no polymer adhesion to the window, no force is required to detach the polymer from the chamber window and the measured

voltage will remain at zero for the duration of the pull tester procedure.

5.4.4 System calibration

The measured output of the Omega LCL-454g pressure transducer is a voltage that must be converted to a mechanical force. In order to convert the measured voltage to force, a hand-held mechanical force gage was used to apply a known force to the pressure transducer while the voltage was recorded. The voltage for applied forces of 100, 200, 300, and 400 grams was recorded for 10 independent measurements and then averaged. The result of the calibration is shown in Figure 5.13. As expected, the output voltage is a linear function of the force applied to the pressure transducer.
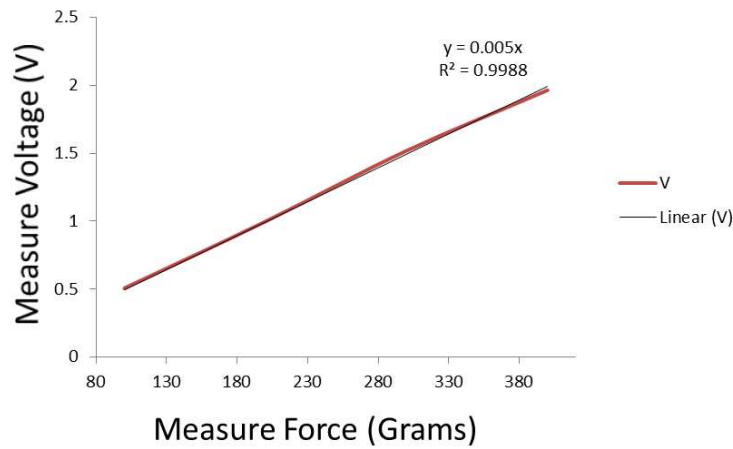
Figure 5.13: Calibration curve converting measured voltage from the LCL-454g pressure sensor to force.

5.4.5 Experimental results

The simulation predictions are experimentally verified in this section with the pull tester. Using the pull tester, 90 layers were sequentially written with no wait time between the fabrication of layers. The force required to detach the polymerized volume from the chamber window was recorded for each layer. To obtain the most accurate comparison

with the simulation results, the experimental parameters were the same as the simulation parameters. Figure 5.14 shows the measured detachment force as a function of layer number and compares it to the degree of polymerization predicted by the simulation.
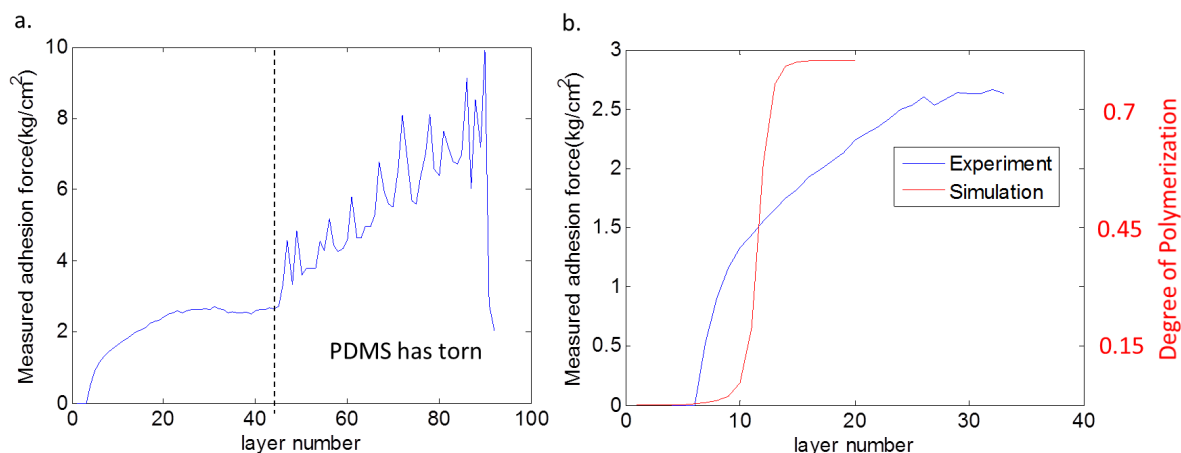
Figure 5.14: Experimental results obtained from the pull tester for sequentially written layers. a, The measured detachment force as a function of layer number with no wait time between exposures. b, Comparison of the measured detachment force and the predicted degree of polymerization on the window by the model

Figure 5.14 shows that the model accurately predicts when polymer will begin to adhere to the PDMS. However the rate at which the modeled degree of polymerization increases is much faster than the rate the measured detachment force increases. Potential explanations for the discrepancy are the model was simple and may have missed some important reaction or diffusion term and/or the precise manner by which polymer growth near the PDMS results in adhesion is unclear. However, the model does predict both the onset of adhesion and the approximate point at which it reaches half of the maximum force before tearing, which is sufficient to optimize the operation of the system since we desire to avoid both conditions.

Constant polymer detachment from the PDMS surface results in pieces of the PDMS being torn from the surface. At layer number 44 the chamber window behavior changes and the measured detachment force begins to increase as a function of layer number. Visual inspection of the chamber window after the exposure revealed a divot in the PDMS in the

exposed area, suggesting that constant polymer detachment tore pieces of the PDMS from the surface. To confirm this induced the change in chamber behavior at layer number 44, the experiment was repeated with only 30 layers and then visually inspected. Visual inspection of the chamber window showed no surface damage to the PDMS.

To demonstrate that a wait time between exposures will suppress polymer adhesion to the PDMS window, the pull tester procedure was repeated with the inclusion of the wait time. The measured detachment force as a function of layer number for a wait time of 180 seconds is shown in Figure 5.15.
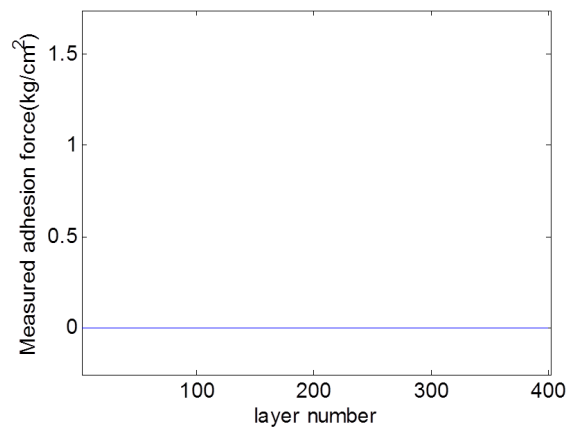
Figure 5.15: The measured detachment force as a function of layer number with 180 seconds of wait time between exposures.

Figure 5.15 shows that for wait times lasting 180 seconds the polymer volume never adheres to the chamber window, confirming the prediction by the model. This demonstrates steady state operation can be achieved when sufficient time is provided for oxygen from the material to diffuse into the PDMS. To understand the chamber window's behavior for wait times ranging from 0 second to 180 seconds not be sufficient to allow the oxygen concentration in PDMS to reach steady state, the required detachment force as a function of layer number was measured for wait times. The results are shown in Figure 5.16.

The results shown in Figure 5.16 demonstrate that as the wait time increases the
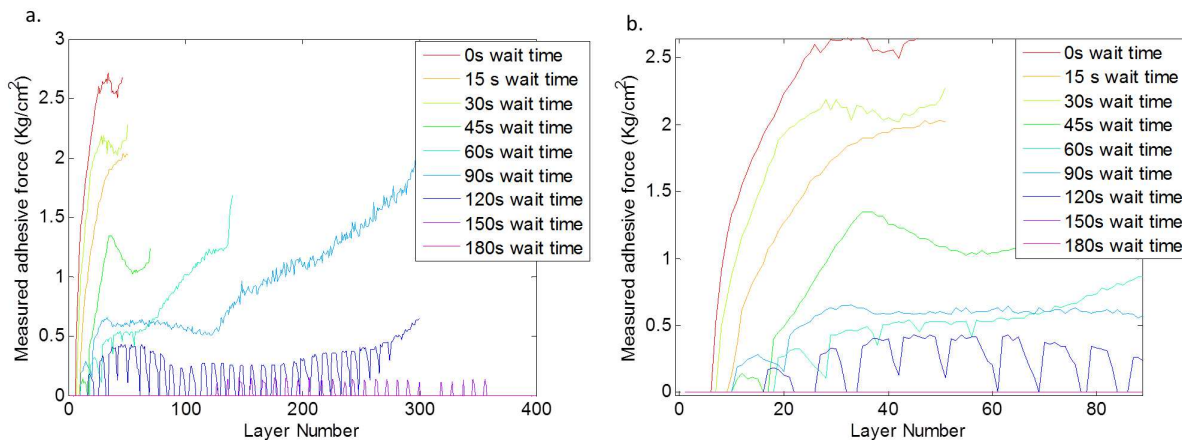
Figure 5.16: Experimental results obtained from the pull tester for sequentially written layers. (a) The required detachment force as a function of layer number for wait times ranging from 0 to 180 seconds. (b) Magnified image of the plot in (a) showing the window behavior at layer numbers 1 - 80.

number of layers that can be written before polymer adhesion is observed also increases. Additionally, the rate at which the required detachment force increases is smaller for longer wait times compared to the rate for short wait times.

The predicted behavior of the chamber window deviates from the experimental results for wait times ranging from 15 to 120 seconds. The model does not predict the polymer concentration at the PDMS interface to ever reach the gel point of PEGDA for wait times longer than 20 seconds. However, Figure 5.16 shows there must be some polymerization on the window for wait times between 20 and 120. Potential sources of the discrepancy between experimental data and simulation results are mechanical changes in the PDMS as layers are written and/or the absence of important chemical parameters in the model.

5.5   Summary and conclusions

In this chapter, I modeled and experimentally validated the dynamics of oxygen diffusion. This revealed that the window has a finite lifetime if used in a rapid fabrication due to depletion of the stored oxygen. However, oxygen can be replenished by introducing a delay

during which oxygen diffuses from the fresh monomer back into the chamber window. I presented a reaction/diffusion simulation of the LDP process that included the PDMS in the model. The results of the simulation showed a wait time was required between exposures for the oxygen concentration in PDMS to maintain a steady state. Steady state chamber window operation results in a consistent oxygen inhibition layer thicknesses and no significant polymerization on the chamber window. The model results were confirmed experimentally by the pull tester, a test bed that quantifies the amount of polymer adhesion to the chamber window.

The model and experimental procedure presented in this chapter can provide answers to fundamental question about the LDP process, such as the required wait time between exposures to replenish oxygen in the PDMS. For example, if a potential material's rates and constants are not known, the pull tester can determine a sufficient wait time between exposures to maintain steady state operation. The required wait time could limit throughput for certain fabrications. Throughput for volumes requiring high axial resolution and/or materials with monomer diffusion coefficients larger than 0.1 μm^2/s may decrease because the process of monomer diffusion will complete before a sufficient amount of oxygen from the monomer has diffused into the PDMS. The experimental and numerical methods presented here are tools to optimize the LDP process for different materials and test new window technology.

Chapter 6

Conclusion and Future Directions

6.1 Conclusions

This thesis has presented a new fabrication process, liquid deposition photolithography (LDP), for efficient production of index structures with nearly arbitrary index feature size and shape not limited by out of focus exposure or transverse diffusional distances. The fabricated 3D index structures can achieve an index contrast up to 0.1, allowing greater flexibility in design of 3D refractive index devices. In addition to full 3D control of index, processing time in LDP is reduced compared to multi-layer planar lithography because the material is self-developing, enabling the entire process to be completed on a single instrument. The self-developing process has the unusual property that total fabrication time for a fixed thickness decreases as the number of layers is increased, enabling fabrication 10^5 faster than femtosecond micromachining. The large index contrast and fast fabrication rate of LDP potentially enable the fabrication of large scale, arbitrary 3D refractive index devices, such as, photonic crystal waveguides [122], diffractive elements and photonic devices.

Chapter 2 introduced LDP by describing the fabrication process and presenting a numerical model of the photo-chemical processes during a fabrication. The individual parts of the process were detailed and results of single and multiple superimposed layers written into a volume of photopolymer were presented. To demonstrate LDP's ability to manufacture photonic devices, a waveguide array containing over 3,000 waveguides was fabricated by sequentially layering and exposing 100 independent layers. The index contrast of the waveg-

uide array was shown to be 0.1, allowing greater flexibility in design of 3D refractive index devices. The results shown in this chapter are the subject of a paper that was published in *Nature Light: Science and Application* in 2013 [177].

Chapter 3 presented the function of the diffusive photopolymer used with the LDP process and how it was designed to achieve high index contrast. The index contrast measured in Chapter 2 is shown to be an order of magnitude larger than expected from the estimated index contrast using bulk measurements. Further analysis of the high index contrast structures needs to be performed in order to accurately characterize the mechanism for high index contrast. It was also shown that for large binary structures to have high fidelity, thin layers must be fabricated to reduce the longitudinal diffusion distance of unreacted monomer. This has the additional benefits of increasing longitudinal resolution and decreasing total fabrication time. The amount of crosstalk between layers was quantified, and the likely mechanism for the crosstalk hypothesized and experimentally demonstrated.

Chapter 4 extended the capabilities of the LDP process by implementing a grayscale pattern generator to enable arbitrary GRIN structuring. The process of longitudinal monomer diffusion allows the fabrication of millimeter scale GRIN structures, demonstrated by single and 25 layer fabrications. The fabrication of 125 μm thick parabolic GRIN structures demonstrated the LDP process has a higher throughput and index contrast compared to single layer fabrications due to the short diffusion path created by the process. LDP's ability to create high fidelity, nearly arbitrary GRIN structures was demonstrated by the fabrication of 125 μm thick volumes containing index structures with 10 different Zernike polynomials.

Chapter 5 described a model and a experiment that investigated the dynamics of oxygen diffusion in LDP. The model and experiment revealed that the chamber window has a finite lifetime if used in a rapid fabrication due to depletion of stored oxygen. The results of the simulation showed a wait time was required between exposures for the oxygen concentration in PDMS to maintain a steady state. Steady state chamber window operation

results in a consistent oxygen inhibition layer thicknesses and no significant polymerization on the chamber window. The model results were confirmed experimentally by the pull tester, a test bed that quantifies the amount of polymer adhesion to the chamber window. The experimental and numerical methods presented in this chapter are tools that can be used to optimize the LDP process for a variety of materials and test new window technology.

This thesis has presented a new fabrication process and demonstrated its potential to manufacture optical devices with high complexity and throughput. In addition to optical device fabrication, the opportunity exists to extend the process to 3D physical structuring for applications such as: MEMS, rapid prototyping and biomedical applications. The following section provides some suggestions for future directions that build on the work presented in this thesis.

6.2 Future Research on LDP

6.2.1 Multiple Material LDP

The work presented in Chapter 2 provided an initial demonstration of the ability of LDP to fabricate complex physical micro-structures for MEMS. Currently, fabrication techniques such as bulk micromachining, surface micromachining, LIGA processing and wafer bonding are the most used methods for fabricating complex micro-structures [178, 179]. However, these processes are not ideal for fabricating sophisticated 3D micro-structures, because they utilize multi-layered planar processing, which is time consuming and unable to fabricate smooth surfaces. To increase throughput and enable smooth surface fabrication, 3D micro-fabrication technologies such as micro-stereolithography [42] and two-photon absorption [44] have been developed. Two-photon absorption has demonstrated 100 nm feature sizes written for micro-structures [45] and MEMS devices [46], however structures are limited in volume due to the method's low throughput.

Micro-stereolithography offers the potential for both high resolution and high through-

put complex micro-structure fabrication. The major limitation to minimum feature size in micro-stereolithography is the polymerization depth of the process and material used [121]. To increase depth resolution, an unreactive, highly absorbing chemical can be added to the resin to significantly reduce the polymerization depth [180]. The minimum layer thickness becomes restricted by adhesion of solidified photopolymer to the glass window in the fixed-surface method or the surface tension of the liquid resin in the free-surface method [181], limiting resolution to 20 μm for most micro-stereolithography processes. Low absorption materials and an irradiation dose close to the polymerization threshold has been used to achieve 400 nm transverse and 1.5 μm depth resolution [181]. However, the polymerization rate needs to be small to prevent out-of-focus polymerization, so the scanning speed of the laser beam is limited to 10 μm/s, slower than two-photon absorption.

I propose using an additional material ("sacrificial") in LDP that would prevent out-of-focus polymerization in the primary material ("structural") by occupying the un-polymerized regions of the structural material, enabling both high throughput and resolution. To spatially control the solidification of the two materials, separate vats and control valves would be used to select the material to be structured. To inject the desired material into the exposure chamber, the appropriate control valve would be opened and the platform would be lowered to inject either the sacrificial or structural material. To ensure only the material to be solidified occupies the unpolymerized regions in the layer to be written, a large volume of material will need to be injected into the exposure chamber with sufficient time to allow extraneous material to diffuse away from the layer. After the diffusion process has completed, the platform can then be moved to its initial position and the unexposed regions of the layer will contain only a single material. This process would be completed for both materials, solidifying the entire layer, providing a mechanical scaffold for subsequent layers. The process steps of multiple material LDP are shown in Figure 6.1.
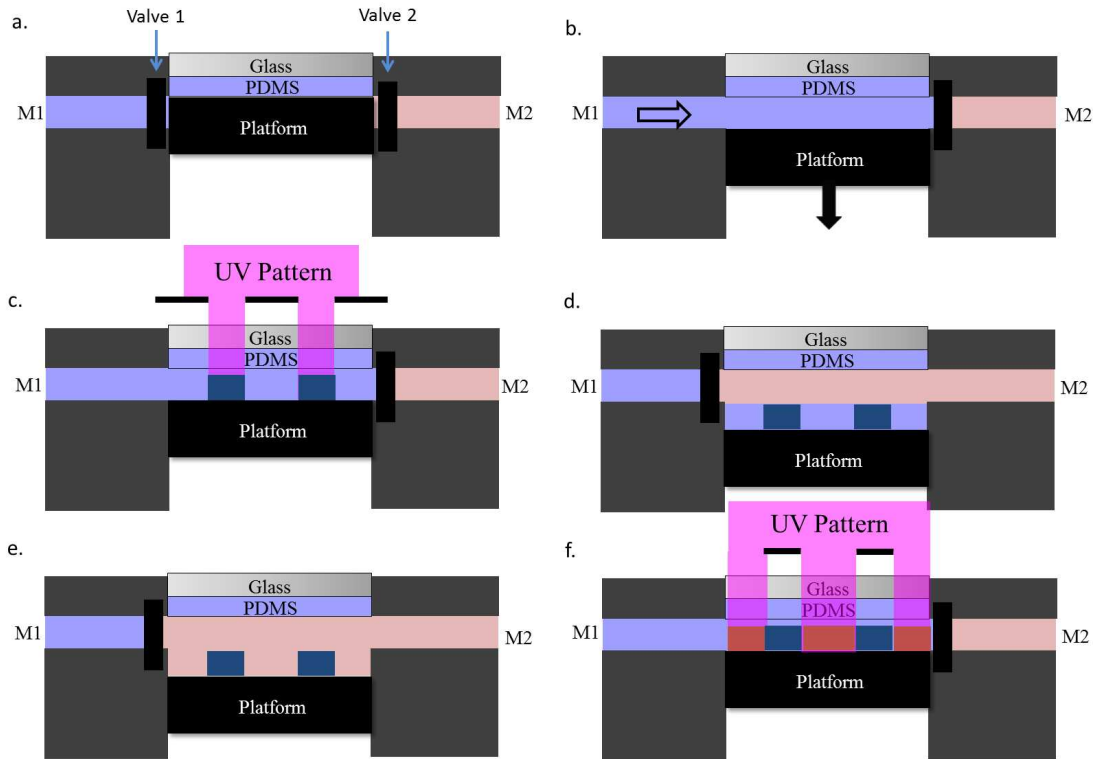
Figure 6.1: Process steps of multiple material LDP, where M1 is the resin polymerized for structural material and M2 is the resin polymerized for sacrificial material. (a) The chamber setup for multiple material LDP. In addition to using two materials to valves are also used (b) Valve 1 is opened and M1 is drawn through a microfluidic channel created as the platform is lowered, producing a new layer. (c) The new liquid layer is patterned by 2D projection lithography, using 365 nm light, polymerizing the liquid monomer into the 2D pattern. (d) Valve 1 is closed and valve 2 is opened and M2 is drawn through a microfluidic channel created as the platform is lowered much farther than the platform was lowered in step (b) to inject a large volume of M2. (e) The thin liquid M1 layer diffuses into thick liquid layer of M2. (f) Raise platform back to thickness set in step (b) and pattern M2 with inverse of pattern exposed to M1. This process is repeated until the entire volume is fabricated. A solvent wash to remove M2

In order to obtain the desired part dimensions after fabrication, the sacrificial material must be removed without removing or damaging the structural material. In order to preferentially remove the sacrificial material, the materials must have an significant difference in solubility in the solvent used. To obtain the difference in solubility, the structural material will most likely need to be a high functionality, highly cross-linked polymer that has a glass transition temperature higher than room temperature. Conversely, the sacrificial monomer will most likely be a mono-functional polymer that has a much lower glass transition temperature compared to the structural polymer.

6.2.2   Determining mechanism of high index contrast

The chemical mechanism that drives the large index contrast demonstrated with LDP is not well understood and further explanation requires additional experiments beyond what is encompassed within this thesis. The index contrast measured in Chapter 2 is shown to be an order of magnitude larger than expected compared to the bulk material measurements used to estimate the index contrast, shown in Chapter 3. Further analysis of the high index contrast structures need to be performed in order to accurately characterize the mechanism for high index contrast and explain the discrepancy between measurements. A potential tool for further exploration is confocal Raman spectroscopy [131, 182].

Confocal Raman microscopy yields two and three dimensional images of the chemical composition of complex, multi-component materials. Confocal Raman microscopy combines the three-dimensional spatial resolution of confocal microscopy and the vibrational sensitivity of Raman spectroscopy. Therefore, it is able to analyze the spatial composition of samples consisting of different materials in a nondestructive experiment. The achievable resolution is of the order of the light wavelength in all three dimensions. The only prerequisites are that their Raman spectra contain at least one specific line for each component and that the luminescence background be sufficiently low.

To reveal the physical mechanism that drives high index change, I propose measuring

the chemical composition on the surface of a LDP fabricated waveguide array with a confocal Raman microscope. The confocal Raman microscope has sufficient resolution to probe the structures and has been previously used to determine the spatial dependence of chemical concentrations of holographic gratings in multi-component diffusive photopolymers [183, 184]. Once the chemical concentrations were known, the Lorenz-Lorentz relation[185] could be applied to confirm the theoretical refractive index matched the measured value. Provided a confocal Raman microscope is available this is a relatively straightforward experiment that should help explain the chemical mechanism the creates the high index contrast.

Bibliography

[1] Pham, D. and Gault, R. A comparison of rapid prototyping technologies. <u>Mach Tool Manufacturing</u> **38** (1998).

[2] Wendel, B., Rietzel, D., Kuhnlein, F., Feulner, R., Hulder, G., and Schmachtenberg, E. Additive processing of polymers. <u>Macromolecular Material Engineering</u> **10** (2008).

[3] llc., C. http://cubify.com/cube/, (2013).

[4] systems, D. http://www.3ders.org/, (2013).

[5] D'Urso, P. S., Effeney, D. J., Earwaker, W. J., Barker, T. M., Redmond, M. J., Thompson, R. G., and Tomlinson, F. H. Custom cranioplasty using stereolithography and acrylic. <u>British Journal of Plastic Surgery</u> **53**(3), 200 – 204 (2000).

[6] Sarment, D. P., Sukovic, P., and Clinthorne, N. Accuracy of implant placement with a stereolithographic surgical guide. <u>The International journal of oral & maxillofacial implants</u> **18**(4) (2003).

[7] Cooke, M., Fisher, J., Dean, D., Rimnac, C., and Mikos, A. Use of stereolithography to manufacture critical-sized 3d biodegradable scaffolds for bone ingrowth. <u>Journal of Biomedical Materials Research Part B: Applied Biomaterials</u> **64**(2) (2002).

[8] Langer, R. and Vacanti, J. Tissue engineering. <u>Science</u> **260** (1993).

[9] Lu, Y., Mapili, G., Suhali, G., Chen, S. C., and Roy, K. A digital micro-mirror device-based system for the micro fabrication of complex, spatially patterned tissue engineering scaffolds. <u>Journal of Biomedical Materials Research Part A</u> **77** (2006).

[10] Arcaute, K., Mann, B., and Wicker, R. Stereolithography of three-dimensional bioactive poly(ethylene glycol) constructs with encapsulated cells. <u>Annals of Biomedical Engineering</u> **34**, 1429–1441 (2006). 10.1007/s10439-006-9156-y.

[11] Nguyen, K. T. and West, J. L. Photopolymerizable hydrogels for tissue engineering applications. <u>Biomaterials</u> **23**(22), 4307 – 4314 (2002).

[12] Hornbeck, L. 128 by 128 deformable mirror device. <u>Electron Devices, IEEE Transactions on</u> **30**(5), 539 – 545 (1983).

[13] Rebeiz, G. M. RF MEMS: Theory, Design, and Technology. Wiley, 1st edition, (2003).

[14] Sharpe, W.N., J., Jackson, K., Hemker, K., and Xie, Z. Effect of specimen size on young's modulus and fracture strength of polysilicon. Microelectromechanical Systems, Journal of **10**(3), 317 – 326 (2001).

[15] Beebe, D., Moore, J., Bauer, J., Yu, Q., Liu, R., Devadoss, C., Jo, B., et al. Functional hydrogel structures for autonomous flow control inside microfluidic channels. Nature **404**(6778), 588–590 (2000).

[16] Mohanty, A., Misra, M., and Hinrichsen, G. Biofibres, biodegradable polymers and biocomposites: An overview. Macromolecular Materials and Engineering **276**(1), 1–24 (2000).

[17] Peppas, N., Hilt, J., Khademhosseini, A., and Langer, R. Hydrogels in biology and medicine: from molecular principles to bionanotechnology. Advanced Materials **18**(11), 1345–1360 (2006).

[18] Roemer, M., Kurzenknabe, T., Oesterschulze, E., and Nicoloso, N. Microactuators based on conducting polymers. Analytical and bioanalytical chemistry **373**(8), 754–757 (2002).

[19] Liu, C. Recent advances in polymer mems. Advanced Materials **21** (2007).

[20] Leonhardt, U. Optical conformal mapping. Science **312**(5781), 1777–1780 (2006).

[21] Pendry, J., Schurig, D., and Smith, D. Controlling electromagnetic fields. Science **312**(5781), 1780–1782 (2006).

[22] Dolin, L. S. On a possibility of comparing three-dimensional electromagnetic. Izv. Vuz. Radiofiz. **4**, 964967 (1961).

[23] Pendry, J., Holden, A., Stewart, W., and Youngs, I. Extremely low frequency plasmons in metallic mesostructures. Physical review letters **76**(25), 4773–4776 (1996).

[24] Pendry, J., Holden, A., Robbins, D., and Stewart, W. Magnetism from conductors and enhanced nonlinear phenomena. Microwave Theory and Techniques, IEEE Transactions on **47**(11), 2075–2084 (1999).

[25] Shelby, R., Smith, D., and Schultz, S. Experimental verification of a negative index of refraction. Science **292**(5514), 77–79 (2001).

[26] Smith, D., Pendry, J., and Wiltshire, M. Metamaterials and negative refractive index. Science **305**(5685), 788–792 (2004).

[27] Lezec, H., Dionne, J., and Atwater, H. Negative refraction at visible frequencies. Science **316**(5823), 430–432 (2007).

[28] Shalaev, V. Optical negative-index metamaterials. Nature photonics **1**(1), 41–48 (2007).

[29] Yao, J., Liu, Z., Liu, Y., Wang, Y., Sun, C., Bartal, G., Stacy, A., and Zhang, X. Optical negative refraction in bulk metamaterials of nanowires. Science **321**(5891), 930 (2008).

[30] Valentine, J., Li, J., Zentgraf, T., Bartal, G., and Zhang, X. An optical cloak made of dielectrics. Nature Materials **8**(7), 568–571 (2009).

[31] Ginn, J., Brener, I., Peters, D., Wendt, J., Stevens, J., Hines, P., Basilio, L., Warne, L., Ihlefeld, J., Clem, P., et al. Realizing optical magnetism from dielectric metamaterials. Physical Review Letters **108**(9), 97402 (2012).

[32] Dhar, L., Curtis, K., and Fäcke, T. Holographic data storage: Coming of age. Nature photonics **2**(7), 403–405 (2008).

[33] Leith, E., Kozma, A., Upatnieks, J., Marks, J., and Massey, N. Holographic data storage in three-dimensional media. Applied Optics **5**(8), 1303–1311 (1966).

[34] Glezer, E., Milosavljevic, M., Huang, L., Finlay, R., Her, T.-H., Callan, J. P., and Mazur, E. Three-dimensional optical storage inside transparent materials. Optics Letters **21**(24), 2023–2025 (1996).

[35] Kruth, J. Material incress manufacturing by rapid prototyping techniques. CIRP Annals-Manufacturing Technology **40**(2), 603–614 (1991).

[36] Hull, C. W. Apparatus for production of three-dimensional objects by stereolithograph, (1986). US Patent 4,575,330.

[37] Bertsch, A., Bernhard, P., Vogt, C., and Renaud, P. Rapid prototyping of small size objects. Rapid Prototyping Journal **6**(4), 259–266 (2000).

[38] Jacobs, P. F. Rapid prototyping & manufacturing: fundamentals of stereolithography. Sme, (1992).

[39] Zhang, X., Jiang, X., and Sun, C. Micro-stereolithography of polymeric and ceramic microstructures. Sensors and Actuators A: Physical **77**(2), 149–156 (1999).

[40] Varadan, V., Jiang, X., and Varadan, V. Microstereolithography and other fabrication techniques for 3D MEMS. Wiley, (2001).

[41] Ikuta, K. and Hirowatari, K. Real three dimensional micro fabrication using stereo lithography and metal molding. In Micro Electro Mechanical Systems, 1993, MEMS'93, Proceedings An Investigation of Micro Structures, Sensors, Actuators, Machines and Systems. IEEE, 42–47. IEEE, (1993).

[42] Sun, C., Fang, N., Wu, D., and Zhang, X. Projection micro-stereolithography using digital micro-mirror dynamic mask. Sensors and Actuators A: Physical **121**(1), 113–120 (2005).

[43] Chatwin, C., Farsari, M., Huang, S., Heywood, M., Birch, P., Young, R., and Richardson, J. Uv microstereolithography system that uses spatial light modulator technology. Applied Optics **37**(32), 7514–7522 (1998).

[44] Kawata, S., Sun, H., Tanaka, T., and Takada, K. Finer features for functional microdevices. Nature **412**(6848), 697–698 (2001).

[45] Maruo, S., Nakamura, O., and Kawata, S. Three-dimensional microfabrication with two-photon-absorbed photopolymerization. Optics Letters **22**(2), 132–134 (1997).

[46] Lee, K., Kim, R., Yang, D., and Park, S. Advances in 3d nano/microfabrication using two-photon initiated polymerization. Progess in Polymer Science **33**(6), 631–681 (2008).

[47] Griffith, M. L. and Halloran, J. W. Freeform fabrication of ceramics via stereolithography. Journal of the American Ceramic Society **79**(10), 2601–2608 (1996).

[48] Lee, J. W., Lee, I. H., and Cho, D.-W. Development of micro-stereolithography technology using metal powder. Microelectronic engineering **83**(4), 1253–1256 (2006).

[49] Marcus, H. and Bourell, D. Solid freeform fabrication finds new applications. Advanced materials & processes **144**(3), 28–35 (1993).

[50] Agarwala, M., Bourell, D., Beaman, J., Marcus, H., and Barlow, J. Direct selective laser sintering of metals. Rapid Prototyping Journal **1**(1), 26–36 (1995).

[51] Sachs, E., Cima, M., Cornie, J., Brancazio, D., Bredt, J., Curodeau, A., Fan, T., Khanuja, S., Lauder, A., Lee, J., et al. Three-dimensional printing: the physics and implications of additive manufacturing. CIRP Annals-Manufacturing Technology **42**(1), 257–260 (1993).

[52] Michaels, S., Sachs, E., and Cima, M. Metal parts generation by three dimensional printing. In Proceedings of the Fourth International Conference on Rapid Prototyping, 26–42, (1993).

[53] Feygin, M. Laminated object manufacturing. In National Conference on Rapid Prototyping, 63–65, (1990).

[54] Feygin, M., Hsieh, B., and Melkanoff, M. Laminated object manufacturing (lom): a new tool in the cim world. In Proceedings of the IFIP TC5/WG5. 3 Eight International PROLAMAT Conference on Human Aspects in Computer Integrated Manufacturing, 457–464, (1992).

[55] Three dimensional micro integrated fluid systems (MIFS) fabricated by stereo lithography, (1994).

[56] Carrozza, M., Croce, N., Magnani, B., and Dario, P. A piezoelectric-driven stereolithography-fabricated micropump. Journal of Micromechanics and Microengineering **5**(2), 177 (1999).

[57] Ballandras, S., Calin, M., Zissi, S., Bertsch, A., André, J., and Hauden, D. Microstereophotolithography and shape memory alloy for the fabrication of miniaturized actuator. Sensors and Actuators A: Physical **62**(1), 741–747 (1997).

[58] Ji, T., Vinoy, K., and Varadan, V. Distributed mems phase shifters by microstereolithography on silicon substrates for microwave and millimeter wave applications. Smart materials and structures **10**(6), 1224 (2001).

[59] Lorenz, H., Despont, M., Fahrni, N., Brugger, J., Vettiger, P., and Renaud, P. High-aspect-ratio, ultrathick, negative-tone near-uv photoresist and its applications for mems. Sensors and Actuators A: Physical **64**(1), 33–39 (1998).

[60] Becker, E., Ehrfeld, W., Hagmann, P., Maner, A., and Mfinchmeyer, D. Fabrication of microstructures with high aspect ratios and great structural heights by synchrotron radiation lithography, galvanoforming, and plastic moulding (liga process). Microelectronic Engineering **4**, 35 – 56 (1986).

[61] Willke, T. and Gearhart, S. Liga micromachined planar transmission lines and filters. Microwave Theory and Techniques, IEEE Transactions on **45**(10), 1681–1688 (1997).

[62] Park, K., Lee, J., Kim, J., Lee, B., Kim, N., Park, J., Kim, G., Bu, J., and Chung, K. A new three-dimensional 30 ghz bandpass filter using the liga micromachined process. Microwave and Optical Technology Letters **30**(3), 199–201 (2001).

[63] IEEE. High vertical aspect ratio LIGA microwave 3-dB coupler, (2003).

[64] Guckel, H., Skrobis, K., Christenson, T., Klein, J., Han, S., Choi, B., Lovell, E., and Chapman, T. Fabrication and testing of the planar magnetic micromotor. Journal of Micromechanics and Microengineering **3**(1) (1999).

[65] Nakamura, S., Suzuki, K., Ataka, M., Fujita, H., Basrour, S., Soumann, V., Labachelerie, M., and Daniau, W. An electrostatic microactuator using liga process for a magnetic head tracking system of hard disk drives. Microsystem technologies **5**(2), 69–71 (1998).

[66] Deng, K., Dewa, A., Ritter, D., Bonham, C., and Guckel, H. Characterization of gear pumps fabricated by liga. Microsystem technologies **4**(4), 163–167 (1998).

[67] Verpoorte, E., Van Der Schoot, B., Jeanneret, S., Manz, A., Widmer, H., and De Rooij, N. Three-dimensional micro flow manifolds for miniaturized chemical analysis systems. Journal of Micromechanics and Microengineering **4**(4) (1999).

[68] Gattass, R. R. and Mazur, E. Femtosecond laser micromachining in transparent materials. Nature photonics **2**, 219–225 (2008).

[69] Davis, K., Miura, K., Sugimoto, N., and Hirao, K. Writing waveguides in glass with a femtosecond laser. Optics Letters **21**(21), 1729–1731 (1996).

[70] Sikorski, Y., Said, A., Bado, P., Maynard, R., Florea, C., and Winick, K. Optical waveguide amplifier in nd-doped glass written with near-ir femtosecond laser pulses. Electronics letters **36**(3), 226–227 (2000).

[71] Streltsov, A. and Borrelli, N. Fabrication and analysis of a directional coupler written in glass by nanojoule femtosecond laser pulses. Optics Letters **26**(1), 42–43 (2001).

[72] Kowalevicz, A., Sharma, V., Ippen, E., Fujimoto, J., and Minoshima, K. Three-dimensional photonic devices fabricated in glass by use of a femtosecond laser oscillator. Optics Letters **30**(9), 1060–1062 (2005).

[73] Gerke, T. and Piestun, R. Aperiodoic volume optics. Nature photonics **4**(3), 188–193 (2010).

[74] Cumpston, B., Ananthavel, S., Barlow, S., Dyer, D., Ehrlich, J., Erskine, L., Heikal, A., Kuebler, S., Lee, I., McCord-Maughon, D., et al. Two-photon polymerization initiators for three-dimensional optical data storage and microfabrication. Nature **398**(6722), 51–54 (1998).

[75] Zoubir, A., Lopez, C., Richardson, M., and Richardson, K. Femtosecond laser fabrication of tubular waveguides in poly (methyl methacrylate). Optics Letters **29**(16), 1840–1842 (2004).

[76] Sowa, S., Watanabe, W., Tamaki, T., Nishii, J., and Itoh, K. Symmetric waveguides in poly (methyl methacrylate) fabricated by femtosecond laser pulses. Optics Express **14**(1), 291–297 (2006).

[77] Ergin, T., Stenger, N., Brenner, P., Pendry, J., and Wegener, M. Three-dimensional invisibility cloak at optical wavelengths. Science **328**(5976), 337–339 (2010).

[78] Gansel, J., Thiel, M., Rill, M., Decker, M., Bade, K., Saile, V., von Freymann, G., Linden, S., and Wegener, M. Gold helix photonic metamaterial as broadband circular polarizer. Science **325**(5947), 1513–1515 (2009).

[79] Zhao, G. and Mouroulis, P. Diffusion model of hologram formation in dry photopolymer materials. Journal of Modern Optics **41**(10), 1929–1939 (1994).

[80] Dhar, L., Hale, A., Katz, H., Schilling, M., Schnoes, M., and Schilling, F. Recording media that exhibit high dynamic range for digital holographic data storage. Optics Letters **24**(7), 487–489 (1999).

[81] Anderson, K. and Curtis, K. Polytopic multiplexing. Optics Letters **29**(12), 1402–1404 (2004).

[82] McLeod, R., Daiber, A., McDonald, M., Robertson, T., Slagle, T., Sochava, S., and Hesselink, L. Microholographic multilayer optical disk data storage. Applied Optics **44**(16), 3197–3207 (2005).

[83] McLeod, R. Impact of phase aberrations caused by multilayer optical data storage in weakly inhomogeneous media. JOSA B. **26**(2), 308–317 (2009).

[84] Sullivan, A., Grabowski, M., and McLeod, R. Three-dimensional direct-write lithography into photopolymer. Applied Optics **46**(3), 295–301 (2007).

[85] Sato, A., Scepanovic, M., and Kostuk, R. Holographic edge-illuminated polymer bragg gratings for dense wavelength division optical filters at 1550 nm. Applied optics **42**(5), 778–784 (2003).

[86] Ye, C. and McLeod, R. Grin lens and lens array fabrication with diffusion-driven photopolymer. Optics Letters **33**(22), 2575–2577 (2008).

[87] Newport. GTS-30V Newport stage, (2013).

[88] Self, S. A. Focusing of spherical gaussian beams. Appl. Opt. **22**(5), 658–661, Mar (1983).

[89] Dendurkuri, D., Pregibon, D., Collins, J., Hatton, T., and Doyle, P. Continuous flow lithography for high-throughput microparticle synthesis. Nature Materials **5** (2006).

[90] Dendurkuri, D., Pregibon, D., Collins, J., Hatton, T., and Doyle, P. Stop flow lithography in a microfluidic device. Lab on a chip **7** (2008).

[91] Decker, C. and Jenkins, A. Kinetic approach of o2 inhibition in ultraviolet- and laser-induced polymerizations. Macromolecules **18**, 12411244 (1985).

[92] Tsougeni, K., Tserepi, A., and Gogolides, E. Photosensitive poly(dimethylsiloxane) materials for microfluidic applications. Microelectronic Engineering **84** (2007).

[93] Heidelberg. DWL 66fs. http://www.himt.de/factsheets/dwl66fs.pdf, (2013).

[94] Newport. XM series linear stages, (2013).

[95] Ye, C. Three-dimensional Gradient Index Optics Fabricated in Diffusive Photopolymers. PhD thesis, University of Colorado Boulder, (2012).

[96] Wikipedia.edu. Sla example, (2012).

[97] BNS. High speed addressing, (2013).

[98] Bertsch, A., Zissi, S., Jezequel, J., Corbel, S., and Andre, J. Microstereophotolithography using a liquid crystal display as dynamic mask-generator. Microsystem Technologies **3**(2), 42–47 (1997).

[99] Imahori, H., Miyoshi, T., Takaya, Y., and Hayashi, T. Micro-stereolithography of dot shapes for lightguide using lcd grayscale mask.

[100] Jain, K., Dunn, T. J., and Hoffman, J. M. Seamless, maskless lithography system using spatial light modulator, , nov (2001). US Patent 6,312,134.

[101] Yet, S., Ko, B., Lee, S., and May, M. Investigation of ufo defect on duv car and barc process. In Proceedings of SPIE, volume 5375, 940–948, (2004).

[102] Dendurkuri, D., Panda, P., Haghgooie, R., Kim, J., Hatton, T., and Doyle, P. Modeling of oxygen-inhibited free radical photopolymerization in a pdms microfluidic device. Macromolecules **48**, 8547–8556 (2008).

[103] O'Brien, A. and Bowman, C. Modeling the effect of oxygen on photopolymerization kinetics. Macromolecular Theory and Simulations **18** (2006).

[104] Bowen, J., Acrivos, A., and Oppenheim, A. Singular perturbation refinement to quasi-steady state approximation in chemical kinetics. Chemical Engineering Science **18**(3), 177–188 (1963).

[105] Lin, H. and Freeman, B. D. Gas permeation and diffusion in cross-linked poly (ethylene glycol diacrylate). Macromolecules **39**(10), 3568–3580 (2006).

[106] Kızılel, S., Pérez-Luna, V. H., and Teymour, F. Mathematical model for surface-initiated photopolymerization of poly (ethylene glycol) diacrylate. Macromolecular theory and simulations **15**(9), 686–700 (2006).

[107] Berchtold, K. A., Lovestead, T. M., and Bowman, C. N. Coupling chain length dependent and reaction diffusion controlled termination in the free radical polymerization of multivinyl (meth) acrylates. Macromolecules **35**(21), 7968–7975 (2002).

[108] Goodner, M. D. and Bowman, C. N. Development of a comprehensive free radical photopolymerization model incorporating heat and mass transfer effects in thick films. Chemical Engineering Science **57**(5), 887–900 (2002).

[109] Goodner, M. D. and Bowman, C. N. Modeling and experimental investigation of light intensity and initiator effects on solvent-free photopolymerizations. In ACS SYMPOSIUM SERIES, volume 713, 220–231, (1998).

[110] Sullivan, A. C. and McLeod, R. R. Tomographic reconstruction of weak, replicated index structures embedded in a volume. Optics Express **21**(15), 14202–14212 (2007).

[111] Ikeda, M., Tateda, M., and Yoshikiyo, H. Refractive index profile of a graded index fiber: measurement by a reflection method. Applied Optics **14**(4), 814–815 (1975).

[112] Cogswell, C. and Sheppard, C. Confocal differential interference contrast (dic) microscopy: including a theoretical analysis of conventional and confocal dic imaging. Journal of Micrscopy **165**, 81–101 (1992).

[113] King, S. V., Libertun, A., Piestun, R., Cogswell, C. J., and Preza, C. Quantitative phase microscopy through differential interference imaging. Journal of biomedical optics **13**(2), 24020 (2008).

[114] Youk, Y. and Kim, D. Y. A simple reflection-type two-dimensional refractive index profile measurement technique for optical waveguides. Optics communications **262**(2), 206–210 (2006).

[115] T., W., JN, G., and CJR, S. Optical fibre profiling using a scanning optical microscope. Optical and Quantum Electronics **12**, 341–345 (1980).

[116] Tateda, M. Single-mode-fiber refractive-index profile measurement by reflection method. Applied Optics **17**(3), 475–478 (1978).

[117] Snyder, A. W. and Love, J. Optical waveguide theory, volume 190. Springer, (1983).

[118] Fallahkhair, A. B., Li, K. S., and Murphy, T. Vector finite difference modesolver for anisotropic dielectric waveguides. Journal of Lightwave Technology **26**(11), 1423–1431 (2008).

[119] Gallagher, D. F. and Felici, T. P. Eigenmode expansion methods for simulation of optical propagation in photonics: pros and cons. In Integrated Optoelectronics Devices, 69–82, (2003).

[120] Ye, C., Kamysiak, K., Sullivan, A., and McLeod, R. Mode profile imaging and loss measurement for uniform and tapered single-mode 3d waveguides in diffusive photopolymer. Optics Express **20**(6), 6575–6583 (2012).

[121] Nakamoto, T., Yamaguchi, K., Abraha, P., and Mishima, K. Manufacturing of three-dimensional micro-parts by uv laser induced polymerization. Journal of micromechanics and microengineering **6**(2), 240 (1999).

[122] Argyros, A., Birks, T., Leon-Saval, S., Cordeiro, C., Luan, F., and Russell, P. Photonic bandgap with an index step of one percent. Optics Express **13**(1), 309–314 (2005).

[123] Hesselink, L., Orlov, S., and Bashaw, M. Holographic data storage systems. Proceedings of the IEEE **92**(8), 1231–1280 (2004).

[124] Psaltis, D. and Burr, G. Holographic data storage. Computer **31**(2), 52–60 (1998).

[125] Colvin, V., Larson, R., Harris, A., and Schilling, M. Quantitative model of volume hologram formation in photopolymers. Journal of applied physics **81**(9), 5913–5923 (1997).

[126] Sheridan, J. and Lawrence, J. Nonlocal-response diffusion model of holographic recording in photopolyme. JOSA A **17**(6), 1108–1114 (2000).

[127] Curtis, K., Dhar, L., Hill, A., Wilson, W., and Ayres, M. Holographic Data Storage. Wiley, (2010).

[128] Hardaker, S., Moghazy, S., Cha, C., and Samuels, R. Quantitative characterization of optical anisotropy in high refractive index films. Journal of Polymer Science Part B: Polymer Physics **31**(13), 1951–1963 (1993).

[129] Peiris, F., Lee, S., Bindley, U., and Furdyna, J. A prism coupler technique for characterizing thin film ii–vi semiconductor systems. Journal of applied physics **84**(9), 5194–5197 (1998).

[130] Gleeson, M. R. and Sheridan, J. T. A review of the modelling of free-radical photopolymerization in the formation of holographic gratings. Journal of optics A: pure and applied optics **11**(2), 024008 (2009).

[131] Dieing, T., Hollricher, O., and Toporski, J. Confocal raman microscopy, volume 158. Springer, (2011).

[132] Yu, W. and Yuan, X. Uv induced controllable volume growth in hybrid sol-gel glass for fabrication of a refractive microlens by use of a grayscale mask. Opt. Express **11**(18), 2253–2258, Sep (2003).

[133] Jiang, H., Yuan, X., Yun, Z., Chan, Y.-C., and Lam, Y.-L. Fabrication of microlens in photosensitive hybrid sol–gel films using a gray scale mask. Materials Science and Engineering: C **16**(1), 99–102 (2001).

[134] Däschner, W., Long, P., Stein, R., Wu, C., and Lee, S. Cost-effective mass fabrication of multilevel diffractive optical elements by use of a single optical exposure with a gray-scale mask on high-energy beam-sensitive glass. Applied Optics **36**(20), 4675–4680 (1997).

[135] Wang, M. R. and Su, H. Laser direct-write gray-level mask and one-step etching for diffractive microlens fabrication. Applied Optics **37**(32), 7568–7576 (1998).

[136] Waits, C. M., Modafe, A., and Ghodssi, R. Investigation of gray-scale technology for large area 3d silicon mems structures. Journal of Micromechanics and Microengineering **13**(2), 170 (2002).

[137] Morgan, B., Waits, C. M., Krizmanic, J., and Ghodssi, R. Development of a deep silicon phase fresnel lens using gray-scale lithography and deep reactive ion etching. Microelectromechanical Systems, Journal of **13**(1), 113–120 (2004).

[138] Oppliger, Y., Sixt, P., Stauffer, J., Mayor, J., Regnault, P., and Voirin, G. One-step 3d shaping using a gray-tone mask for optical and microelectronic applications. Microelectronic Engineering **23**(1), 449–454 (1994).

[139] Hornbeck, L. J. Deformable-mirror spatial light modulators. In 33rd Annual Techincal Symposium, (1990).

[140] TI. dlp5500, (2013).

[141] Platt, B. C. History and principles of shack-hartmann wavefront sensing. Journal of Refractive Surgery **17**(5), 573–577 (2001).

[142] Atkinson, L. G., Houde-Walter, S. N., Moore, D. T., Ryan, D. P., and Stagaman, J. M. Design of a gradient-index photographic objective. Applied Optics **21**(6), 993–998 (1982).

[143] Moore, D. T. Design of single element gradient-index collimator. JOSA **67**(9), 1137–1143 (1977).

[144] Moore, D. T. Design of singlets with continuously varying indices of refraction. JOSA **61**(7), 886–894 (1971).

[145] Mallinson, S. R. and Warnes, G. Optimization of thick lenses for single-mode optical-fiber microcomponents. Optics Letters **10**(5), 238–240 (1985).

[146] Tomlinson, W. Applications of grin-rod lenses in optical fiber communication systems. Applied Optics **19**(7), 1127–1138 (1980).

[147] Tearney, G., Boppart, S., Bouma, B., Brezinski, M., Weissman, N., Southern, J., and Fujimoto, J. Scanning single-mode fiber optic catheter-endoscope for optical coherence tomography. Optics Letters **21**(7), 543–545 (1996).

[148] Tearney, G. J., Brezinski, M. E., Bouma, B. E., Boppart, S. A., Pitris, C., Southern, J. F., and Fujimoto, J. G. In vivo endoscopic optical biopsy with optical coherence tomography. Science **276**(5321), 2037–2039 (1997).

[149] Koike, Y., Sumi, Y., and Ohtsuka, Y. Spherical gradient-index sphere len. Applied optics **25**(19), 3356–3363 (1986).

[150] Jin, Y., Tai, H., Hiltner, A., Baer, E., and Shirk, J. S. New class of bioinspired lenses with a gradient refractive index. Journal of applied polymer science **103**(3), 1834–1841 (2007).

[151] Marchand, E. W. Gradient index optics. New York: Academic Press, 1978 **1** (1978).

[152] Sinai, P. Correction of optical aberrations by neutron irradiation. Applied Optics **10**(1), 99–104 (1971).

[153] Pickering, M. A., Taylor, R. L., and Moore, D. T. Gradient infrared optical material prepared by a chemical vapor deposition process. Applied optics **25**(19), 3364–3372 (1986).

[154] Ohmi, S., Sakai, H., Asahara, Y., Nakayama, S., Yoneda, Y., and Izumitani, T. Gradient-index rod lens made by a double ion-exchange process. Applied Optics **27**(3), 496–499 (1988).

[155] Kindred, D. S., Bentley, J., and Moore, D. T. Axial and radial gradient-index titania flint glasses. Applied optics **29**(28), 4036–4041 (1990).

[156] Liu, J.-H., Chen, J.-L., Wang, H.-Y., and Tsai, F.-R. Fabrication of a gradient refractive index (grin) plastic rod using the novel process of centrifugal diffusing polymerization. Macromolecular Chemistry and Physics **201**(1), 126–131 (2000).

[157] Liu, J.-H. and Chiu, Y.-H. Process equipped with a sloped uv lamp for the fabrication of gradient-refractive-index lenses. Optics letters **34**(9), 1393–1395 (2009).

[158] Wu, S. P., Nihei, E., and Koike, Y. Large radial graded-index polymer. Applied optics **35**(1), 28–32 (1996).

[159] Gonsalves, R. A. Phase retrieval and diversity in adaptive optics. Optical Engineering **21**(5), 215829–215829 (1982).

[160] Tyson, R. Principles of adaptive optics. CRC Press, (2010).

[161] Grimm, B., Goelz, S., Bille, J. F., et al. Objective measurement of wave aberrations of the human eye with the use of a hartmann-shack wave-front sensor. JOSA A **11**(7), 1949–1957 (1994).

[162] Weibel, D. B. and Whitesides, G. M. Applications of microfluidics in chemical biology. Current Opinion in Chemical Biology **10**(6), 584–591 (2006).

[163] Yi, C., Li, C.-W., Ji, S., and Yang, M. Microfluidics technology for manipulation and analysis of biological cells. Analytica Chimica Acta **560**(1), 1–23 (2006).

[164] Houston, K., Weinkauf, D., and Stewart, F. Gas transport characteristics of plasma treated poly (dimethylsiloxane) and polyphosphazene membrane materials. Journal of membrane science **205**(1), 103–112 (2002).

[165] Koros, W. and Fleming, G. Membrane-based gas separation. Journal of Membrane Science **83**(1), 1–80 (1993).

[166] Dendukuri, D., Hatton, T. A., and Doyle, P. S. Synthesis and self-assembly of amphiphilic polymeric microparticles. Langmuir **23**(8), 4669–4674 (2007).

[167] Barker, A. L., Macpherson, J. V., Slevin, C. J., and Unwin, P. R. Scanning electrochemical microscopy (secm) as a probe of transfer processes in two-phase systems: Theory and experimental applications of secm-induced transfer with arbitrary partition coefficients, diffusion coefficients, and interfacial kinetics. The Journal of Physical Chemistry B **102**(9), 1586–1598 (1998).

[168] Merkel, T., Bondar, V., Nagai, K., Freeman, B., and Pinnau, I. Gas sorption, diffusion, and permeation in poly (dimethylsiloxane. Journal of Polymer Science Part B: Polymer Physics **38**(3), 415–434 (2000).

[169] De Bo, I., Van Langenhove, H., Pruuost, P., De Neve, J., Pieters, J., Vankelecom, I. F., and Dick, E. Investigation of the permeability and selectivity of gases and volatile organic compounds for polydimethylsiloxane membranes. Journal of membrane science **215**(1), 303–319 (2003).

[170] Unwin, P. R. and Bard, A. J. Scanning electrochemical microscopy. scanning electrochemical microscope induced desorption: a new technique for the measurement of adsorption/desorption kinetics and surface diffusion rates at the solid/liquid interface. The Journal of Physical Chemistry **96**(12), 5035–5045 (1992).

[171] Kamiya, Y., Naito, Y., Hirose, T., and Mizoguchi, K. Sorption and partial molar volume of gases in poly (dimethyl siloxane). Journal of Polymer Science Part B: Polymer Physics **28**(8), 1297–1308 (1990).

[172] Anseth, K. S., Wang, C. M., and Bowman, C. N. Kinetic evidence of reaction diffusion during the polymerization of multi(meth)acrylate monomers. Macromolecules **27**(3), 650–655 (1994).

[173] Allen, P. E. M., Simon, G. P., Williams, D. R. G., and Williams, E. H. Dynamic mechanical properties and cross-polarized, proton-enhanced, magic angle spinning carbon-13 nmr time constants of poly[oligo(ethylene glycol)dimethacrylates]. Macromolecules **22**(2), 809–816 (1989).

[174] Simon, G. P., Allen, P. E. M., Bennett, D. J., Williams, D. R. G., and Williams, E. H. Nature of residual unsaturation during cure of dimethacrylates examined by cppemas carbon-13 nmr and simulation using a kinetic gelation model. Macromolecules **22**(9), 3555–3561 (1989).

[175] Zhu, S., Tian, Y., Hamielec, A. E., and Eaton, D. R. Radical trapping and termination in free-radical polymerization of methyl methacrylate. Macromolecules **23**(4), 1144–1150 (1990).

[176] Studer, K., Decker, C., Beck, E., and Schwalm, R. Overcoming oxygen inhibition in uv-curing of acrylate coatings by carbon dioxide inerting: Part ii. Progress in organic coatings **48**(1), 101–111 (2003).

[177] Urness, A. C., Moore, E. D., Kamysiak, K. K., Cole, M. C., and McLeod, R. R. Liquid deposition photolithography for submicrometer resolution three-dimensional index structuring with large throughput. Nature Light: Science & Applications **2**(3), e56 (2013).

[178] Wise, K. D. and Najafi, K. Microfabrication techniques for integrated sensors and microsystems. Science **254**(5036), 1335–1342 (1991).

[179] Bustillo, J. M., Howe, R. T., and Muller, R. S. Surface micromachining for microelectromechanical systems. Proceedings of the IEEE **86**(8), 1552–1574 (1998).

[180] Zissi, S., Bertsch, A., Jézéquel, J.-Y., Corbel, S., Lougnot, D., and Andre, J. Stereolithography and microtechniques. Microsystem technologies **2**(1), 97–102 (1995).

[181] Maruo, S. and Ikuta, K. Submicron stereolithography for the production of freely movable mechanisms by using single-photon polymerization. Sensors and Actuators A: Physical **100**(1), 70–76 (2002).

[182] Kador, L., Schittkowski, T., Bauer, M., and Fan, Y. Three-dimensional materials analysis by confocal raman microspectroscopy. Applied optics **40**(28), 4965–4970 (2001).

[183] Kagan, C., Harris, T., Harris, A., and Schilling, M. Submicron confocal raman imaging of holograms in multicomponent photopolymers. Unknown Journal **108**(16), 6892–6896 (1998).

[184] Lagugné Labarthet, F., Buffeteau, T., and Sourisseau, C. Molecular orientations in azopolymer holographic diffraction gratings as studied by raman confocal microspectroscopy. The Journal of Physical Chemistry B **102**(30), 5754–5765 (1998).

[185] Aubrecht, I., Miler, M., and Koudela, I. Recording of holographic diffraction gratings in photopolymers: theoretical modelling and real-time monitoring of grating growth. Journal of Modern Optics **45**(7), 1465–1477 (1998).

[186] Ergin, T., Stenger, N., Brenner, P., Pendry, J. B., and Wegener, M. Supporting online material for three-dimensional invisibility cloak at optical wavelengths. Science **328**(5976) (2010).

Appendix A

Calculations

A.1   Throughput of Waveguide Array Fabrication using LDP

Writing times for one structure using a single pattern with a 4 mm diameter and 1 mm depth is approximately 15 hours..

$$\text{Fabrication rate}(\mu m^3/s) = ((\pi(2,000^2)(1,000)))/(54,000) = 233,000(\mu m^3/s) \quad \text{(A.1)}$$

$$\text{Fabrication time}(mm^3) = (10^9 \mu m^3)/(233,000(\mu m^3/s)) = 4,300s = 1.2(\text{hours}/mm^3) \quad \text{(A.2)}$$

A.2   Two-Photon Write Time Calculation

The writing time quoted in the supplementary material for the fabrication of a single woodpile invisibility cloak measuring 90 μm in length, 30 μm in width, and 10 μm in height with a 0.8 μm woodpile rod spacing is three hours [186]. The calculation of fabrication rate and fabrication time for one mm^3 is thus

$$\text{Fabrication rate}(\mu m^3/s) = ((90)(30)(10))/(10,800) = 2.5(\mu m^3/s) \quad \text{(A.3)}$$

$$\text{Fabrication time}(mm^3) = (10^9 \mu m^3)/2.5(\mu m^3/s) = 4x10^8 s = 12.68(\text{years}/mm^3) \quad \text{(A.4)}$$

Appendix B

Exposure Conditions

The intensity and doses for all the exposures are similar, but the individual experiments have differences in both illumination intensity and dose. These differences are due to long term fluctuations in the laser source, small inconsistencies in material batches and different optimal exposure for different structures.

For Figure 2.17 the exposure conditions are:

- Irradiance of the binary mask pattern is 25 mW/cm^2

- Exposure dose of the binary mask pattern is 400 mJ/cm^2.

- Irradiance of the post-cure is 15 mW/cm^2,

- Exposure dose of the post-cure is 250 mJ/cm^2.

For Figure 2.18(a) the exposure conditions are:

- Irradiance of the binary mask pattern is 35 mW/cm^2.

- Exposure dose for the first layer is 400 mJ/cm^2.

- Exposure dose for the second is 720 mJ/cm^2.

- Irradiance of the post cure is 15 mW/cm^2.

- Exposure dose of the post-cure is 275 mJ/cm^2.

The exposure does in this case were optimized for clarity of Differential Interference Contrast (DIC) micrograph images.

For Figure 2.18(b-c) the exposure conditions are:

- Irradiance of the beam illuminating the mask is 25 mW/cm^2.

- Dose for the patterned layer is 375 mJ/cm^2.

- Irradiance of the post-cure is 15 mW/cm^2.

- Dose of the post-cure is 275 mJ/cm^2.

For Figure 2.19 the exposure conditions are:

- Irradiance of the beam illuminating the mask was 25mW/cm^2.

- Exposure dose of the written layers is 375 mJ/cm^2.

- Irradiance of the post-cure is 15 mW/cm^2

- Exposure dose of the post-cure is 275 mJ/cm^2.

For Figures 3.3 the exposure conditions are:

- Irradiance of the beam illuminating the mask is 15 mW/cm^2.

- Exposure dose of the written layer is 450 mJ/cm^2.

- Irradiance of the post-cure is 15 mW/cm^2,

- Exposure dose of the post-cure is 275 mJ/cm^2.

For 3.11 the exposure conditions are:

- Irradiance of the beam illuminating the mask is 15 mW/cm^2.

- Exposure dose for the written layers is 350 mJ/cm^2.

- Irradiance of the post-cure is 15 mW/cm^2

- Exposure dose of the post-cure is 275 mJ/cm^2.

For Figure 3.12, 3.14 and 3.13 the exposure conditions are:

- Irradiance of the beam illuminating the mask is 15 mW/cm^2.

- Exposure dose for the written layers is 375 mJ/cm^2.

- Irradiance of the post-cure is 15 mW/cm^2

- Exposure dose of the post-cure is 275 mJ/cm^2.